


5-2014

## PERFORMANCE EVALUATION OF MATERIAL DECOMPOSITION USING RAPID KVP-SWITCHING DUAL-ENERGY CT FOR ASSESSING BONE MINERAL DENSITY

John M. Wait

Follow this and additional works at: [https://digitalcommons.library.tmc.edu/utgsbs\\_dissertations](https://digitalcommons.library.tmc.edu/utgsbs_dissertations)

 Part of the [Musculoskeletal Diseases Commons](#), [Musculoskeletal, Neural, and Ocular Physiology Commons](#), [Orthopedics Commons](#), [Other Physical Sciences and Mathematics Commons](#), and the [Radiology Commons](#)

### Recommended Citation

Wait, John M., "PERFORMANCE EVALUATION OF MATERIAL DECOMPOSITION USING RAPID KVP-SWITCHING DUAL-ENERGY CT FOR ASSESSING BONE MINERAL DENSITY" (2014). *The University of Texas MD Anderson Cancer Center UTHealth Graduate School of Biomedical Sciences Dissertations and Theses (Open Access)*. 451.

[https://digitalcommons.library.tmc.edu/utgsbs\\_dissertations/451](https://digitalcommons.library.tmc.edu/utgsbs_dissertations/451)

This Thesis (MS) is brought to you for free and open access by the The University of Texas MD Anderson Cancer Center UTHealth Graduate School of Biomedical Sciences at DigitalCommons@TMC. It has been accepted for inclusion in The University of Texas MD Anderson Cancer Center UTHealth Graduate School of Biomedical Sciences Dissertations and Theses (Open Access) by an authorized administrator of DigitalCommons@TMC. For more information, please contact [digitalcommons@library.tmc.edu](mailto:digitalcommons@library.tmc.edu).

PERFORMANCE EVALUATION OF MATERIAL DECOMPOSITION USING RAPID KVP-  
SWITCHING DUAL-ENERGY CT FOR ASSESSING BONE MINERAL DENSITY

By

John Matthew Spiridigliozzi Wait, B.S.

APPROVED:

---

S. Cheenu Kappadath, Ph. D., Supervisory Professor

---

Dianna D. Cody, Ph. D.

---

X. John Rong, Ph. D.

---

A. Kyle Jones, Ph. D.

---

Veerabhadran Baladandayuthapani, Ph. D.

APPROVED:

---

Dean, The University of Texas  
Graduate School of Biomedical Sciences at Houston

PERFORMANCE EVALUATION OF MATERIAL DECOMPOSITION USING RAPID KVP-  
SWITCHING DUAL-ENERGY CT FOR ASSESSING BONE MINERAL DENSITY

A

THESIS

Presented to the Faculty of  
The University of Texas  
Health Science Center at Houston  
and  
The University of Texas  
M.D. Anderson Cancer Center  
Graduate School of Biomedical Sciences  
in Partial Fulfillment  
of the Requirements  
for the Degree of  
MASTER OF SCIENCE

by

John Matthew Spiridigliozzi Wait, B.S.

Houston, Texas

May, 2014

This work is dedicated to my parents, who have always believed in me.

This thesis was written because of their commitment to my future.



## **Acknowledgments**

This work would not have been possible without the guidance and expertise provided by my supervisory professor, Dr. Cheenu Kappadath. Additionally, the time and assistance pledged by Dr. Dianna Cody was instrumental in its completion. I would like to acknowledge them both and my other committee members, Drs. Kyle Jones, John Rong, and Veera Baladandayuthapani for their significant contributions in shaping this thesis as well as their guidance for my future career. I also relied on the support of Dr. Adam Chandler and a grant from General Electric Healthcare for the completion of this project, as well as the knowledge and experience of Jessica Nute.

I would like to thank Dr. Richard Wendt for providing personal guidance during this process. I would also like to thank Frances Quintana and the rest of the administrative staff of GSBS and the medical physics program for their invaluable assistance. Finally, I would like to thank my friends, fellow students, and family members who have provided incredible support for me throughout my journey.

# PERFORMANCE EVALUATION OF MATERIAL DECOMPOSITION USING RAPID KVP-SWITCHING DUAL-ENERGY CT FOR ASSESSING BONE MINERAL DENSITY

John Matthew Spiridigliozzi Wait, B.S.

Supervisory Professor: S. Cheenu Kappadath, Ph.D.

Osteoporosis is diagnosed by assessing the bone mineral density (BMD) of the trabecular bone, and has previously been characterized with dual-energy x-ray absorptiometry (DXA) or single-energy computed tomography (SECT). Dual-energy computed tomography (DECT) is able to create two three-dimensional sets of images representing the densities of two materials in a given basis pair. DECT is theoretically capable of providing a true density measurement of trabecular bone material with the proper selection of material basis pair.

Using the rapid kVp-switching GE HD750 scanner, the concentrations of various solutes were assessed in two-material syringe-phantoms in different experimental conditions with DECT material density images, SECT and DXA. RMS error was used to evaluate the accuracy of the DECT concentration measurements in air and regression was used to compare measurements made in other scanning conditions. The effect of anthropomorphic geometry was explored in concentric phantoms designed to model bone. The sensitivity of DECT, SECT, and DXA to changes in bone composition was compared. The correlation between different basis pair decompositions was evaluated. Finally, the correlation between DECT concentration measurements and DXA areal BMD (aBMD) measurements was assessed and used to develop a methodology to convert DECT concentration measurements to aBMD measurements.

The RMS error of DECT concentration measurements made in air ranged from 9-244%. Measurements of concentration made off-isocenter or with different DECT techniques were

found to have a small (~5%) effect, but scattering conditions resulted in a reduction of 8-27% with similar trends observed in SECT data. In concentric phantoms, higher-attenuating material in the outer chamber increased measured values of the inner material for all measurement methods. DECT measurements had the highest sensitivity (2 mg/mL  $K_2HPO_4$ ). Different DECT basis pairs were nearly perfectly correlated ( $R^2 \approx 1$ ). This was exploited to demonstrate a strong correlation ( $R^2 = 0.988$ ) between measured  $K_2HPO_4$  concentration and DXA aBMD for different two-material phantoms. The relationship of DECT aBMD and DXA aBMD was highly correlated ( $R^2 = 0.983$ ) but the limits of agreement (-0.16 to 0.57 g/cm<sup>2</sup>) were relatively large compared to clinical utility.

This study suggests that corrections to output DECT concentration measurements may be necessary for clinically acceptable aBMD or trabecular BMD values.

## Table of Contents

Dedication .....	iii
Acknowledgments.....	iv
Abstract .....	v
Table of Contents .....	vii
List of Illustrations.....	ix
List of Tables .....	xvii
List of Abbreviations .....	xx
1. Motivation.....	1
2. Introduction .....	3
2.1 Osteoporosis and Bone Mineral Density.....	3
2.2. Measurement of Bone Mineral Density .....	5
2.2.1. Dual Energy X-Ray Absorptiometry.....	5
2.2.2. Single-Energy Computed Tomography.....	7
2.2.3. Dual Energy Computed Tomography.....	11
2.4. Hypothesis and Specific Aims.....	16
3. Specific Aim I: Performance of DECT and Measurement Method Comparison .....	18
3.1. Subaim 1: Accuracy of DECT and Comparison of Measurements.....	18
3.1.1. Material Decomposition Accuracy.....	18
3.1.2. Differing Scan Parameters .....	40
3.2. Subaim 2: Measurements in Bone Geometry Models.....	57
3.2.1. Concentric Phantom Accuracy .....	57
3.2.2. Reversed Concentric Phantoms.....	75
3.3. Subaim 3: Sensitivity of Measurement Methods.....	79
3.4. Subaim 4: Correlation of Base Pairs.....	91
4. Specific Aim II: Relating DECT to DXA.....	94
4.1. Subaim 1: Correlation of DECT and DXA .....	94
4.2. Subaim 2: DECT Integration and DXA Comparison.....	96
5. Conclusion .....	110
6. Future Work.....	111

7. Bibliography .....	113
8. Vita .....	121

## List of Illustrations

- Figure 1: CIRS 62 electron density phantom, pictured with included tissue-equivalent inserts placed in bores. The inner “head” portion can be removed or it can remain in place to simulate a “body” measurement..... 20
- Figure 2: Configuration of materials used for in-air DECT and SECT measurements. Each syringe-phantom was inserted in the central bore of the electron density body phantom with the solution protruding in air. Eight images that span the solution volume were acquired, and a measurement was made on the central image (image 4 or 5) as shown. .... 20
- Figure 3: Illustration of procedure for making material density measurements in GSI Viewer. The image shown is a material density map; a circular ROI is drawn in the cross-section of the syringe-phantom. .... 21
- Figure 4: Positioning of syringe-phantom for DXA measurement. Five 3/8 in. (9.5 mm) PMMA slabs are placed above and three below to simulate patient scattering conditions in a lumbar spine measurement..... 22
- Figure 5: DXA measurement of a two-material syringe-phantom with the vendor-provided software. A "bone map" was manually drawn on the central axis. The BMD was reported in areal density ( $\text{g}/\text{cm}^2$ ). .... 22
- Figure 6: Mean concentration (mg/mL) measured in an ROI placed in the same position over each of the middle six images of the image stack acquired for three Optiray 320, ethanol,  $\text{K}_2\text{HPO}_4$ , and 10 gm%  $\text{K}_2\text{HPO}_4$  solution syringe-phantoms. The CV for Optiray was 0.6%, the CV for ethanol was 6%, the CV for  $\text{K}_2\text{HPO}_4$  was 0.9%, and the CV for 10 gm%  $\text{K}_2\text{HPO}_4$  solution was 1%. .... 26
- Figure 7: The standard deviation of material density image solute concentration measurements of each syringe-phantom as a function of the measured mean solute concentration. .... 27
- Figure 8: The material density image-derived concentration value of each solute is compared to the known concentration. A linear regression was applied for each solute. The line of equivalence is shown for reference. Error bars on the y-axis indicate total variation for each measurement and are too small to be visible on all but ethanol measurements. Error bars on the x-axis for  $\text{K}_2\text{HPO}_4$ , represent uncertainty in known concentration based on the observed volume but are too small to be visible in this plot. .... 29
- Figure 9: Bland-Altman analysis of material density image concentration measurements compared with known concentration. Error bars on the y-axis represent the total variation of the concentration measurements. .... 31
- Figure 10: Correlation of HU measurements on images acquired using SECT at 120 kVp in air with the normalized known concentration. The known concentration was normalized according to the formula  $(\text{value} - \text{minimum concentration})/(\text{maximum concentration} - \text{minimum concentration})$ . Error bars indicate total variation for each measurement but are too small to be

visible for most measurements. The dotted lines represent the 95% confidence limits for each regression fit to the data. .... 34

Figure 11: Correlation of HU measurements on images acquired using SECT at 80 kVp in air with the normalized known concentration. The known concentration was normalized according to the formula  $(\text{value} - \text{minimum concentration}) / (\text{maximum concentration} - \text{minimum concentration})$ . Error bars indicate total variation for each measurement but are too small to be visible for most measurements. The dotted lines represent the 95% confidence limits for each regression fit to the data. .... 35

Figure 12: Correlation of aBMD measured by DXA with the known normalized concentration of each solute. The known concentration was normalized according to the formula  $(\text{value} - \text{minimum concentration}) / (\text{maximum concentration} - \text{minimum concentration})$ . Error bars indicate total variation for each measurement but are too small to be visible for most measurements. The dotted lines represent the 95% confidence limits for each regression fit to the data. .... 37

Figure 13: Mass attenuation coefficient of water, ethanol, and  $K_2HPO_4$  from 10-200 keV, with the ordinate on a base 10 logarithmic scale. Data taken from NIST XCOM database (109). The effective energies of the two beams used in DECT mode (roughly 40 and 50 keV) are indicated. .... 39

Figure 14: On and off-isocenter measurements with DECT. Right: The syringe-phantom protrudes in air from the central bore of the electron density body phantom on and Center: set 10.5 cm above isocenter. Right: 120 kVp image of a  $K_2HPO_4$  syringe-phantom in air 10.5 cm above isocenter. .... 42

Figure 15: Configuration of materials used for DECT and SECT measurements in scattering conditions. The syringe-phantom was inserted in the central bore of the electron density body phantom with the solution enclosed within the body of the phantom. Eight images that spanned the solution volume were acquired, and a measurement was made on the central image (4 or 5) as shown. .... 42

Figure 16: DECT and SECT measurement in homogenous scattering conditions. Left: Water-equivalent inserts or 60 mL syringes filled with distilled water were placed within all but the central bore of the water-equivalent electron density phantom body to perform measurements of each two-material syringe-phantom. Right: 120 kVp image of a  $K_2HPO_4$  syringe-phantom in homogenous scattering conditions. The two water-equivalent inserts can be seen at the approximate one o' clock and seven o' clock positions. .... 43

Figure 17: DECT and SECT measurements in heterogeneous scattering conditions. Left: Electron density body phantom with tissue-equivalent inserts placed within all but the central bore of the water-equivalent phantom body. The two-material solution is placed within the body of the phantom in the central bore to perform measurements of each syringe-phantom. Right: 120 kVp image of a  $K_2HPO_4$  syringe-phantom in heterogeneous scattering conditions. .... 43

Figure 18: DECT and SECT measurements in smaller-sized homogenous scattering conditions. Left: The outer body portion of the electron density phantom was removed and water-equivalent inserts or 60 mL syringes filled with distilled water were placed within all but the central bore of the water-equivalent electron density phantom to perform measurements of each two-material syringe-phantom. Right: 120 kVp image of a  $K_2HPO_4$  syringe-phantom in the

head portion of the electron density phantom. Due to the display field of view used, the image here looks similar to the image for homogenous scattering conditions in the body phantom. ... 44

Figure 19: Comparison of material density image concentration measurements performed using the GSI-5 and GSI-6 protocols. Error bars on the x and y axis indicate total variation for measurements made using GSI-6 and GSI-5 protocols respectively and aren't visible for most points. .... 47

Figure 20: Comparison of material density image concentration measurements performed at isocenter and 10.5 cm above isocenter. Error bars on the x and y axis indicate total variation for measurements made on and displaced from isocenter respectively and aren't visible for most points. All measurements were made using the GSI-6 protocol. .... 48

Figure 21: Comparison of material density image concentration measurements acquired in air and in different scattering conditions. Error bars on the x and y axis indicate total variation for measurements made in air and in scattering conditions respectively. The line of equivalence is shown for reference..... 50

Figure 22: Comparison of SECT HU measurements acquired in air and in different scattering conditions at 120 and 80 kVp. Error bars on the x and y axis indicate total variation for measurements made in air and in scattering conditions respectively. The line of equivalence is shown for reference..... 51

Figure 23: Variation between scans as an average CV of the mean measurement assessed in DECT, SECT, and DXA for Optiray 320,  $K_2HPO_4$ , and 10 gm%  $K_2HPO_4$  solution syringe-phantoms. .... 53

Figure 24: Variation between images as an average CV of the mean measurement assessed in DECT and SECT for Optiray 320, ethanol,  $K_2HPO_4$ , and 10 gm%  $K_2HPO_4$  solution syringe-phantoms. The very large CV for ethanol measured in air at 120 kVp is mostly due to the relatively small mean value in the denominator. .... 53

Figure 25: Variation in known concentration from phantom preparation as an average CV of the mean measurement assessed in DECT, SECT, and DXA for Optiray 320 and  $K_2HPO_4$  syringe-phantoms. .... 54

Figure 26: Variation in measured mean as an average CV of the mean measurement assessed in DECT and SECT for Optiray 320, ethanol,  $K_2HPO_4$ , and 10 gm%  $K_2HPO_4$  solution syringe-phantoms. .... 54

Figure 27: Total variation as an average CV of the mean measurement assessed in DECT, SECT, and DXA for Optiray 320, ethanol,  $K_2HPO_4$ , and 10 gm%  $K_2HPO_4$  solution syringe-phantoms. The very large CV for ethanol is partially due to the relatively small mean value in the denominator. .... 55

Figure 28: Diagram describing the two sets of concentric phantoms constructed for Section 3.2.1. The color blue represents Optiray 320 solution and the color green represents  $K_2HPO_4$  solution. The increasing concentration of the solute is represented by the darkening hue of each color. The simplified diagrams on the far right illustrate for which solution the concentration was increased and for which solution the concentration remained fixed in each set. .... 59



Figure 29: Configuration of materials for concentric phantom DECT and SECT measurements in air (left) and in scattering conditions (right). ..... 59

Figure 30: Example GSI Viewer in-air measurements of the  $K_2HPO_4$  concentration in the inner circular area and the Optiray 320 concentration in the annular area surrounding. The Optiray 320-water basis pair is used in this illustration..... 60

Figure 31: Left: Placement of concentric phantoms for DXA scanning. Right: Rectangular ROIs drawn on DXA image of concentric phantoms for the inner and outer chambers. .... 60

Figure 32: Material density image concentration measurements in air and scattering conditions of concentric phantoms where the inner  $K_2HPO_4$  solution concentration increases and the outer Optiray 320 solution concentration is fixed. Error bars on the x-axis and y-axis indicate the total variation of the uniform solution measurement and the measurement made in the concentric phantom, respectively. Top Left: Measurements of  $K_2HPO_4$  concentration. A slope of 1 is expected for both measurements; in-air measurements yielded a slope of  $1.13 \pm 0.03$  and scatter measurements yielded a slope of  $1.08 \pm 0.08$ . Bottom Left: Measurements of Optiray 320 concentration. A slope of 0 is expected for both measurements; in-air and scatter measurements both yielded a slope of  $-0.01 \pm 0.04$ . Right: Graphic based on Figure 28 illustrating which solution concentration is changing, which solution concentration is fixed, and which is being plotted to the left (arrow). ..... 62

Figure 33: Material density image concentration measurements in air and scattering conditions of concentric phantoms where the inner  $K_2HPO_4$  solution concentration is fixed and the outer Optiray 320 solution concentration increases. Error bars on the x-axis and y-axis indicate the total variation of the uniform solution measurement and the measurement made in the concentric phantom, respectively. Top Left: Measurements of Optiray 320 concentration. A slope of 1 is expected for both measurements; in-air measurements yielded a slope of  $0.88 \pm 0.03$  and scatter measurements yielded a slope of  $1.01 \pm 0.04$ . Bottom Left: Measurements of  $K_2HPO_4$  concentration. A slope of 0 is expected for both measurements; in-air measurements yielded a slope of  $0.3 \pm 0.1$  and scatter measurements yielded a slope of  $1.1 \pm 0.4$ . Right: Graphic based on Figure 28 illustrating which solution concentration is changing, which solution concentration is fixed, and which is being plotted to the left (arrow). ..... 63

Figure 34: SECT HU measurements of concentric phantoms in air and scattering conditions at 120 and 80 kVp where the inner  $K_2HPO_4$  solution increases and the outer Optiray 320 solution concentration is fixed. Error bars on the x-axis and y-axis indicate the total variation of the uniform solution measurement and the measurement made in the concentric phantom, respectively. Top Left: Measurements of  $K_2HPO_4$  HU. A slope of 1 is expected for all measurements; in-air measurements at 120 kVp yielded a slope of  $0.99 \pm 0.02$  and scatter measurements yielded a slope of  $1.01 \pm 0.03$ . In-air measurements at 80 kVp yielded a slope of  $1.02 \pm 0.02$  and scatter measurements yielded a slope of  $1.03 \pm 0.04$ . Bottom Left: Measurements of Optiray HU. A slope of 0 is expected for all measurements; in-air and scatter measurements at 120 kVp both yielded a slope of  $0.0 \pm 0.1$ . In-air measurements at 80 kVp yielded a slope of  $0.0 \pm 0.1$  and scatter measurements yielded a slope of  $0.0 \pm 0.2$ . Right: Graphic based on Figure 28 illustrating which solution concentration is changing, which solution concentration is fixed, and which is being plotted to the left (arrow). ..... 66

Figure 35: SECT HU measurements of concentric phantoms in air and scattering conditions at 120 and 80 kVp where the inner  $K_2HPO_4$  solution is fixed and the outer Optiray 320 solution concentration increases. Error bars on the x-axis and y-axis indicate the total variation of the uniform solution measurement and the measurement made in the concentric phantom, respectively. Top Left: Measurements of Optiray HU. A slope of 1 is expected for all measurements; in-air measurements at 120 kVp yielded a slope of  $0.94 \pm 0.5$  and scatter measurements yielded a slope of  $0.93 \pm 0.5$ . In-air measurements at 80 kVp yielded a slope of  $0.97 \pm 0.07$  and scatter measurements yielded a slope of  $0.97 \pm 0.06$ . Note that for a 30% Optiray 320 concentration, the CT number reached a maximum value at 80 kVp in air. Bottom Left: Measurements of  $K_2HPO_4$  HU. A slope of 0 is expected for all measurements; in-air measurements at 120 kVp yielded a slope of  $0.8 \pm 0.3$  and scatter measurements yielded a slope of  $0.9 \pm 0.3$ . In-air measurements at 80 kVp yielded a slope of  $0.09 \pm 0.06$  and scatter measurements yielded a slope of  $0.12 \pm 0.04$ . Right: Graphic based on Figure 28 illustrating which solution concentration is changing, which solution concentration is fixed, and which is being plotted to the left (arrow)..... 67

Figure 36: DXA aBMD measurements of concentric phantoms where the inner  $K_2HPO_4$  solution increases and the outer Optiray 320 solution concentration is fixed. Error bars on the x-axis and y-axis indicate the total variation of the uniform solution measurement and the measurement made in the concentric phantom, respectively. Top Left: Measurements of  $K_2HPO_4$  aBMD. A slope of 1 and offset of 0 is expected; measurements yielded a slope of  $0.4 \pm 0.1$  and an offset of  $1.3 \pm 0.1$ . Bottom Left: Measurements of Optiray aBMD. A slope of 0 and offset of  $2.58 \pm 0.02$  is expected; measurements yielded a slope of  $-0.1 \pm 0.2$  and an offset of  $2.0 \pm 0.2$ . Right: Graphic based on Figure 28 illustrating which solution concentration is changing, which solution concentration is fixed and which is being plotted to the left (arrow)..... 70

Figure 37: DXA aBMD measurements of concentric phantoms for which the inner  $K_2HPO_4$  concentration is fixed and the outer Optiray 320 solution concentration increases. Error bars on the x-axis and y-axis indicate the total variation of the uniform solution measurement and the measurement made in the concentric phantom, respectively. Top left: Measurements of Optiray aBMD. An offset of 0 and slope of 1 is expected; measurements yielded a slope of  $0.8 \pm 0.1$  and an offset of  $-0.2 \pm 0.5$ . Bottom left: Measurements of  $K_2HPO_4$  aBMD. A slope of 0 and an offset of  $0.592 \pm 0.009$  is expected; measurements yielded a slope of  $0.58 \pm 0.03$  and an offset of  $0.85 \pm 0.01$ . Right: Graphic based on Figure 28 illustrating which solution concentration is changing, which solution concentration is fixed and which is being plotted to the left (arrow)...71

Figure 38: The aBMD varies for the same size and shaped ROI area on a cylinder depending on position transverse to the axis and cylinder diameter. .... 74

Figure 39: Diagram based on Figure 28 describing the set of three “reverse” concentric phantoms constructed for the reversed concentric phantom experiment. The color blue represents Optiray 320 solution, while the color green represents  $K_2HPO_4$  solution. The increasing concentration of the Optiray 320 represented by the darkening hue. The simplified diagram on the far right illustrates for which solution the concentration was increased and for which solution the concentration remained fixed, as in Figure 28. .... 75

Figure 40: Left: Material density image concentration measurements in air (Top) and in scattering conditions (Bottom) of the inner Optiray 320 solution of increasing concentration,

where the outer  $K_2HPO_4$  solution concentration was fixed. Error bars on the x-axis and y-axis indicate the total variation of the uniform solution measurement and the measurement made in the concentric phantom, respectively. The point corresponding to 20% Optiray concentration appears to reflect an improper Optiray solution preparation. Right: Graphic based on Figure 39 illustrating which solution concentration is changing, which solution concentration is fixed and which is being plotted to the left (arrow). ..... 77

Figure 41: Left: SECT HU measurements in air (Top) and in scatter (Bottom) at 120 and 80 kVp of the inner Optiray 320 solution of increasing concentration, where the outer  $K_2HPO_4$  solution concentration was fixed. Error bars on the x-axis and y-axis indicate the total variation of the uniform solution measurement and the measurement made in the concentric phantom, respectively. The points corresponding to 20% Optiray concentration appears to reflect an improper Optiray solution preparation. Right: Graphic based on Figure 39 illustrating which solution concentration is changing, which solution concentration is fixed and which is being plotted to the left (arrow)..... 78

Figure 42: Material density image concentration measured in air and in scattering conditions for a series of  $K_2HPO_4$  syringe-phantoms for which the concentration of the solute decreases logarithmically. The error bars represent  $2\sigma_z$  for that measurement, where  $z$  is the difference between the measurement for that  $K_2HPO_4$  concentration and water. The error bars are too small to be visible for most points in air. The smallest  $K_2HPO_4$  concentration distinguishable from water in air was 0.16% and 2.5% in scatter. .... 82

Figure 43: Extended plot of  $K_2HPO_4$  concentration for the purpose of evaluating DECT sensitivity. Error bars on the y-axis indicate total variation for each measurement. The dotted lines indicate the 95% confidence intervals. The equation of the regression in air with 95% confidence is  $y = 1.08 \pm 0.02x$  (in mg/mL). The equation of the regression in scattering conditions with 95% confidence is  $y = 0.73 \pm 0.01x$  (in mg/mL)..... 83

Figure 44: SECT HU measured in air and in scattering conditions at 120 and 80 kVp for a series of  $K_2HPO_4$  syringe-phantoms for which the concentration of the solute decreases logarithmically. The error bars represent  $2\sigma_z$  for that measurement, where  $z$  is the difference between the measurement for that  $K_2HPO_4$  concentration and water. The error bars are too small to be visible for most points in air. The smallest  $K_2HPO_4$  concentration distinguishable from water in air was 0.16% and 2.5% in scatter for both 120 and 80 kVp..... 84

Figure 45: Extended plot of  $K_2HPO_4$  concentration for the purpose of evaluating SECT sensitivity. Error bars on the y-axis indicate total variation for each measurement; some are too small to be visible. The dotted lines indicate the 95% confidence intervals. The equation for the 120 kVp regression with 95% confidence is  $y = (1.54 \pm 0.04 \text{ HU (mg/mL)}^{-1})x + (19 \pm 11) \text{ HU}$  in air and  $y = (1.12 \pm 0.02 \text{ HU (mg/mL)}^{-1})x$  in scattering conditions. The equation for the 80 kVp regression with 95% confidence is  $y = (2.09 \pm 0.05 \text{ HU (mg/mL)}^{-1})x + (21 \pm 14) \text{ HU}$  in air and  $y = (1.48 \pm 0.03 \text{ HU (mg/mL)}^{-1})x$  in scattering conditions..... 85

Figure 46: DXA aBMD measured for a series of  $K_2HPO_4$  syringe-phantoms for which the concentration of the solute decreases logarithmically. The error bars represent  $2\sigma_z$  for that measurement, where  $z$  is the difference between the measurement for that  $K_2HPO_4$  concentration and water. The smallest  $K_2HPO_4$  concentration distinguishable from water was 0.31%..... 86

Figure 47: Extended plot of  $K_2HPO_4$  concentration for the purpose of evaluating DXA sensitivity. Error bars on the y-axis indicate total variation for each measurement; most are too small to be visible. The dotted lines indicate the 95% confidence intervals. The equation for the regression with 95% confidence is  $y = (2.23 \pm 0.03 \times 10^{-3} \text{g/cm}^2 (\text{mg/ml})^{-1})x - (8 \pm 1 \times 10^{-2}) \text{g/cm}^2$ . ..... 87

Figure 48: The solute concentrations with different material decomposition basis pairs are measured in the syringe-phantom set containing Optiray 320 and water and plotted against the derived Optiray 320 concentration using the Optiray 320-water basis pair..... 92

Figure 49: The solute concentrations with different material decomposition basis pairs are measured in the syringe-phantom set containing  $K_2HPO_4$  and water and plotted against the derived  $K_2HPO_4$  concentration using the  $K_2HPO_4$ -water basis pair. .... 92

Figure 50: The solute concentrations with different material decomposition basis pairs are measured in the syringe-phantom set containing 10 gm%  $K_2HPO_4$  solution and ethanol and plotted against the derived concentration of 10 gm%  $K_2HPO_4$  solution using the 10 gm%  $K_2HPO_4$  solution-ethanol basis pair..... 93

Figure 51: Correlation of  $K_2HPO_4$  concentration measured from material density images using the  $K_2HPO_4$ -water basis pair for three different solutes with aBMD measured with DXA. .... 95

Figure 52: Left: Anthropomorphic QC phantom included with the Hologic Discovery DXA scanner. The cuboid phantom is designed to produce a measured aBMD of about  $1 \text{g/cm}^2$  on the scanner. Center: DECT  $K_2HPO_4$  material density map. Right: SECT 80 kVp HU image. .... 97

Figure 53: Left: The European Spine Phantom. Center: DECT  $K_2HPO_4$  material density map. Right: SECT 80 kVp HU image. .... 97

Figure 54: Top to bottom: Shank, femoral head, vertebral bodies placed parallel to scan axis, vertebral bodies placed perpendicular to scan axis, neck bones. Left to right: photograph, DECT  $K_2HPO_4$  material density map, SECT 80 kVp HU image..... 98

Figure 55: Arrangement of materials for measurement of animal bones with the DXA scanner. .... 99

Figure 56: Linear regression used to convert material density image-derived  $K_2HPO_4$  concentration (left) and 80 kVp HU (right) to HA concentration using HA density provided by QRM. The equation of the line for DECT  $K_2HPO_4$  measurements is  $y = 0.8445x - 3.536$  (in  $(\text{mg/mL})/(\text{mg/mL})$ ). The equation of the line for SECT 80 kVp HU measurements is  $y = 0.5125x$  (in  $(\text{mg/mL})/\text{HU}$ ) - 6.800 (in  $\text{mg/mL}$ )..... 100

Figure 57: Simplified schematic diagram of the DECT or SECT image integration process for the ESP. A) An axial image set is re-binned into coronal images. A threshold is applied and the remaining voxels are set to zero B) The thresholded images are then integrated into a single image. C) A new threshold is applied and D) the resulting area (within an ROI in this case) is recorded along with the integrated density from which to calculate the aBMD (right)..... 101

Figure 58: Correlation of integrated HA aBMD acquired from DECT images and DXA aBMD. The linear regression is plotted with 95% confidence intervals (dotted lines) and the line of

equivalence. The equation of the regression is  $y = (0.95 \pm 0.04)x$  (in  $(\text{g}/\text{cm}^2)/(\text{g}/\text{cm}^2)$ ) +  $(0.28 \pm 0.09)$  (in  $\text{g}/\text{cm}^2$ )..... 103

Figure 59: Enlargement of Figure 58 showing the range of DXA aBMD values expected to be seen in clinical measurements of the lumbar spine, about 0.65-1.5  $\text{g}/\text{cm}^2$ . Dotted lines represent the 95% confidence intervals and the line of equivalence is shown for reference. ... 104

Figure 60: Bland-Altman analysis comparing DECT aBMD and DXA aBMD of a variety of phantoms illustrated in Figure 58. The mean difference was 0.205  $\text{g}/\text{cm}^2$  with a standard error of 0.005  $\text{g}/\text{cm}^2$ . ..... 105

Figure 61: Correlation of integrated 80 kVp HU areal density acquired from SECT images and DXA aBMD. The linear regression is plotted with 95% confidence intervals, represented as dotted lines. The equation of the regression is  $y = (1.25 \pm 0.5)x$  (in  $(\text{g}/\text{cm}^2)/(\text{g}/\text{cm}^2)$ ). The line of equivalence is shown for comparison. .... 106

Figure 62: Enlargement of Figure 61 showing the range of DXA aBMD values expected to be seen in clinical measurements of the lumbar spine, about 0.65-1.5  $\text{g}/\text{cm}^2$ . Dotted lines represent the 95% confidence intervals of the regression. The line of equivalence is shown for comparison. .... 107

Figure 63: Bland-Altman analysis comparing SECT aBMD and DXA aBMD of a variety of phantoms illustrated in Figure 61. The mean difference was -0.276  $\text{g}/\text{cm}^2$  with a standard error of 0.008  $\text{g}/\text{cm}^2$ . ..... 108

## List of Tables

Table 1: Calculated sources of variation of a solute concentration measurement in air by DECT for a 25% concentration. The mean value and CV of the total variation are also shown for reference. The total variation is the sum of the individual variabilities added in quadrature. ....	25
Table 2: Pearson's correlation coefficients (squared) for correlation, y-intercept, and slope of concentration measurements on images acquired using DECT in air with the GSI-6 protocol and the concentration of each solute or ethanol. Regressions with a y-intercept consistent with 0 within the 95% confidence intervals were re-plotted with the y-intercept set to 0.....	28
Table 3: Statistics for material density image accuracy evaluation. The probability that each linear regression of the measured solute concentration vs. the known concentration has a slope of 1 and intercept of 0 is recorded, as well as the RMS error as an absolute and percentage of the average concentration for all syringe-phantoms of each solute. Significance in this experiment was defined as $p < 0.05$ .....	30
Table 4: Bland-Altman analysis of material density image-derived concentration measurements compared to the known concentration. ....	32
Table 5: Calculated sources of variation of a CT number measurement in air at 120 kVp for a 25% concentration. The mean value and CV of the total variation are also shown for reference. The total variation is the sum of the individual variabilities added in quadrature. ....	32
Table 6: Calculated sources of variation of a CT number measurement in air at 80 kVp for a 20% concentration. The mean value and CV of the total variation are also shown for reference. The total variation is the sum of the individual variabilities added in quadrature. Calculation of the phantom preparation and repeat variation for Optiray 25% was not possible because the CT number reached its maximum value so 20% concentrations were evaluated.....	33
Table 7: Pearson's correlation coefficients (squared) for correlation of HU measurements on images acquired using SECT at 120 kVp and the known concentration of each solute.....	34
Table 8: Pearson's correlation coefficients (squared) for correlation of HU measurements on images acquired using SECT at 80 kVp and the known concentration of each solute. ....	35
Table 9: Calculated sources of variation of a DXA aBMD measurement for a 25% concentration. The mean value and CV of the total variation are also shown for reference. The total variation is the sum of the individual variabilities added in quadrature. ....	36
Table 10: Pearson's correlation coefficients (squared) for correlation of aBMD measured by DXA with the known concentration of each solute. ....	37
Table 11: Comparison of GSI protocols assessed in Section 3.1.2. ....	40
Table 12: Calculated sources of variation of a solute concentration measurement in scattering conditions by DECT for a 25% concentration. The mean value and CV of the total variation are also shown for reference. The total variation is the sum of the individual variabilities added in quadrature.....	45



Table 13: Calculated sources of variation of a CT number measurement in scattering conditions at 120 kVp for a 25% concentration. The mean value and CV of the total variation are also shown for reference. The total variation is the sum of the individual variabilities added in quadrature.....	45
Table 14: Calculated sources of variation of a CT number measurement in scattering conditions at 80 kVp for a 25% concentration. The mean value and CV of the total variation are also shown for reference. The total variation is the sum of the individual variabilities added in quadrature.....	46
Table 15: Slope and y-intercept with 95% confidence intervals and squared Pearson's correlation coefficient for the linear regression comparing material density image concentration measurements acquired using GSI-5/6 protocols and on/10.5 cm above isocenter. The y-intercept with 95% confidence intervals was equivalent to 0 in the original regression in both cases, so the data were re-fit with a regression set to intercept the y-axis at $y = 0$ mg/mL. The probability of the slope of this regression being equivalent to unity was evaluated with an f-test. Significance in this experiment was defined as $p < 0.05$ .....	49
Table 16: Slope and y-intercept with 95% confidence intervals and squared Pearson's correlation coefficient for the linear regression comparing material density image concentration measurements made in air and in various scattering conditions. The y-intercept with 95% confidence intervals was equivalent to 0 in the original regression in all cases, so the data were re-fit with a regression set to intercept the y-axis at $y = 0$ . Significance in this experiment was defined as $p < 0.05$ . Note: Hom. = homogenous, Het. = heterogeneous. ....	50
Table 17: Slope and y-intercept with 95% confidence intervals and the squared Pearson's correlation coefficient for the linear regression comparing SECT concentration measurements made in air and in various scattering conditions at 120 and 80 kVp. The y-intercept with 95% confidence intervals was equivalent to 0 in the original regression in homogenous and heterogeneous scattering conditions in the body phantom at 80 kVp, so the data were re-fit with a regression set to intercept the y-axis at $y = 0$ HU. Note: Hom. = homogenous, Het. = heterogeneous. ....	52
Table 18: Variation between scans as an average CV of the mean measurement across all syringe-phantoms except for ethanol for DECT, SECT and DXA in air and in scattering conditions.....	56
Table 19: Description of concentric phantoms constructed for concentric phantom experiments. Each value is represented as a percent by volume concentration formatted as concentration of $K_2HPO_4$ by volume/concentration of Optiray 320 by volume. The 0%/0% concentric phantom contains only water in the inner and outer chambers. The 0%/0% and 10%/10% concentric phantoms were shared between the two sets.....	58
Table 20: Slope with 95% confidence intervals compared for a regression of the concentration measured in the concentric phantom vs the concentration measured in the uniform syringe-phantom. Each concentric phantom was scanned both in air and in scattering conditions and compared with the uniform syringe-phantom with both the equivalent concentration of $K_2HPO_4$ and Optiray 320 in those conditions. When the concentration of the material analyzed was fixed, it was expected that the slope of the regression would be 0. When the concentration of	

the material analyzed was changing, it was expected that the slope of the regression would be unity. Slopes considered different from expectation are marked with a \* ..... 64

Table 21: Slope with 95% confidence intervals compared for a regression of the HU measured in the concentric phantom vs the HU measured in the uniform syringe-phantom in air and in scattering conditions at 120 and 80 kVp. Each concentric phantom was scanned both in air and in scattering conditions and compared with the uniform syringe-phantom with both the equivalent concentration of  $K_2HPO_4$  and Optiray 320 in those conditions. When the concentration of the material analyzed was fixed, it was expected that the slope of the regression would be 0. When the concentration of the material analyzed was changing, it was expected that the slope of the regression would be unity. Slopes considered different from expectation are marked with a \* ..... 68

Table 22: Slope and offsets with 95% confidence intervals compared for a regression of the aBMD measured in the concentric phantom vs the aBMD measured in the uniform syringe-phantom. Each concentric phantom was scanned between eight 3/8 in. (9.5 mm) PMMA blocks and compared with the uniform syringe-phantom with both the equivalent concentration of  $K_2HPO_4$  and Optiray 320 in those conditions. When the concentration of the material analyzed was fixed, it was expected that the slope of the regression would be 0. When the concentration of the material analyzed was changing, it was expected that the slope of the regression would be unity. The expected offset is the measurement of the uniform syringe-phantom of equivalent concentration to the material being analyzed  $\pm$  the total variation in the uniform syringe-phantom measurement or 0 if the material being analyzed is changing in concentration. Slopes and offsets considered different from expectation are marked with a \* ..... 72

Table 23: The minimum discrete amount of  $K_2HPO_4$  by volume percentage and concentration that can be distinguished from water by each measurement method in air and in scattering conditions when applicable. The magnitude of each source of variation for that measurement method in the measurement of the listed concentration is also shown for comparison. .... 88

Table 24: The smallest detectable reduction in  $K_2HPO_4$  concentration from normal at the 95% confidence interval of the regression as a concentration and percentage of the normal value. The normal  $K_2HPO_4$  concentration equivalent vBMD for post-menopausal women is estimated at 126 mg/mL. .... 89

Table 25: The squared Pearson's correlation coefficient for each linear regression of the derived concentration using a given basis pair against the constituent basis pair for that series of syringe-phantoms..... 93

Table 26: Bland-Altman statistics of comparison between DECT HA aBMD and DXA aBMD. 105

Table 27: Bland-Altman statistics of comparison between SECT HA aBMD and DXA aBMD. 108



## List of Abbreviations

<b>aBMD</b>	Areal Bone Mineral Density
<b>AP</b>	Anteroposterior
<b>BMD</b>	Bone Mineral Density
<b>CV</b>	Coefficient of Variation
<b>CT</b>	Computed Tomography
<b>DXA</b>	Dual-Energy X-Ray Absorptiometry
<b>DECT</b>	Dual-Energy Computed Tomography
<b>DEQCT</b>	Dual-Energy Quantitative Computed Tomography
<b>DPA</b>	Dual-Photon Absorptiometry
<b>FOV</b>	Field of View
<b>GSI</b>	Gemstone Spectral Imaging
<b>HA</b>	Calcium Hydroxyapatite (Calcium Hydroxylapatite)
<b>HU</b>	Hounsfield Units
<b>K<sub>2</sub>HPO<sub>4</sub></b>	Dipotassium Phosphate (Dipotassium Hydrogen Phosphate)
<b>kVp</b>	Kilovolts Peak
<b>PA</b>	Posteroanterior
<b>QC</b>	Quality Control
<b>QCT</b>	Quantitative Computed Tomography

<b>ROI</b>	Region of Interest
<b>rsDECT</b>	Rapid-kVp-Switching Dual-Energy Computed Tomography
<b>SECT</b>	Single-Energy Computed Tomography
<b>SEQCT</b>	Single-Energy Quantitative Computed Tomography
<b>TBV</b>	Trabecular Bone Volume
<b>vBMD</b>	Volumetric Bone Mineral Density

## 1. Motivation

Osteoporosis is defined clinically as a measured bone mineral density (BMD) that is more than 2.5 standard deviations below the mean value for a reference population of healthy “young adults” aged 30-40 of the same gender and race imaged at the same site (1–3). This reduction in BMD results in a lower yield strength than normal bone, which translates to an increased fracture risk for patients (4,5).

Dual Energy X-Ray Absorptiometry (DXA) is the current gold standard for assessing BMD. The DXA scanner outputs an areal BMD (aBMD) with units of  $\text{g}/\text{cm}^2$  rather a true bone mineral density. Another modality that has been used for measuring BMD, although less frequently in the clinic, is single-energy computed tomography (SECT), which uses a single x-ray tube potential and measures tissue attenuation in Hounsfield units (HU). SECT may allow differentiation of trabecular bone from cortical bone, which is not possible with DXA. SECT used to make quantitative measurements of BMD using a reference phantom is referred to as single energy quantitative computed tomography (SEQCT). As a 3D technique, SEQCT may not be as susceptible as DXA to variations in measurement with bone size. However, SEQCT is susceptible to beam hardening artifacts, patient scatter, and the presence of fatty marrow which can be mistaken for reduced BMD (6–8).

Dual energy quantitative computed tomography (DEQCT) uses two x-ray tube potentials and provides a three-dimensional dataset like SECT but the use of two effective beam energies could theoretically allow for correction of beam hardening artifacts seen in SEQCT (9). More importantly, DEQCT also has the ability to identify the composition of a given voxel instead of only the net attenuation, potentially allowing more accurate assessment of bone composition. DEQCT was first implemented in the late 70's but in the past relied on two sequential single-energy scans on a conventional CT scanner and costly image preprocessing techniques. Additionally, the propagation of errors in data collected at two different energies rather than one reduced the reproducibility of DECT relative to SEQCT. A commercial DECT scanner is now

available that creates a dual-energy image with a single rotation utilizing a rapidly switching voltage across the cathode that results in a rapidly changing kVp (HD750, General Electric Medical Systems, Milwaukee, WI) and provides a ready-to-use software package capable of processing the dual-energy data (GSI Viewer, GEMS). This software offers the ability to decompose the signal from each voxel into the density of two user-defined materials assuming only those materials are present; for example, iodine and water. The two-material decomposition pairs are created by uploading a table of mass attenuation coefficients for the appropriate materials to the GSI Viewer software. Such a mapping has the potential to accurately assess BMD by modeling trabecular bone in terms of bone mineral (HA) and soft tissue, reducing the errors in SECT measurements.

However, the performance of the material decomposition feature of the rapid-kVp-switching DECT scanner has not been investigated extensively. There have to date not been any detailed studies investigating the performance of the DECT scanner using material decomposition to characterize bone composition. The objective of this study is to quantitatively investigate the sensitivity of GSI material decomposition images to known changes in the composition of several two-material samples in a variety of conditions and to evaluate its potential to assess BMD.

## 2. Introduction

### 2.1 Osteoporosis and Bone Mineral Density

Human bones are comprised of two distinct compartments. The outer cortical compartment consists mostly of a dense tissue comprised of calcium hydroxyapatite (HA) and collagen, often referred to as “bone mineral” or “bone material.” The cortical bone forms a shell around the inner trabecular bone, also known cancellous bone. Trabecular bone consists primarily of bone mineral, red marrow, which produces blood cells, and yellow marrow, which is mostly fat. Bone mineral density (BMD) is the amount of bone material in a given volume of bone, typically per cubic centimeter.

Osteoporosis is defined as “a disease characterized by low bone mass and microarchitectural deterioration of bone tissue, leading to enhanced bone fragility and a consequent increase in fracture risk (10).” Osteoporosis is defined clinically as a measured bone mineral density or bone mineral content that is more than 2.5 standard deviations below the mean value for a reference population of young adults of the same gender and race imaged at the same skeletal site (1,2). The standard deviation from the mean value is known as the T-score. A similar metric is the Z-score, for which the reference population is the patient’s own age group. The mean BMD for healthy women can vary by as much as 30% between reference populations (11). Bone mineral loss is known to increase with age, at greater rates in women than men (12–15). The normal incidence of osteoporosis increases with age, with 5% of women in western populations aged 50-54 estimated to have the disease, and up to 60.5% of women aged 85 or older (1). In postmenopausal women, osteoporosis is attributed to reduced estrogen levels. One action of estrogen is to partially block the resorption of bone stimulated by parathyroid hormone (16,17). In both women and men, bone loss may also result from a reduction of calcium absorption in the gut from dietary sources beginning in ages 55-60 and 65-70 respectively and low rates of new bone formation (12,18). Bone fractures and spinal compression are associated with osteoporosis, and it is therefore considered a disease (12).

While osteoporosis is a natural consequence of aging, there are several other known causes of reduced bone mineral (19,20). One of these is an increased risk of bone mineral loss secondary to some forms of cancer treatment (21–23).

While there are many factors proposed to be associated with fracture risk (2,24,25), the reduced bone mineral density (BMD) associated with osteoporosis is thought to be most predictive (2). Bone mineral density is defined as the amount of bone mineral (HA) “per unit volume of the organic bone matrix (3).” The BMD of osteoporotic bone is reduced primarily in the trabecular compartment (26,27) due to the larger surface area to volume ratio and metabolic activity (28,29).

Trabecular bone in patients diagnosed with osteoporosis is known to have similar bone material composition and density to normal bone; it is the trabecular bone volume (TBV) that is reduced through loss of entire structural elements (4,14,27,30). This reduction in TBV results in a lower yield strength than normal bone in mechanical stress tests and severe changes are associated with compression fractures (1,4,5,30). The decrease in TBV coincides with an age-related increase in fat in the marrow, although the effects are not necessarily related (8,13,31–35).

A number of different anatomical sites have been proposed and investigated for the assessment of trabecular BMD for fracture risk. Numerous studies have supported the recommendation that BMD is best assessed at the anatomical site which is thought to be at risk of fracture (15,36,37). Currently the lumbar spinal vertebrae are one of the most frequently monitored sites of BMD. This is in part because the lumbar spine is particularly prone to fracture; in osteoporosis these fractures are associated with an increased risk of hospitalization and mortality (38). The lumbar spine is also preferred because of the large proportion of trabecular bone in the lumbar vertebrae relative to the rest of the skeleton. Correspondingly, the lumbar spine experiences a larger decrease in BMD in osteoporosis (15,39).

## 2.2. Measurement of Bone Mineral Density

Measurement of trabecular BMD demands a methodology that is accurate, repeatable, sensitive, and correlated with probability of fracture (2,40). Numerous methods for assessing BMD have been developed since 1964 (41). Three technologies of interest in this investigation are dual-energy x-ray absorptiometry (42), single-energy computed tomography (43,44), and dual-energy computed tomography (45).

### 2.2.1. Dual Energy X-Ray Absorptiometry

Dual Energy X-Ray Absorptiometry (DXA) is the current gold standard for assessing BMD. The modality gained rapid acceptance; a study by Intenzo et al. found that four times as many Medicare patients had a DXA examination performed in 2002 as in 1996 (2,195,548 vs 510,105), an increase they attributed to “demographics, heightened public awareness of osteoporosis, and advances in therapy (46).” DXA is favored because it is non-invasive and precise, with a reported 0.5-2% coefficient of variation (CV) for posteroanterior (PA) lumbar spine measurements (47). The DXA scanner creates a radiograph with two x-ray beams generated from bremsstrahlung radiation at two different peak tube potentials (kVps). In the DXA implementation by Hologic (Hologic, Bedford, Massachusetts), the x-ray source switches between high and low kVp resulting in polychromatic beams with high and low effective energies (48) that are attenuated by soft tissue and bone according to the Beer-Lambert law and the energy-dependent mass attenuation coefficient ( $\mu/\rho$ ). In principle, the two different effective energies allow the determination of the areal density  $M$  of one material (bone,  $B$ ) without contribution of the other (soft tissue,  $S$ ) from the integrated high and low-effective energy x-ray beam transmissions  $I_H$  and  $I_L$ , as illustrated in the DPA equation (49) (Equation 2.2.1-5) derived below:

$$I_L = I_{L,0} e^{-\left(\frac{\mu}{\rho_{S,L}} M_S + \frac{\mu}{\rho_{B,L}} M_B\right)} \quad \text{Equation 2.2.1-1}$$

$$I_H = I_{H,0} e^{-\left(\frac{\mu}{\rho_{S,H}} M_S + \frac{\mu}{\rho_{B,H}} M_B\right)}. \quad \text{Equation 2.2.1-2}$$

By taking the logarithm of both sides and setting  $J = -\ln(I/I_0)$ , Equation 2.2.1-1 and 2.2.1-2 may be re-written as

$$J_L = \frac{\mu}{\rho_{S,L}} M_S + \frac{\mu}{\rho_{B,L}} M_B \quad \text{Equation 2.2.1-3}$$

$$J_H = \frac{\mu}{\rho_{S,H}} M_S + \frac{\mu}{\rho_{B,H}} M_B. \quad \text{Equation 2.2.1-4}$$

Equation 2.2.1-3 or Equation 2.2.1-4 can be written in terms of  $M_S$  and substituted into the other and solved for  $M_B$ :

$$M_B = \frac{J_L - \left(\frac{\mu}{\rho_{S,L}} / \frac{\mu}{\rho_{S,H}}\right) J_H}{\frac{\mu}{\rho_{B,L}} - \left(\frac{\mu}{\rho_{S,L}} / \frac{\mu}{\rho_{S,H}}\right) \frac{\mu}{\rho_{B,H}}}. \quad \text{Equation 2.2.1-5}$$

In equation 2.2.1-5, the terms  $\frac{\mu}{\rho_{B,L}}$  and  $\frac{\mu}{\rho_{B,H}}$  are known from the effective energy of each beam and the composition of bone mineral (hydroxyapatite) (50). The ratio  $\frac{\mu}{\rho_{S,L}} / \frac{\mu}{\rho_{S,H}}$  is calculated as  $J_L/J_H$  either for each scan line or averaged over all regions containing only soft tissue (50,51), since the composition of the soft tissue is not known. At MD Anderson, most DXA examinations include an anteroposterior (AP) measurement of the lumbar spine. The typical screening examination is vertebrae L1-L4 and each femoral neck.

The widespread use of DXA has resulted in a large body of normative data from which an individual diagnosis of osteoporosis can be made (11,52–58). Despite its ubiquitous use, however, DXA has an important drawback. The scanner outputs a bone mineral “density” with units of  $\text{g/cm}^2$ , which is not a true bone mineral density but in fact an estimate of bone mineral content within a given areal projection. This is often referred to as an areal bone mineral density, or aBMD. Because it is not a true volumetric density, an aBMD measurement is



necessarily an inaccurate measurement of true BMD. Additionally, although the quantity of interest is BMD of the trabecular portion of the bone, due to the two-dimensional nature of DXA imaging cortical bone mineral is incorporated into the aBMD as well. As a result, the sensitivity of DXA is theoretically reduced, which impacts its effectiveness as a screening modality (58).

### 2.2.2. Single-Energy Computed Tomography

Single energy computed tomography (SECT) is an alternative noninvasive method for quantitative bone analysis (40). Like DXA, SECT images are produced by integral measurements of x-ray attenuation in tissue. A computed tomography (CT) scanner creates a three-dimensional image dataset from the rotation of an x-ray tube and detector (x, y axes) and patient translation (z axis), most often using a filtered back-projection reconstruction in which each beam profile is deconvolved with a sharpening kernel and then superimposed in image space over 360 degrees (59,60). The resulting images are attenuation maps defined by the characteristic linear attenuation coefficient ( $\mu$ ) of the tissues in the field of view (FOV). Each volume element or “voxel” of the image is associated with a Hounsfield unit (HU) (also called CT number) that is defined as

$$HU(E, x, y, z) = 1000 \times \frac{\mu(E, x, y, z) - \mu(E)_w}{\mu(E)_w} \quad \text{Equation 2.2.2-1}$$

where  $\mu(E)_w$  is the linear attenuation coefficient of water. Because  $\mu$  is a function of energy ( $E$ ), SECT acquisitions with different kVps will yield different HU for the same tissue.

While trabecular BMD is sometimes assessed in terms of the average HU in a region of interest (ROI) (61,62), typically for BMD assessment the CT device is calibrated with a known standard to output units of true density (usually  $\text{mg}/\text{cm}^3$  or  $\text{mg}/\text{mL}$ ). This approach is commonly referred to as quantitative computed tomography (QCT).

Single-energy QCT (SEQCT) for the assessment of bone composition has been in use since 1976 (43,44). Historically, SECT measurements were calibrated with known

concentrations of dipotassium phosphate ( $K_2HPO_4$ ) in water (26,27,63–65). Dipotassium phosphate is a useful substitute for bone material due to its similar effective atomic number, physical density, and linear attenuation coefficient  $\mu_E$  for effective energies in the range of CT, as well as its solubility in water (63,66). Solid phantoms of varying concentrations of HA in water-equivalent plastic have also been used (65,67). In QCT studies investigating the influence of fat in the marrow space on measurements, ethanol has often been used as a fat substitute (33,66,68,69) due to its similar mass attenuation coefficient and its solubility in water. Water-soluble materials allow for completely uniform phantom composition assuming they do not precipitate out of the solution.

SEQCT outputs a true volumetric bone mineral density (vBMD), a potentially major advantage over DXA. The three-dimensional nature of SECT data also allows for differentiation between the trabecular and cortical compartments of bone. The potential for bone densitometry measurements with CT was realized not long after the introduction of the device (43,44,70). Within its first decade, SECT became established as a useful alternative to single and dual-photon absorptiometry, planar imaging predecessors of DXA that used radioisotopes rather than x-rays, for the assessment of bone mineral density (71). SEQCT bone mineral assessment available in the mid-90's had precision errors (CVs) of 2-4% (40); modern-day SEQCT with multislice helical scanners has improved this to a 1.4% "best case" precision error and a 3.6% "worst case" error, with a routine measurement estimated to have a precision error of 1.8% (72). SEQCT is generally more sensitive to changes in bone mass than projection technologies (40,73). In a cross-sectional study of 108 postmenopausal women conducted by Gulgielmi et al., SEQCT estimated a rate of bone loss in the lumbar spine over four times greater than the rate estimated by PA DXA (1.96% vs 0.45%) (74). The same study also found that SEQCT was a significant predictor of osteoporosis in the lumbar spine, but PA DXA was not. In general, SEQCT BMD has been found to be at least as predictive of fracture risk as AP DXA aBMD in the lumbar spine for postmenopausal women (25).

Despite the demonstrated utility of SEQCT, there are a number of disadvantages that prevent it from being the preferred screening method for generalized fracture risk. Although QCT may be implemented on existing SECT scanners, a DXA scanner is less expensive to acquire and operate and has no other demands placed on it other than the assessment of BMD. In addition, a SEQCT spine examination delivers 1.2-120× more radiation dose to the patient than a DXA spine examination (0.016-1.5 mSv depending on type of examination for SEQCT vs. 0.013 mSv for DXA) (75). SEQCT is also a less precise modality than DXA due to the more numerous scan parameters, in which variations contribute to the total error (72,76).

While the true density measurements of vBMD are more accurate characterizations of bone tissue than DXA aBMD, SEQCT suffers from other sources of inaccuracy. A well-studied limitation on SEQCT measurements is beam hardening (6,77,78), a phenomenon that results from the polyenergetic x-ray spectrum used to produce the images (the effect is present in DXA as well (79)). As the polyenergetic beam travels through a patient, lower-energy x-ray components of the beam are attenuated. The result is a net shift upward in the effective energy of the beam (“hardening”), resulting in lower attenuation measurements than expected. Because of these lower HU measurements, beam hardening artifacts affect SEQCT primarily by reducing the observed vBMD (64,80). Beam hardening can be addressed and corrected in a number of ways in SEQCT, including empirical modeling (80), calculations based on assumed materials present in the image (81), and reference phantoms (6). However, none of these methods are completely capable of removing beam hardening artifacts in an individual examination.

SEQCT measurements are also confounded by the effects of x-ray scatter. In the range of effective energies used in CT examinations, “scatter” refers primarily to Compton scatter, which has the dominant interaction cross section or probability of interaction in water (compared to the photoelectric effect, which has the next largest cross section). Compton scatter is an inelastic process in which an x-ray photon collides with a free charged particle (in

a patient, usually an electron) and a scattered x-ray photon with reduced energy leaves the collision site at an angle to the original path. In CT imaging, this scattered x-ray photon is detected by the imaging equipment but the signal does not correspond to the original (“primary”) beam path, so it appears as noise and degrades the contrast of the resultant image along with other background noise sources.

Another consequence of scatter was illustrated by Glover (82). The total intensity  $I_t$  of radiation at the detector can be represented as a sum of the contributions of the intensity of the primary beam  $I_p$  and of the total scattered radiation  $I_s$ :

$$I_t = I_p + I_s. \quad \text{Equation 2.2.2.-2}$$

The detected x-ray attenuation is logarithmically transformed during the reconstruction process, so equivalently

$$\log(I_t) = \log I_p \left( 1 + \frac{I_s}{I_p} \right). \quad \text{Equation 2.2.2-3}$$

If the scatter to primary ratio  $I_s/I_p$  is much smaller than 1, eq. 2.2.2-3 may be re-written:

$$X_t = X_p - \frac{I_s}{I_p} = X_p + X_s \quad \text{Equation 2.2.2-4}$$

where  $X_t \equiv -\log I_t$ ,  $X_p \equiv -\log I_p$  and  $X_s \equiv I_s/I_p$ . The result is the measured total logarithmic attenuation  $X_t$  is reduced from the expected measurement by an amount equivalent to the scatter to primary ratio. When the x-ray beam passes through a highly attenuating region, there is a much greater decrease in  $I_p$  than  $I_s$  so a noticeable decrease in HU from the expected value will be observed. An example is when a flat x-ray beam with no primary attenuator encounters a homogenous water-filled cylindrical phantom meant to represent a patient. The beam is unevenly attenuated by the patient and so a “cupping” artifact is observed, in which the HU measured in the center of the phantom is less than HU measured around the edges. This effect is compensated for in CT scanners with the use of a bowtie filter, an attenuating object shaped in such a way to ensure the beam is roughly uniformly attenuated along its entire

profile. Different-sized patients necessitate different-sized bowtie filters. This selection is never exact and as a result patient size is known to affect SEQCT measurements (7,83,84).

The accuracy of SEQCT is perhaps most dramatically affected by the amount of fat in trabecular bone. Because SEQCT is calibrated with varying compositions of bone mineral equivalent material in water and because fat is less attenuating than water (typically -50 to -100 HU compared to 0 HU for water), the presence of fat in the marrow space causes a systematic error in SEQCT measurements. Because marrow makes up approximately 75-80% of trabecular bone, and fat approximately 25-75% of marrow, the systematic error can be large (85). In addition, the presence of unknown quantities of fat causes an underestimation of vBMD of 10-30% at 80 kVp and 20-40% for tube potentials up to 130 kVp (8). An adjustment of SEQCT measurement can be made based on normative data on fat content over age and the underestimation of vBMD over fat content (86). However, individual variation in vertebral fat still accounts for 12-24% of the residual inaccuracy at 80 kVp and 30-40% up to 130 kVp.

### **2.2.3. Dual Energy Computed Tomography**

Dual-energy computed tomography (DECT) has the potential to overcome the limitations on accuracy of SPECT. Dual-energy computed tomography, first proposed simultaneously with SPECT (70), utilizes the same imaging methodology as single-energy computed tomography, but with acquisitions at two effective x-ray energies instead of one. When attenuation data have been acquired at two different effective energies, either a preprocessing (projection based) technique (9) may be applied to the raw data or a postprocessing (image based) technique (87) may be applied to the resulting image sets to create new images that are able to distinguish between two different materials in a given voxel rather than providing a net attenuation measurement. A preprocessing technique is advantageous because it is in theory free of beam hardening artifacts due to the decomposition functions used (88,89). However, preprocessing is technically challenging and requires access to the raw data; until recently the technique was limited to a few research centers (90,91).

The most studied preprocessing technique is based on the work of Alvarez and Macovski (9). The method relies on the principle that the linear attenuation coefficient  $\mu(E)$  of a given material varies with the effective energy of an x-ray beam according to a linear combination of the photoelectric effect and Compton scattering. The cross section of the photoelectric effect is inversely proportional to the third power of effective energy ( $E^{-3}$ ), whereas the cross section of Compton scattering is described by the Klein-Nishina formula  $f_{KN}(E)$ , as described in the paper. The linear attenuation coefficient in a given (multislice) CT image, through empirical testing, is approximated by the function

$$\mu(x, y, E) = a_1(x, y, z) \frac{1}{E^3} + a_2(x, y) f_{KN}(E). \quad \text{Equation 2.2.3-1}$$

The coefficients  $a_1$  and  $a_2$  depend on the atomic number  $Z$ , mass density  $\rho$ , and atomic weight  $A$  of the material, such that

$$\begin{cases} a_1 \approx K_1 \frac{\rho}{A} Z^n \\ a_2 \approx K_2 \frac{\rho}{A} Z \end{cases}, \quad \text{Equation 2.2.3-2}$$

where  $K_1$  and  $K_2$  are empirical constants,  $n \approx 4$ , and all parameters except for  $n$  are dependent on the location in the image  $(x, y)$ . An individual photon in the x-ray beam of the CT scanner measures the line integral of  $\mu(x, y, z, E)$ , that is,

$$\int \mu(x, y, z, E) ds = A_1 \frac{1}{E^3} + A_2 f_{KN}(E) \quad \text{Equation 2.2.3-3}$$

where

$$A_1 = \int a_1(x, y, z) ds \text{ and } A_2 = \int a_2(x, y, z) ds. \quad \text{Equation 2.2.3-4}$$

If two measurements were made with x-rays beams of two different energy spectra  $S_1$  and  $S_2$ , then the two different intensity measurements  $I$  can be obtained:

$$\begin{cases} I_1(A_1, A_2) = T \int S_1(E) e^{-A_1/E^3 - A_2 f_{KN}(E)} dE \\ I_2(A_1, A_2) = T \int S_2(E) e^{-A_1/E^3 - A_2 f_{KN}(E)} dE \end{cases} \quad \text{Equation 2.2.3-5}$$

where  $T$  is the total measurement time and  $I$  is the total energy. Through these two intensity measurements, the coefficients  $A$  may be derived. If two materials (a basis pair) are assumed to be in a given voxel or conversely if a constant density is assumed, the density (and for most materials, the electron density) or material properties (atomic number, mass) can be obtained. The former method can be used to produce two material decomposition image sets, where the voxels in each set represent the density of one material assuming the other is present. Separation of the spectra is important for dual-energy reconstruction; the lower-energy beam should be attenuated a relatively large amount by the more material sensitive photoelectric interactions, while the higher-energy beam should be dominated by Compton scattering; in principle greater separation between the two images gives greater material discrimination. However, the more the lower energy beam becomes attenuated, the more the signal to noise ratio decreases (92).

It is important to note that the equations in (13) are non-linear and cannot be solved exactly. The choice of reconstruction function will impact the accuracy of any preprocessed DECT measurement. It is also important to note that the Alvarez and Macovski method does not address the problem of scattered radiation (9). It is also important to note that unlike in DXA dual-energy reconstructions, the two materials used in DECT material decomposition image sets are input by the user and assumed to be known. Density for each basis pair material is derived solely from first principles. DXA, by contrast, only assumes one material is known (HA) and applies an empirical correction to the areal density based on indirect measurements of the second material (soft tissue). In this way, DXA essentially normalizes the density measurement for each individual patient whereas no normalization is applied in DECT acquisitions. While DXA aBMD is assessed daily with a quality control (QC) phantom provided by the manufacturer, there is currently no similar calibrated standard for assessing DECT density measurements.

In principle, there are a number of ways to implement DECT acquisition. The simplest method to obtain two spectra is to simply repeat a SECT scan twice at different kVps (93,94).

However, due to the sequential nature of the scans, this method is prone to image artifacts caused by patient motion in a clinical situation. An implementation involving a single scan is preferred. In one proposed implementation, a split filter of differing thickness is placed over the tube window such that the beam on one side of the filter passes through more attenuating material and is harder than the beam on the other side (95). In another, the detector is split such that the two sides are more sensitive to higher and lower-energy photons (96). Besides poorer discrimination between Compton scattering and the photoelectric effect, these (research) methods also prevent single-energy acquisitions on the same scanner. One solution is an implementation in which two sources set to two different kVps are set at  $90^\circ$  from one another and rotated around the patient simultaneously paired with two detectors (97). The current most commonly used implementation method has the disadvantage of reducing the effective FOV of the scanner when used for DECT due to the small size of one of the detectors used (98) and also relies on postprocessing imaging techniques that do not compensate for beam hardening (89). Another implementation involves a single source that rapidly switches between two kVps paired with a single detector (99,100).

One of the first applications of DECT was quantitative assessment of bone mineral (DEQCT) (45) by Genant et al. using sequential scanning and postprocessing. A follow-up study conducted a much more in-depth characterization of the technique (68). Genant and Boyd measured the CT number and fraction  $K_2HPO_4$  of varying solutions of  $K_2HPO_4$  in water and  $K_2HPO_4$ –water–ethanol in single-chamber cylinders to simulate cortical and trabecular bone and in concentric cylinders to simulate bone geometry. The two chambers (trabecular and cortical) of the concentric phantom were measured separately and as an integral. The investigators found excellent correlation of CT number with  $K_2HPO_4$  in both the solid and concentric cylinders and lower than expected CT numbers in the middle of cylinders with thick cortical bone, indicating beam hardening error. In measurements of the  $K_2HPO_4$  concentration, DEQCT was found to have greater accuracy, far less susceptible to ethanol concentration, but



less precision. The investigators concluded that DEQCT might be more useful for diagnosis and SEQCT for follow-up.

Many subsequent studies confirmed these results (76,85,94,101). In the late '80s, DEQCT studies were reporting a standard error of the estimate of 3-6% in normal women and 6-10% in older women, compared to 6-9% and 10-15% respectively with SEQCT, but a three to fourfold reduction in precision and a doubling of dose (73,102). Research in DEQCT for vBMD measurement mostly ceased by 1996, when Genant et al. published a literature review on noninvasive bone analysis that briefly concluded the poorer precision and higher dose of the technique made it suitable only for research applications (40).

Recently, interest in DECT has re-emerged with the advent of the first commercial DECT scanner in 2006 (97). A variety of studies have been published on the potential clinical application of these scanners (103–105). However, we are not aware of any studies to date assessing the capability of these new DECT scanners for characterizing BMD. A commercial DECT scanner with rapid kVp switching (rsDECT) and dual-energy preprocessing modeled after the methods of Alvarez and Macovski is now available (100). The GE HD750 (General Electric Medical Systems, Milwaukee, WI) includes pre-packaged image analysis software called GSI Viewer (General Electric Medical Systems, Milwaukee, WI) that allows for two-material decomposition image sets to be created based on user-defined material basis pairs. The purpose of this present study is to characterize this feature of the scanner and its potential for vBMD measurement.

## 2.4. Hypothesis and Specific Aims

**Hypothesis:** Rapid-kVp-switching dual energy computed tomography (DECT) is capable of producing material density images with an accuracy better than 95% which are more sensitive to changes in bone-equivalent material than dual-energy absorptiometry (DXA) and can be related to DXA areal bone mineral density (aBMD) measurements to distinguish osteoporotic from normal bone within a 95% confidence interval.

**Specific Aim I:** To quantitatively investigate the performance of material density concentrations, SECT, and DXA to known changes in the composition of several two-material samples.

- Subaim 1: To determine the accuracy of DECT material decomposition when characterizing two-material samples using the constituent material decomposition basis pairs and to compare the performance and sources of variability of DECT material density images, SECT, and DXA for a variety of imaging conditions.
- Subaim 2: To compare the performance of DECT material density images, SECT, and DXA in a concentric phantom designed to simulate the geometry of bone.
- Subaim 3: To evaluate the relative sensitivity of DECT material density images, SECT, and DXA to changes in  $K_2HPO_4$  concentration.
- Subaim 4: To quantitatively investigate the correlations between several constituent and non-constituent DECT basis pairs for given two-material samples.

**Specific Aim II:** To quantitatively investigate the relationship between DECT material density concentrations and DXA measurements and compare a DECT and SECT-derived aBMD with DXA.

- Subaim 1: To analyze the correlation of DECT concentration measurements using the  $K_2HPO_4$ -water basis pair with DXA aBMD measurements.
- Subaim 2: To develop a methodology to calculate DECT and SECT-based areal bone mineral density in  $g/cm^2$  of HA and investigate the correlation of each to DXA-based aBMD.

### 3. Specific Aim I: Performance of DECT and Measurement Method Comparison

#### 3.1. Subaim 1: Accuracy of DECT and Comparison of Measurements

##### 3.1.1. Material Decomposition Accuracy

###### 3.1.1.1. Materials and Methods

A characterization of the accuracy of material density image-derived concentration measurements was sought. Syringe-phantoms were designed to assess the accuracy of the material density images in the simplest case of decomposing two-material samples into their constituent basis pairs. Seven 30 mL solutions of iodinated contrast (Optiray 320, Mallinckrodt Pharmaceuticals, St. Louis, MO) and water, ethanol and water, dipotassium phosphate ( $K_2HPO_4$ ) and water, and a 10 gm%  $K_2HPO_4$  and water solution plus denatured ethanol were prepared in 60 mL syringes with a diameter of 2.5 cm. The materials were selected due to their ubiquitous use as CT contrast (Optiray 320), and as bone ( $K_2HPO_4$ ) and fat (ethanol) surrogates in CT research. The syringe-phantoms containing both 10 gm%  $K_2HPO_4$  solution and ethanol were constructed (106) to model the composition of trabecular bone, containing both fatty yellow marrow and bone material.

The concentration of each solute (Optiray 320, ethanol, and  $K_2HPO_4$ ) varied in 5% by volume increments from 0-30%, for a total of 21 solutions. For the additional seven 10 gm%  $K_2HPO_4$  solution-ethanol syringe-phantoms, the ethanol concentration was varied in 5% by volume increments from 0-30% representing progressively more yellow marrow. However, for the remainder of this paper the 10 gm%  $K_2HPO_4$  solution is considered the “solute” since, representing bone material, it is the material of interest. These concentrations were selected to give a broad range of material densities for each solute, particularly for the  $K_2HPO_4$ , which nears its precipitation point at 30% concentration.

In preparing solutions containing  $K_2HPO_4$ , the  $K_2HPO_4$  powder was weighed on a gram scale with an approximate uncertainty of  $\pm 0.001$  g provided by the manufacturer. Distilled water

and ethanol were measured out in 5 and 1 mL volumetric pipettes with an estimated uncertainty of 0.01 mL each.  $K_2HPO_4$  is known to create an excess volume when dissolved in water (107) so the concentration was adjusted based on volumes measured with the syringes. The uncertainty in volume from syringe measurements ( $\pm 0.05$  mL) was translated to error bars in subsequent analysis (Section 3.1.1.2.1). The excess volume effect is also known for ethanol added to water, and the concentration was adjusted according to fourth-order polynomial fit to partial volume tables found in Benson and Kiyohara (108). This effect is notably much smaller than for  $K_2HPO_4$ . Excess volume data was not available for Optiray 320-water and  $K_2HPO_4$ -water-ethanol solutions, but visual assessment of the syringe-phantoms determined that volume corrections were not necessary.

Scans were acquired with the GE HD750 dual-energy CT scanner using the GSI-6 dual-energy protocol (medium body filter, rotation time 1s, beam width 40 mm,  $CTDI_{vol}$  33.43 mGy). Each syringe-phantom was placed in the central bore of an electron density phantom (Model 62, CIRS, Norfolk, VA), which measures 13 x 2 x 10.6 in. (33 x 5.1 x 27 cm), with the portion containing the solution protruding in air and the central bore aligned at isocenter (Figures 1-2). Eight 5 mm images were acquired and reconstructed using the GE GSI viewer software into material density maps using the constituent basis pair (for example, Optiray 320 and water). The mass attenuation coefficients for each material in the basis pair loaded to the GSI software were taken from the NIST database using XCOM (109), except for water, which was available as a pre-determined material. Optiray 320 was programmed as a mixture according to the composition listed in the package insert. For each syringe-phantom, the mean solute concentration and standard deviation was recorded from a circular region of interest (ROI) of 250-259 mm<sup>2</sup> drawn in the center of the transaxial area of the syringe (Figure 3) in the central image (image 4 or 5).



Figure 1: CIRS 62 electron density phantom, pictured with included tissue-equivalent inserts placed in bores. The inner “head” portion can be removed or it can remain in place to simulate a “body” measurement.

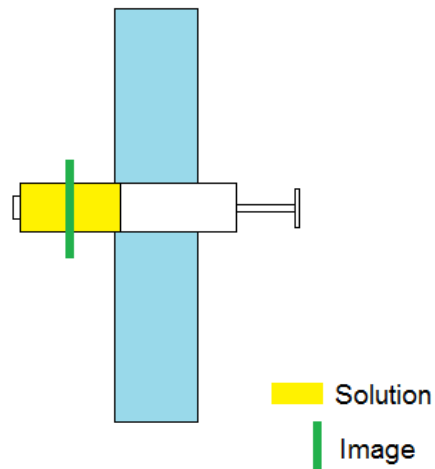
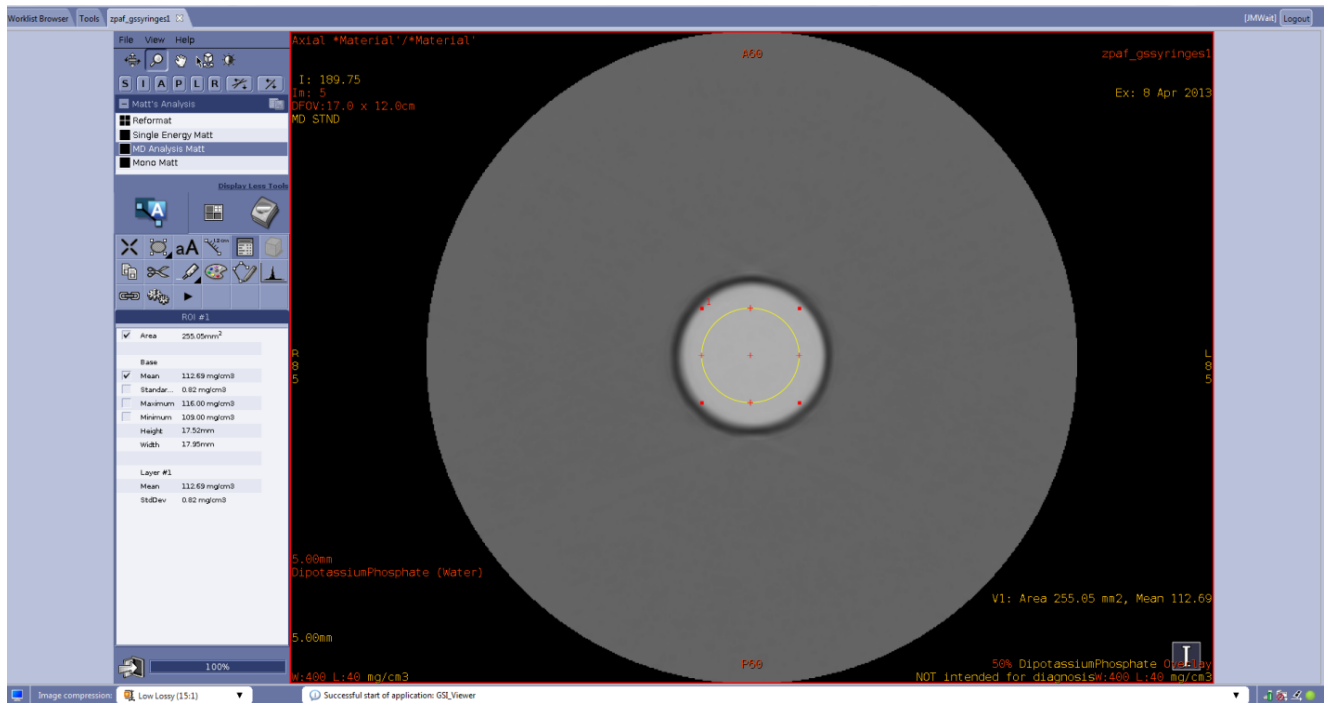


Figure 2: Configuration of materials used for in-air DECT and SECT measurements. Each syringe-phantom was inserted in the central bore of the electron density body phantom with the solution protruding in air. Eight images that span the solution volume were acquired, and a measurement was made on the central image (image 4 or 5) as shown.

Figure 3: Illustration of procedure for making material density measurements in GSI Viewer.

The image shown is a material density map; a circular ROI is drawn in the cross-section of the syringe-phantom.



For comparison, immediately following the DECT scans, axial SECT images were acquired sequentially at 120 kVp/150 mA and 80 kVp/200 mA with 1s tube rotation time and the medium body filter selected. The corresponding mean and standard deviation of the CT number were measured in the GSI Viewer software and recorded for all image sets using the same ROI size range and approximate position as the concentration measurements. The syringe-phantoms were also scanned individually with a DXA scanner (Discovery, Hologic, Bedford, MA) with each syringe-phantoms placed horizontally between five 3/8 in. (9.5 mm) thick PMMA slabs on top and three slabs beneath to simulate patient scattering conditions in a lumbar spine measurement (Figure 4). aBMD measurements were made using vendor supplied software in lumbar spine analysis/subregion array spine mode by manually drawing a rectangular ROI over the central axis of the syringe-phantom to segment the “bone” region

(Figure 5). The Hologic Discovery scanner produces x-ray beams with switching tube potentials of 100 and 140 kVp.

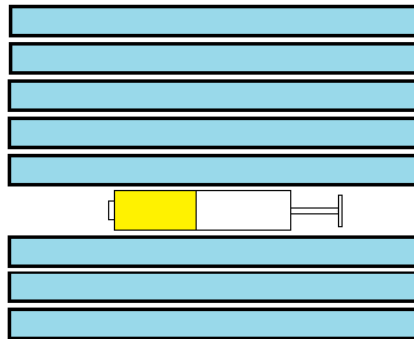


Figure 4: Positioning of syringe-phantom for DXA measurement. Five 3/8 in. (9.5 mm) PMMA slabs are placed above and three below to simulate patient scattering conditions in a lumbar spine measurement.

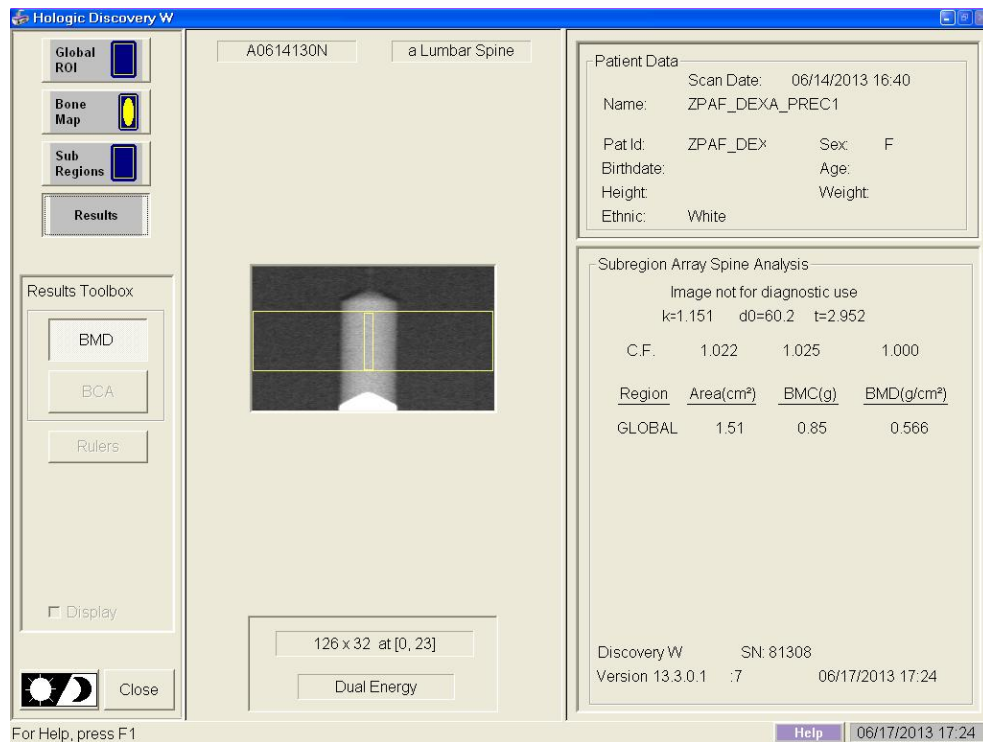


Figure 5: DXA measurement of a two-material syringe-phantom with the vendor-provided software. A "bone map" was manually drawn on the central axis. The BMD was reported in areal density (g/cm<sup>2</sup>).



The material density image-derived solute concentrations were compared with the known concentrations and the data was fit with a linear regression. The Pearson's correlation coefficient ( $r$ ) was computed. The probability of a slope of unity and the probability of a y-intercept equal to 0 were determined with an f-test using GraphPad Prism 6 statistical analysis software (GraphPad Software, La Jolla, CA). Regressions with a y-intercept consistent with 0 within the 95% confidence intervals were re-plotted with the y-intercept set to 0. The accuracy was evaluated by calculating the total root mean square (RMS) error and the RMS error as a coefficient of variation (CV) of the solute across all concentrations for the relevant syringe-phantoms. The material density image-derived solute concentrations and the known concentrations were also compared using Bland-Altman analysis (110).

An evaluation of the different sources of variation in the DECT scanner measurements was necessary in order to determine the accuracy of the concentration measurements from the material density images. Four sources of variation were identified: variation in phantom preparation ( $\sigma_p$ ), variation between images in each acquisition ( $\sigma_i$ ), variation between acquisitions ( $\sigma_r$ ) and random variation in concentrations across the ROI or noise ( $\sigma_n$ ).

In order to estimate variation in phantom preparation,  $\sigma_p$ , four 25% Optiray 320 syringe-phantoms and three 2.5%  $K_2HPO_4$  syringe-phantoms were independently prepared. These concentrations were selected to represent estimated "worst-case" variation for the two respective materials based on the phantom preparation method. These syringe-phantoms were scanned with DECT using the same methodology as described for the other syringe-phantoms. The phantom preparation variation  $\sigma_p$  was not evaluated for ethanol and 10gm%  $K_2HPO_4$  solution syringe-phantoms because due to the large inaccuracies observed relative to the other syringe-phantoms, it was judged not worth the time and financial resources to obtain the relevant data. In order to estimate variation between images,  $\sigma_i$ , the standard deviation of the mean was determined from DECT data in the same location on an eight-image stack of three concentrations (10, 20, 30%) of each solute or ethanol. The two outermost images (Images 1

and 8) for each stack were found to have partial volume artifacts with air and the electron density phantom respectively and were not included in the analysis. To estimate variation between scans,  $\sigma_r$ , a single 25% Optiray 320, a single 2.5%  $K_2HPO_4$  syringe-phantom, and the 25%-ethanol 10 gm%  $K_2HPO_4$  solution syringe-phantom were scanned three times on three separate dates using the methodology described earlier in this section, and the standard deviation of the mean concentration was determined. The  $\sigma_r$  was not evaluated for ethanol. Finally, the noise ( $\sigma_n$ ) of each measurement of all Optiray 320, ethanol,  $K_2HPO_4$ , and 10 gm%  $K_2HPO_4$  solution concentrations was defined as the standard deviation of the mean. The total standard deviation  $\sigma_t$  of each mean concentration was then calculated from combining these four standard deviations in quadrature. The phantom preparation variation  $\sigma_p$  was not included in the total variation for any syringe-phantom containing only water.

For comparison, the same method was used to calculate each variation for SECT and DXA measurements, using the same syringe-phantoms to calculate  $\sigma_p$ . The differing nature of DXA aBMD measurements required only  $\sigma_p$  and  $\sigma_r$  to be evaluated. DXA produces a single image rather than an image stack and the standard deviation or variability or “variation” of the measurement displayed is not provided by the DXA software.

### **3.1.1.2. Results**

#### 3.1.1.2.1. DECT Accuracy

The magnitude of each source of variation for each two-material syringe-phantom imaged with DECT is summarized for a representative concentration in Table 1. Measurements of the ethanol syringe-phantoms in general had the highest variation.

Table 1: Calculated sources of variation of a solute concentration measurement in air by DECT for a 25% concentration. The mean value and CV of the total variation are also shown for reference. The total variation is the sum of the individual variabilities added in quadrature.

DECT Variation (Air)	Optiray 25% (mg/mL)	Ethanol 25% (mg/mL)	K <sub>2</sub> HPO <sub>4</sub> 25% (mg/mL)	10 gm% K <sub>2</sub> HPO <sub>4</sub> Solution 25% (mg/mL)
Phantom Preparation ( $\sigma_p$ )	3	-	10	-
Image to Image ( $\sigma_i$ )	2	29	5	10
Scan to Scan ( $\sigma_r$ )	1	-	5	10
ROI Noise ( $\sigma_n$ )	4	41	3	10
Combined ( $\sigma_t$ )	5	50	13	17
Mean Value	349	451	558	912
CV (Unitless)	2%	11%	2%	2%

The data associated with the calculation of variation between images,  $\sigma_i$ , is summarized in Figure 6. The measured mean concentration across the central six images in the image stack associated with each syringe-phantom is plotted with the associated distance from the center of the image stack (taken as image 4). Each measurement was acquired with the ROI placed in the same location in each individual image stack. Overall, except for ethanol-water, the variation across the image stack was small (0.6-1%).

The ROI noise,  $\sigma_n$ , was found to vary with concentration (Figure 7). A clear increase in noise is seen in measurements made in syringe-phantoms containing Optiray 320 and K<sub>2</sub>HPO<sub>4</sub>, but no clear trend is visible in the other two sets of syringe-phantoms. The dominant source of variation differed between each set of syringe-phantoms.

## Image to Image Variation ( $\sigma_i$ )

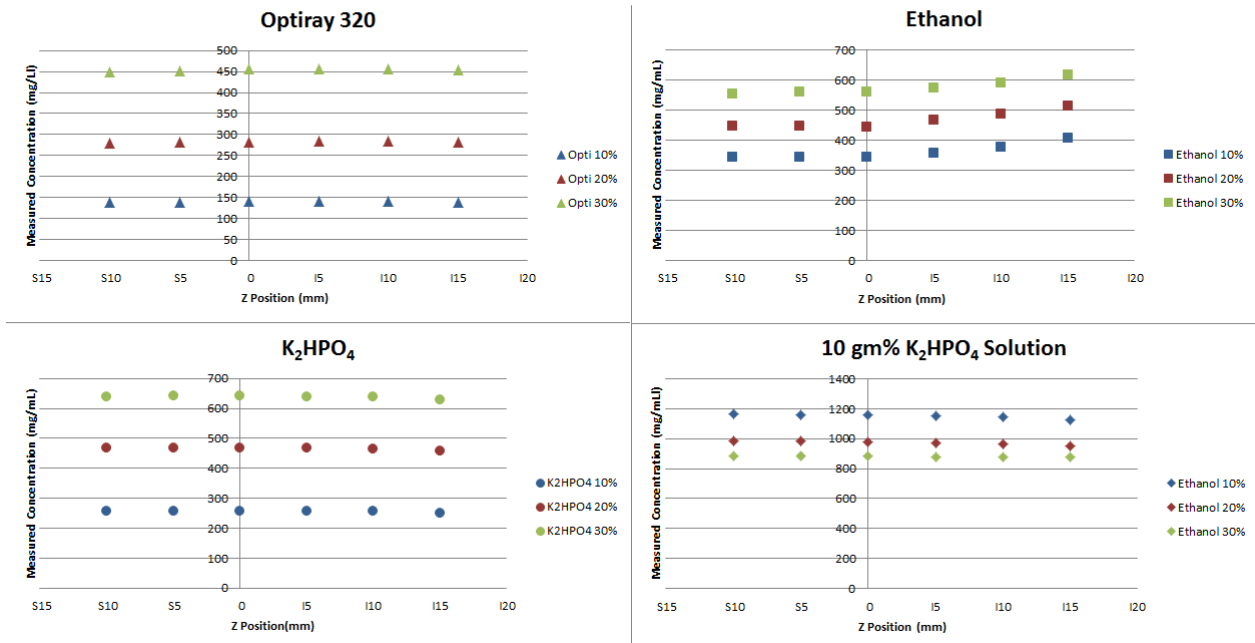
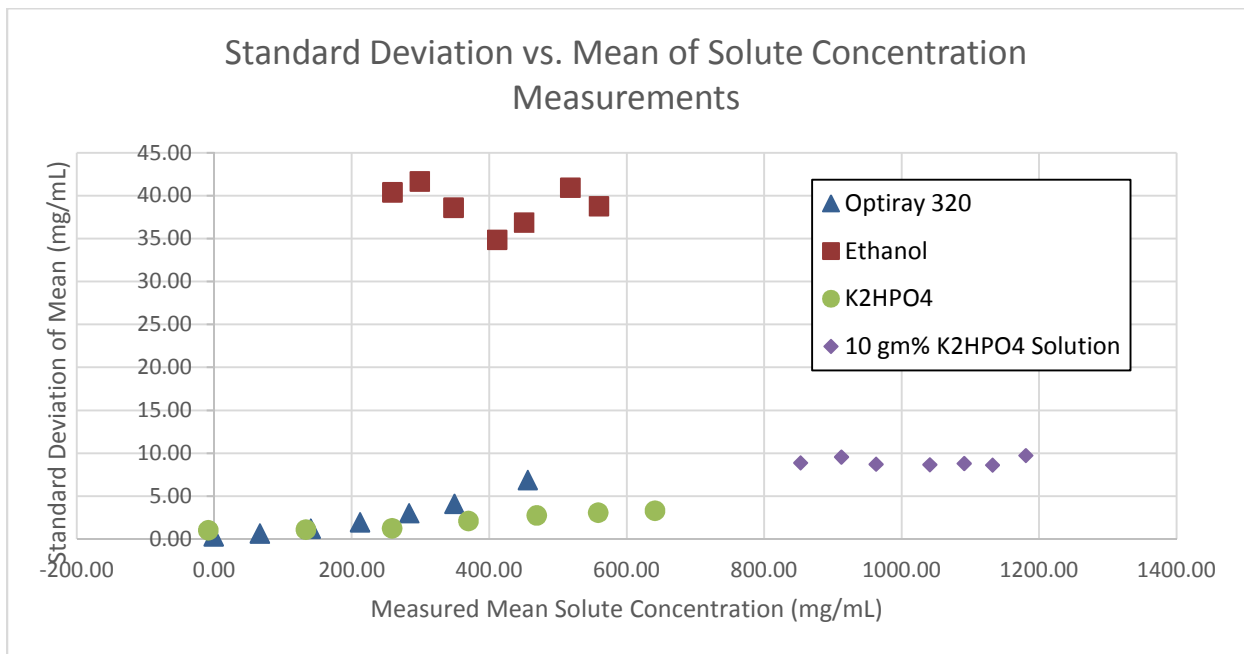


Figure 6: Mean concentration (mg/mL) measured in an ROI placed in the same position over each of the middle six images of the image stack acquired for three Optiray 320, ethanol, K<sub>2</sub>HPO<sub>4</sub>, and 10 gm% K<sub>2</sub>HPO<sub>4</sub> solution syringe-phantoms. The CV for Optiray was 0.6%, the CV for ethanol was 6%, the CV for K<sub>2</sub>HPO<sub>4</sub> was 0.9%, and the CV for 10 gm% K<sub>2</sub>HPO<sub>4</sub> solution was 1%.

Figure 7: The standard deviation of material density image solute concentration measurements of each syringe-phantom as a function of the measured mean solute concentration.



The material density image-derived solute concentrations of each constituent basis pair are plotted against the known concentration of each material in Figure 8. The data were positively correlated, and the squared Pearson's correlation coefficients of each regression were  $>0.986$  ( $p < 0.0001$ ) (Table 2). The significance tests (f-tests) and RMS errors are summarized in Table 3. The f-test found the fitted slope was significantly ( $p < 0.05$ ) different from 1 for all solutes and the intercept was significantly different from zero only for ethanol. The RMS errors for Optiray 320,  $K_2HPO_4$ , 10 gm%  $K_2HPO_4$  solution, and ethanol, were 9%, 10%, 12%, and 244% respectively. The especially large RMS error in ethanol stems from the large offset ( $\sim 252$  mg/mL) seen with ethanol-water basis pair measurements. While concentration measurements were significantly linearly correlated with the known concentration, the average RMS error was greater than 5% for all materials.

Table 2: Pearson's correlation coefficients (squared) for correlation, y-intercept, and slope of concentration measurements on images acquired using DECT in air with the GSI-6 protocol and the concentration of each solute or ethanol. Regressions with a y-intercept consistent with 0 within the 95% confidence intervals were re-plotted with the y-intercept set to 0.

Solute	R <sup>2</sup>	Slope	y-intercept (mg/mL)	Slope (intercept = 0)
Optiray 320	0.995	1.08 ± 0.08	-8 ± 20	1.06 ± 0.04
Ethanol	0.997	1.30 ± 0.09	252 ± 13	
K <sub>2</sub> HPO <sub>4</sub>	0.999	1.08 ± 0.04	0 ± 14	1.08 ± 0.02
10 gm% K <sub>2</sub> HPO <sub>4</sub> Solution	0.993	1.0 ± 0.1	83 ± 90	1.12 ± 0.01

## DECT Correlation/Accuracy

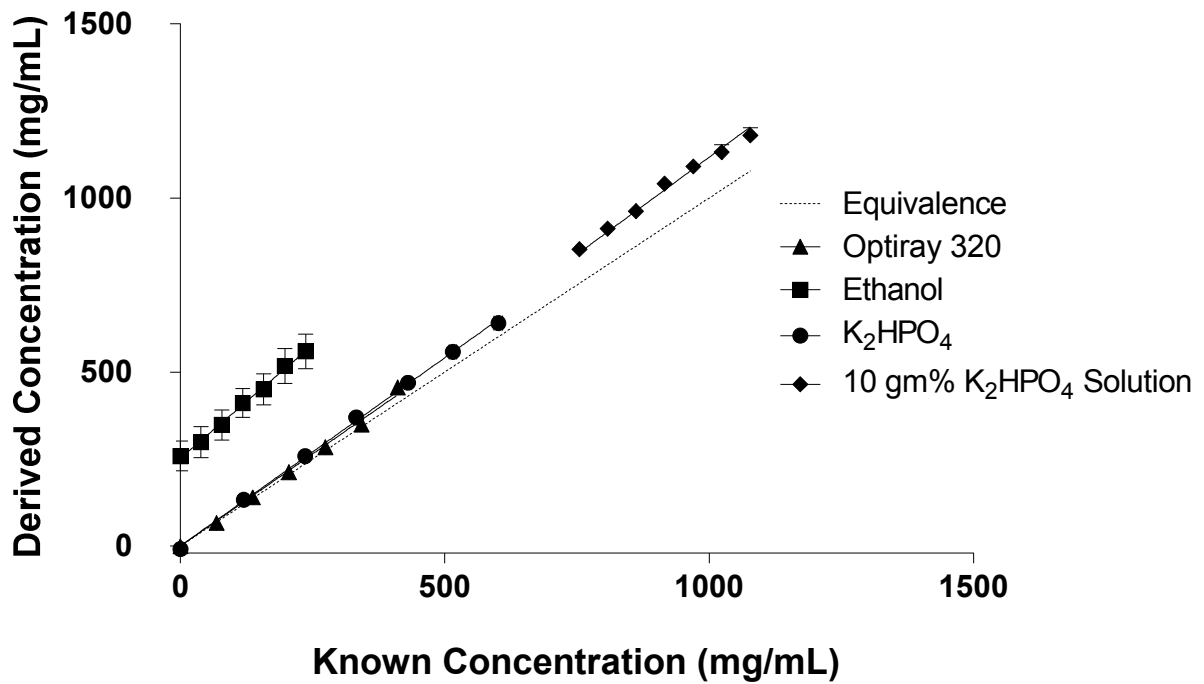


Figure 8: The material density image-derived concentration value of each solute is compared to the known concentration. A linear regression was applied for each solute. The line of equivalence is shown for reference. Error bars on the y-axis indicate total variation for each measurement and are too small to be visible on all but ethanol measurements. Error bars on the x-axis for K<sub>2</sub>HPO<sub>4</sub>, represent uncertainty in known concentration based on the observed volume but are too small to be visible in this plot.

Table 3: Statistics for material density image accuracy evaluation. The probability that each linear regression of the measured solute concentration vs. the known concentration has a slope of 1 and intercept of 0 is recorded, as well as the RMS error as an absolute and percentage of the average concentration for all syringe-phantoms of each solute. Significance in this experiment was defined as  $p < 0.05$ .

Solute	P value (Significant correlation)	P value (Slope = 1)	P value (0 Intercept)	RMS Error (mg/mL)	RMS %Error
Optiray 320	<0.0001	0.0157	0.3482	18	9%
Ethanol	<0.0001	0.0003	<0.0001	289	244%
K <sub>2</sub> HPO <sub>4</sub>	<0.0001	<0.0001	0.9582	31	10%
10 gm% K <sub>2</sub> HPO <sub>4</sub> Solution	<0.0001	<0.0001	0.065	109	12%

Bland-Altman analysis (110) is a statistical method for comparing the agreement between two measurement techniques. The mean difference between two measurements (bias) is evaluated and the “limits of agreement,” or the mean  $\pm 2 \times$  the standard deviation, are considered to be a range within which most differences would fall; variations within the limits of agreement must be clinically acceptable. The limits of agreement are calculated for a specific sample of the population of all measurements, so a 95% confidence interval may be calculated for these limits for entire the population by considering the degrees of freedom of the sample, the proper  $t$  value to give 95% confidence and the standard error  $s$  such that the interval is the bias  $\pm st$ .

To further investigate the accuracy of the material density image-derived concentration, we performed Bland-Altman analysis by comparing measured and expected concentrations for all syringe-phantoms, summarized in Figure 9 and Table 4. In particular, the 95% limits of the bias corresponding to K<sub>2</sub>HPO<sub>4</sub> (9-43 mg/mL) are large relative to the mean change in K<sub>2</sub>HPO<sub>4</sub> concentration equivalent that signifies osteoporosis in postmenopausal women in QCT (about



48 mg/mL) (111). The 95% confidence interval and limits of agreement are consistent with a bias of 0 mg/mL only for Optiray 320. With this analysis both sets of syringe-phantoms containing ethanol yielded especially large differences in measured concentrations from expected.

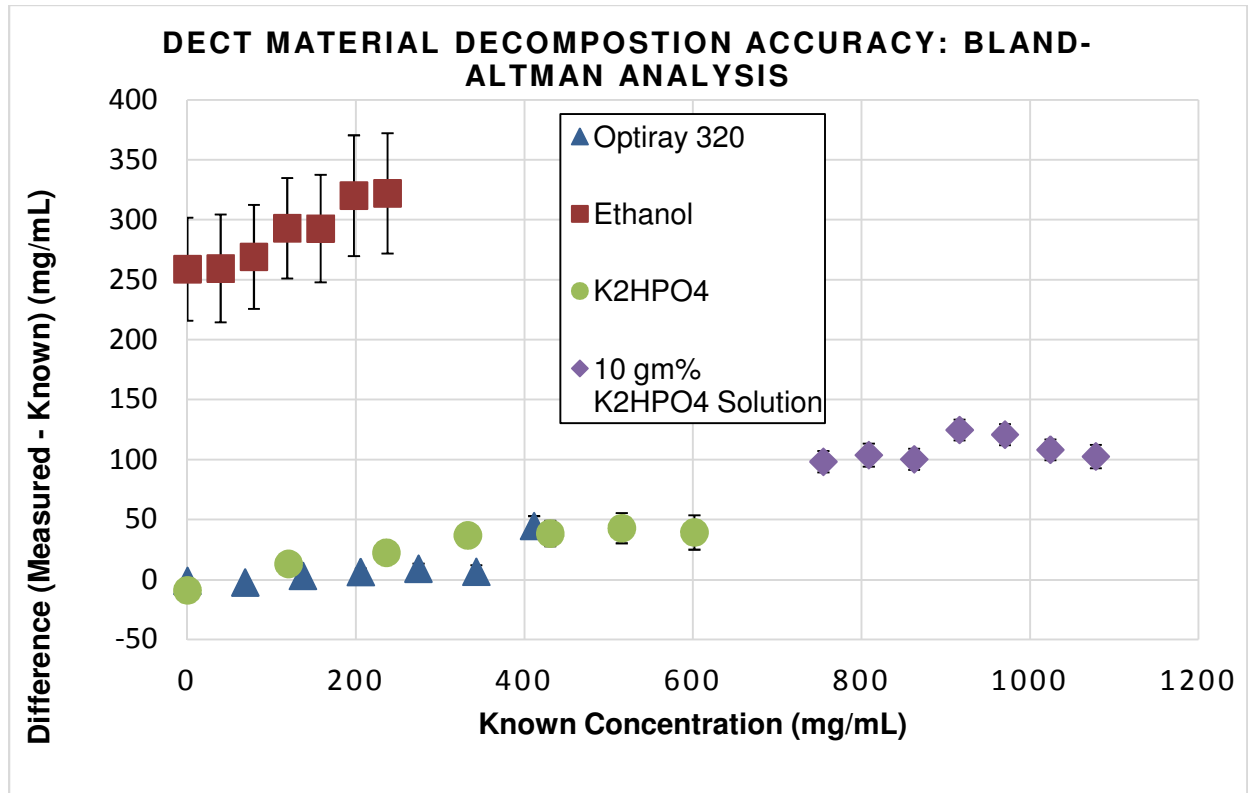


Figure 9: Bland-Altman analysis of material density image concentration measurements compared with known concentration. Error bars on the y-axis represent the total variation of the concentration measurements.

Table 4: Bland-Altman analysis of material density image-derived concentration measurements compared to the known concentration.

Solute	Average Difference (Derived-Known) (mg/mL)	Lower Limit of Agreement of Difference (mg/mL)	Upper Limit of Agreement of Difference (mg/mL)	Lower 95% Confidence Limit of Difference (mg/mL)	Upper 95% Confidence Limit of Difference (mg/mL)
Optiray 320	9	-23	41	-5	24
Ethanol	288	235	341	264	312
K <sub>2</sub> HPO <sub>4</sub>	26	-12	64	9	43
10 gm% K <sub>2</sub> HPO <sub>4</sub> Solution	109	88	129	99	118

### 3.1.1.2.2. SECT Linearity

The magnitude of each source of variation in an SECT measurement of a representative solute concentration is summarized as a CV in Table 5 and Table 6. As with DECT concentration measurements, the largest variation observed relative to the mean concentration was in HU measurements made in ethanol syringe-phantoms.

Table 5: Calculated sources of variation of a CT number measurement in air at 120 kVp for a 25% concentration. The mean value and CV of the total variation are also shown for reference. The total variation is the sum of the individual variabilities added in quadrature.

120 kVp Variation (Air)	Optiray 25% (HU)	Ethanol 25% (HU)	K <sub>2</sub> HPO <sub>4</sub> 25% (HU)	10 gm% K <sub>2</sub> HPO <sub>4</sub> Solution 25% (HU)
Phantom Preparation ( $\sigma_p$ )	11	-	10	-
Image to Image ( $\sigma_i$ )	12	34	10	7
Scan to Scan ( $\sigma_r$ )	9	-	2	1
ROI Noise ( $\sigma_n$ )	56	1	8	1
Total ( $\sigma_t$ )	59	34	16	7
Mean Value	2144	-28	813	122
CV (Unitless)	3%	-120%	2%	5%

Table 6: Calculated sources of variation of a CT number measurement in air at 80 kVp for a 20% concentration. The mean value and CV of the total variation are also shown for reference. The total variation is the sum of the individual variabilities added in quadrature. Calculation of the phantom preparation and repeat variation for Optiray 25% was not possible because the CT number reached its maximum value so 20% concentrations were evaluated.

80 kVp Variation (Air)	Optiray 20% (HU)	Ethanol 20% (HU)	K2HPO4 20% (HU)	10 gm% K2HPO4 Solution 20% (HU)
Phantom Preparation ( $\sigma_p$ )	-	-	12	-
Image to Image ( $\sigma_i$ )	23	14	13	7
Scan to Scan ( $\sigma_r$ )	-	-	3	1
ROI Noise ( $\sigma_n$ )	37	2	8	1
Total ( $\sigma_t$ )	43	14	20	7
Mean Value	2789	-25	930	188
CV (Unitless)	2%	-58%	2%	4%

Like DECT concentration, SECT HU was found to be positively correlated with the concentration of all solutes at 120 kVp ( $R^2 > 0.988$ ) (Figure 10, Table 7) and 80 kVp ( $R^2 > 0.913$ ) (Figure 11, Table 8). At 80 kVp, the HU of the Optiray 320 solutions reached the maximum value the software could record (3071), resulting in a weaker linear correlation.

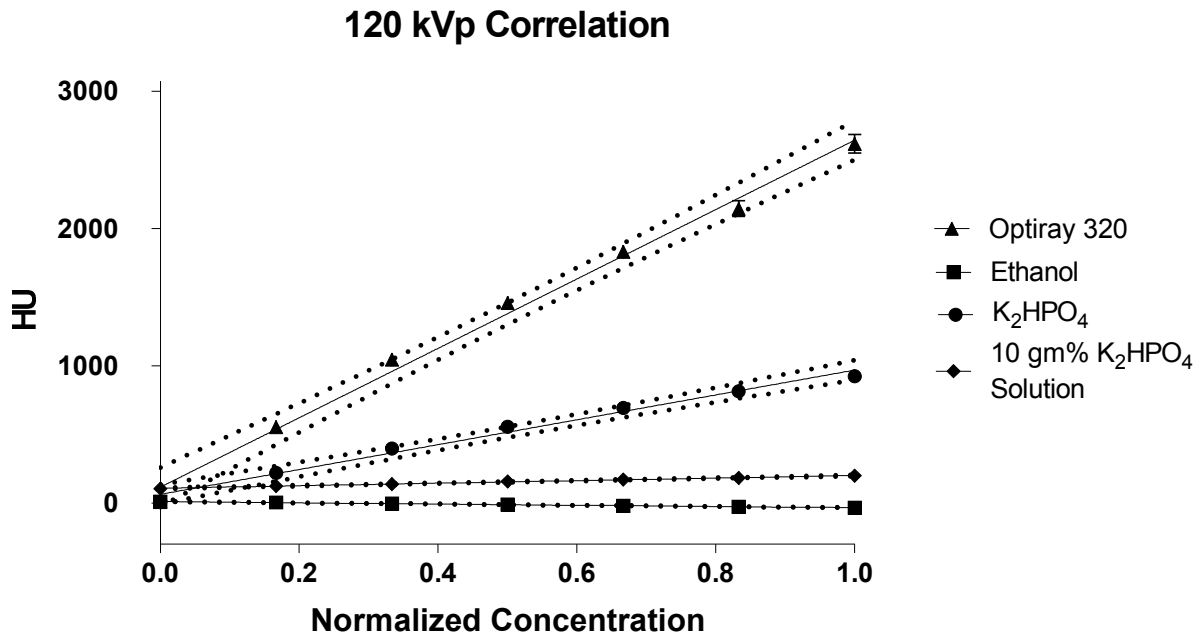


Figure 10: Correlation of HU measurements on images acquired using SECT at 120 kVp in air with the normalized known concentration. The known concentration was normalized according to the formula  $(value - minimum\ concentration)/(maximum\ concentration - minimum\ concentration)$ . Error bars indicate total variation for each measurement but are too small to be visible for most measurements. The dotted lines represent the 95% confidence limits for each regression fit to the data.

Table 7: Pearson's correlation coefficients (squared) for correlation of HU measurements on images acquired using SECT at 120 kVp and the known concentration of each solute.

Solute	R <sup>2</sup>
Optiray 320	0.988
Ethanol	0.997
K <sub>2</sub> HPO <sub>4</sub>	0.998
10 gm% K <sub>2</sub> HPO <sub>4</sub> Solution	0.995

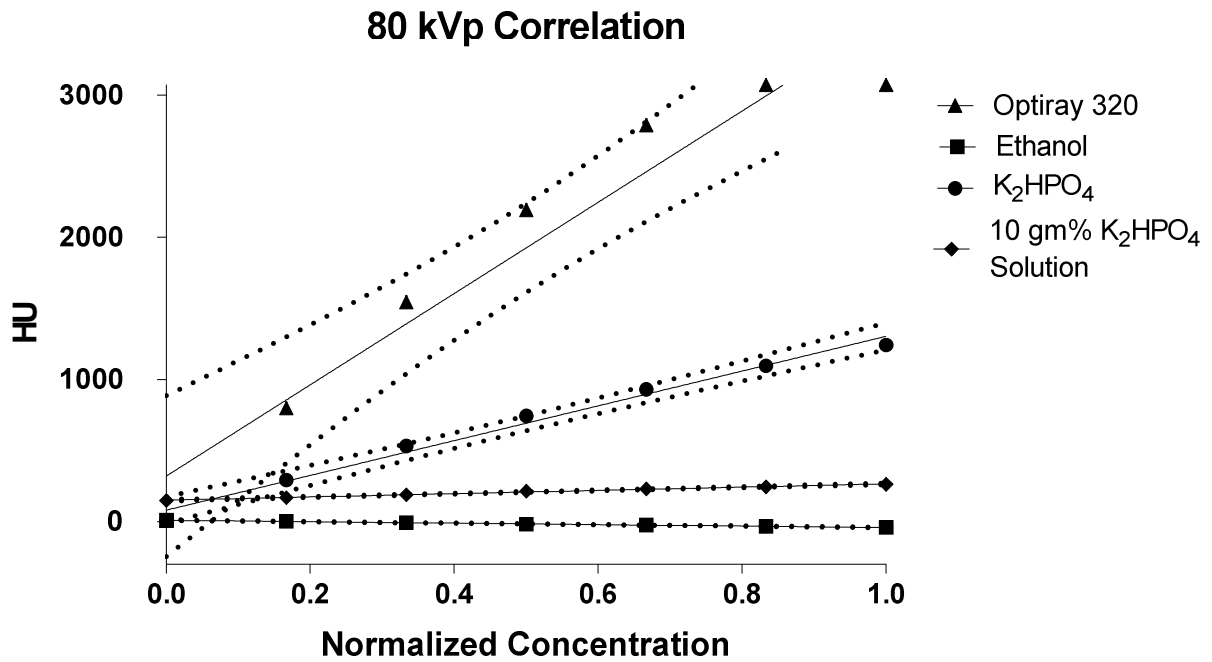


Figure 11: Correlation of HU measurements on images acquired using SECT at 80 kVp in air with the normalized known concentration. The known concentration was normalized according to the formula  $(value - minimum\ concentration) / (maximum\ concentration - minimum\ concentration)$ . Error bars indicate total variation for each measurement but are too small to be visible for most measurements. The dotted lines represent the 95% confidence limits for each regression fit to the data.

Table 8: Pearson's correlation coefficients (squared) for correlation of HU measurements on images acquired using SECT at 80 kVp and the known concentration of each solute.

Solute	R <sup>2</sup>
Optiray 320	0.913
Ethanol	0.996
K <sub>2</sub> HPO <sub>4</sub>	0.998
10 gm% K <sub>2</sub> HPO <sub>4</sub> Solution	0.994

### 3.1.1.2.3. DXA Linearity

The magnitude of each source of variation for a syringe-phantom measured with DXA aBMD is summarized for a representative solute concentration in Table 9. The variation in phantom preparation, though small, is a larger source of variation than the variation between scans.

*Table 9: Calculated sources of variation of a DXA aBMD measurement for a 25% concentration. The mean value and CV of the total variation are also shown for reference. The total variation is the sum of the individual variabilities added in quadrature.*

<b>DXA Variation</b>	<b>Optiray 25% (aBMD)</b>	<b>Ethanol 25% (aBMD)</b>	<b>K<sub>2</sub>HPO<sub>4</sub> 25% (aBMD)</b>	<b>10 gm% K<sub>2</sub>HPO<sub>4</sub> Solution 25% (aBMD)</b>
Phantom Preparation ( $\sigma_p$ )	0.03	-	0.02	-
Scan to Scan ( $\sigma_r$ )	0.01	-	0.01	0.001
Total ( $\sigma_t$ )	0.03	-	0.02	0.001
Mean Value	5.41	0.064	1.26	0.272
CV	1%	-	2%	0%

The aBMD measured by DXA was also found to be correlated with solute concentration for all materials ( $R^2 > 0.880$ ) (Figure 12, Table 10). The correlation was weakest for ethanol.

## BMD Correlation

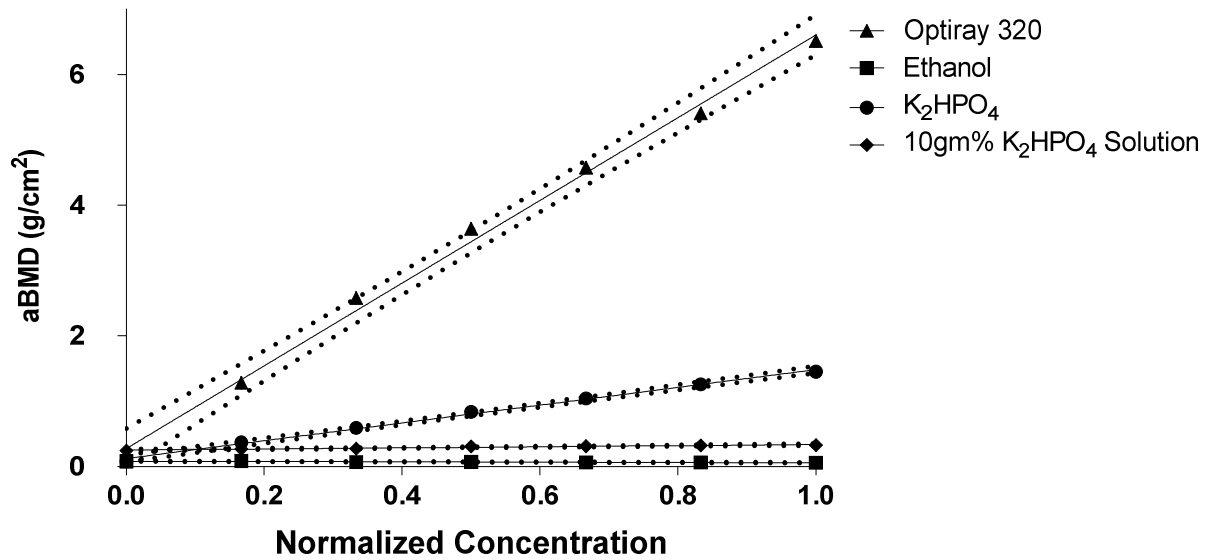


Figure 12: Correlation of aBMD measured by DXA with the known normalized concentration of each solute. The known concentration was normalized according to the formula  $(\text{value} - \text{minimum concentration}) / (\text{maximum concentration} - \text{minimum concentration})$ . Error bars indicate total variation for each measurement but are too small to be visible for most measurements. The dotted lines represent the 95% confidence limits for each regression fit to the data.

Table 10: Pearson's correlation coefficients (squared) for correlation of aBMD measured by DXA with the known concentration of each solute.

Solute	R <sup>2</sup>
Optiray 320	0.990
Ethanol	0.851
K <sub>2</sub> HPO <sub>4</sub>	0.999
10 gm% K <sub>2</sub> HPO <sub>4</sub> Solution	0.933

### 3.1.1.3. Discussion

All measurement methods had less variation in the Optiray 320 phantom preparation than in  $K_2HPO_4$  phantom preparation. This result is not surprising when considering the different preparation methods (Section 3.1.1.1). There was uncertainty introduced in the  $K_2HPO_4$ -water syringe-phantoms in the weighing of the  $K_2HPO_4$  and additional uncertainty introduced during the pipetting of the water and the transfer of the  $K_2HPO_4$  powder to the water. In contrast, uncertainty was introduced in the Optiray 320 syringe-phantom preparation only during the pipetting of the Optiray 320 and pipetting of the water; that is, there were fewer sources of uncertainty.

The material density image-derived concentration measurements were well correlated and increased linearly with the known solute concentration (Figure 8). SECT and DXA measurements also showed a strong linear correlation. While material density image measurements of syringe-phantoms containing Optiray 320 and  $K_2HPO_4$  coarsely followed the line of equivalence (intercept consistent with zero and slope only marginally different than unity), those for syringe-phantoms containing ethanol were substantially less accurate. Measurements of ethanol concentration in ethanol-water syringe-phantoms, though linear, had a very large RMS error (289 mg/mL) (Table 3) and offset; indeed, a large concentration of ethanol ( $260 \pm 40$  mg/mL) was measured even in the 0% concentration syringe-phantom, where only distilled water was present. The ethanol-water syringe-phantoms, as well as the 10 gm%  $K_2HPO_4$  solution syringe-phantoms, also had relatively large biases (Table 4). Distinguishing between ethanol and water is evidently problematic for the material density decomposition feature of the GSI Viewer software. This may be explained by the very similar mass attenuation coefficients of water and ethanol within the energy range of rsDECT x-rays (Figure 13). The effective energy of the 80 and 140 kVp beams used in the DECT acquisitions with the medium body filter are roughly 40 and 50 keV. The mass attenuation coefficients of water and ethanol are  $0.268 \text{ g/cm}^2$  and  $0.243 \text{ g/cm}^2$  at 40 keV and  $0.227 \text{ g/cm}^2$  and  $0.216$



g/cm<sup>2</sup> at 50 keV respectively. In comparison, the mass attenuation coefficient of K<sub>2</sub>HPO<sub>4</sub> is 0.933 g/cm<sup>2</sup> at 40 keV and 0.557 at 50 keV g/cm<sup>2</sup>.

Due to the poor results with the ethanol-water syringe-phantoms and basis pair, these data were excluded from further investigation in this paper.

The large average RMS error for all solutes, even those in syringe-phantoms not containing ethanol (Table 3), reduces confidence in absolute DECT concentration measurements. The large RMS error for two-material phantoms of known suggests that measurements of bone material, where the exact composition of trabecular bone varies from patient to patient, would almost certainly see errors in accuracy greater than 5%.

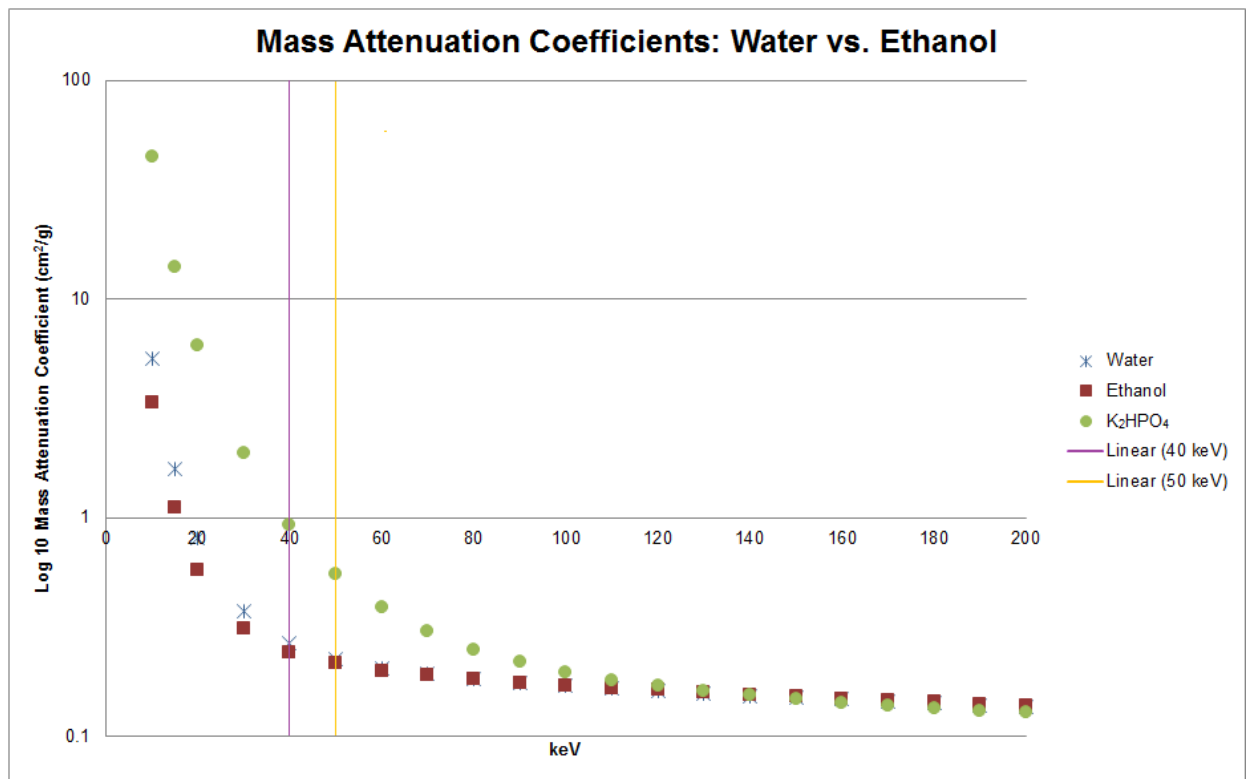


Figure 13: Mass attenuation coefficient of water, ethanol, and K<sub>2</sub>HPO<sub>4</sub> from 10-200 keV, with the ordinate on a base 10 logarithmic scale. Data taken from NIST XCOM database (109). The effective energies of the two beams used in DECT mode (roughly 40 and 50 keV) are indicated.

### 3.1.2. Differing Scan Parameters

#### 3.1.2.1. Materials and Methods

To investigate the effect of various scanning conditions on the accuracy of material density image concentration measurements, further scans of the 28 syringe-phantoms were obtained under a variety of conditions: 1) using different a different GSI protocol, 2) in different scattering conditions, and 3) at a location away from isocenter.

Depending on patient size, a different GSI protocol may be indicated for a hypothetical DEQCT BMD evaluation. To assess the effect of the GSI protocol, we scanned each syringe-phantom with the GSI-5 protocol, which differs from the GSI-6 protocol in the bowtie filter used and estimated  $CTDI_{vol}$  (Table 11).

Table 11: Comparison of GSI protocols assessed in Section 3.1.2.

Protocol	Type	Bowtie Filter Size	Tube Rotation Time	Beam width	Estimated $CTDI_{vol}$
GSI-6	Body	Medium	1 s	40 mm (Axial)	33.43 mGy
GSI-5	Body	Large	1 s	40 mm (Axial)	32.01 mGy

Differences in patient morphology and scan setup may translate into different placement of the lumbar spine relative to isocenter of the DECT scanner in a clinical examination. Likewise, all clinical QCT measurements of vBMD are made not in air but in scattering conditions created by the soft tissue of the patient. To assess the effect of patient positioning, each syringe-phantom was scanned in air with the central bore of the electron density body phantom set 10.5 cm above isocenter (Figure 14) and compared the measurements to those made with the syringe-phantom set at isocenter. To assess the effects of homogenous scattering conditions, the portion of the syringe-phantom containing the two-material solution

was placed within the central bore of the electron density body phantom while the surrounding bores were filled with either water-filled 60 mL syringes or water-equivalent inserts (Figures 16-17). To assess the effects of heterogeneous scattering conditions, the surrounding bores were filled with water-equivalent or various tissue-equivalent inserts included with the phantom ranging from lung equivalent (inspiration) to cortical bone equivalent (about -810 to 910 HU at 120 kVp) (Figure 17).

In a clinical environment, the weight of different patients varies greatly or the same patient may vary in weight between exams. To assess the effect of homogenous scattering conditions in a smaller-sized scattering environment, the head insert (7.1 in. (18 cm) diameter) was removed from the surrounding body (13 in. x 2 in. x 10.6 in.) of the electron density phantom and the associated bores were filled with either syringes containing water or water-equivalent inserts (Figure 18).

All scattering-condition measurements were made using the GSI-6 protocol. For comparison, sequential axial 120 kVp/150 mA and 80 kVp/200 mA SECT scans with a 1s tube rotation time and using the medium body filter were acquired immediately following each DECT scan in the various scattering conditions. It was hypothesized that measurements made in scattering conditions would have different variabilities than those made in air so a reassessment of all sources of variation was performed of the syringe-phantoms in homogenous scattering conditions in the body phantom using the same methods as previously outlined in Section 3.1.1.1 (the same syringe-phantoms were used to assess phantom preparation variation). The variation for measurements made in all scattering conditions was estimated with the new total variabilities  $\sigma_t$ .

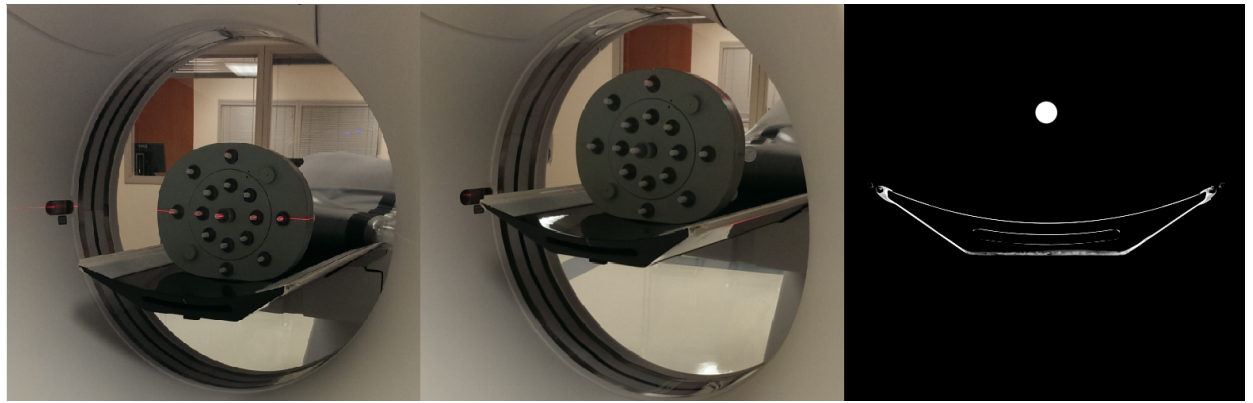


Figure 14: On and off-isocenter measurements with DECT. Right: The syringe-phantom protrudes in air from the central bore of the electron density body phantom on and Center: set 10.5 cm above isocenter. Right: 120 kVp image of a  $K_2HPO_4$  syringe-phantom in air 10.5 cm above isocenter.

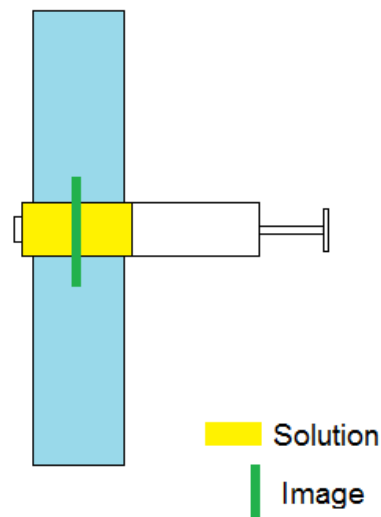


Figure 15: Configuration of materials used for DECT and SECT measurements in scattering conditions. The syringe-phantom was inserted in the central bore of the electron density body phantom with the solution enclosed within the body of the phantom. Eight images that spanned the solution volume were acquired, and a measurement was made on the central image (4 or 5) as shown.

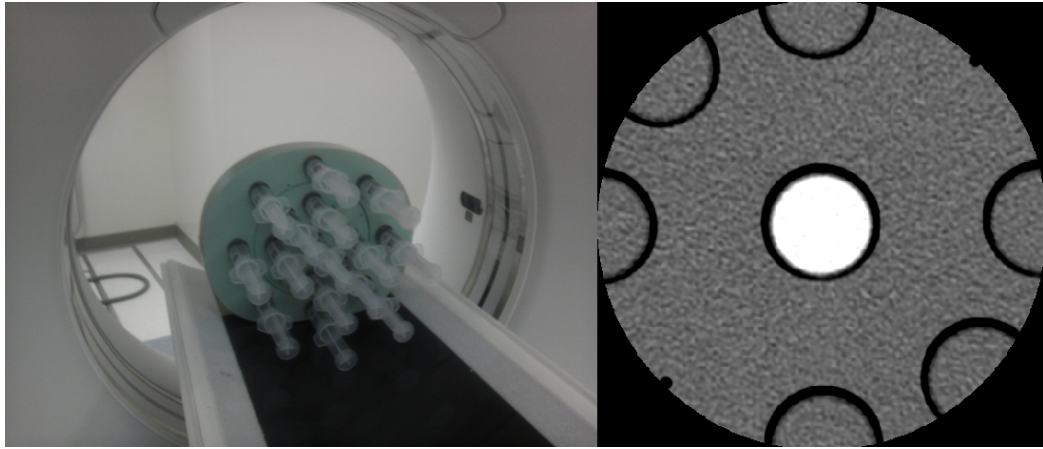


Figure 16: DECT and SECT measurement in homogenous scattering conditions. Left: Water-equivalent inserts or 60 mL syringes filled with distilled water were placed within all but the central bore of the water-equivalent electron density phantom body to perform measurements of each two-material syringe-phantom. Right: 120 kVp image of a  $K_2HPO_4$  syringe-phantom in homogenous scattering conditions. The two water-equivalent inserts can be seen at the approximate one o'clock and seven o'clock positions.

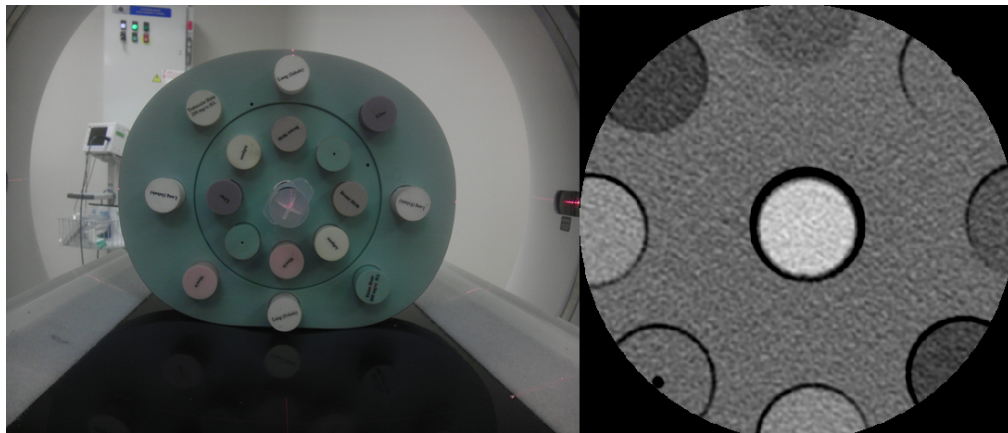
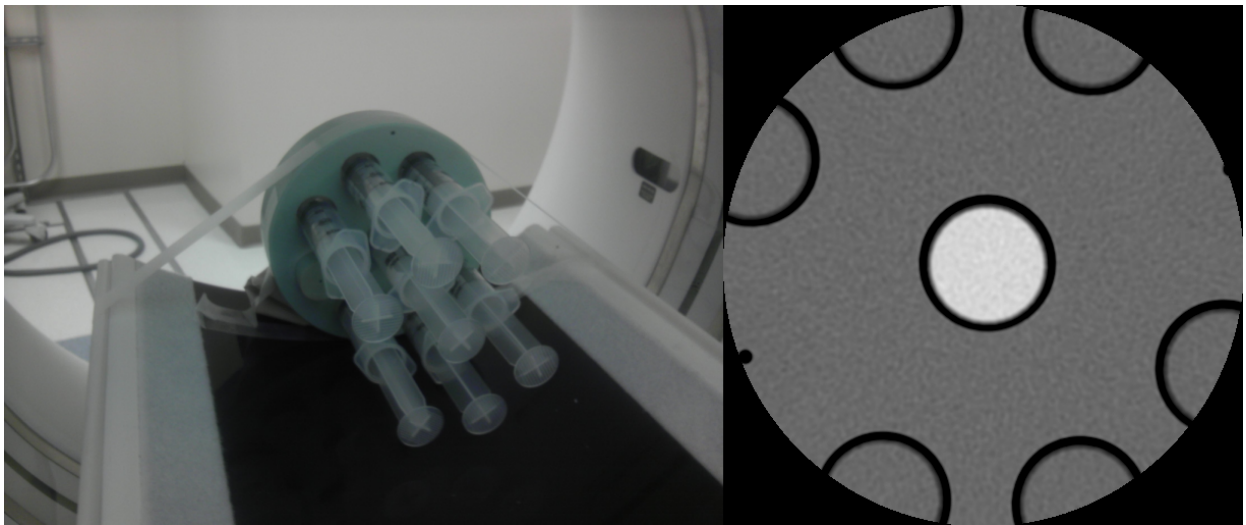


Figure 17: DECT and SECT measurements in heterogeneous scattering conditions. Left: Electron density body phantom with tissue-equivalent inserts placed within all but the central bore of the water-equivalent phantom body. The two-material solution is placed within the body of the phantom in the central bore to perform measurements of each syringe-phantom. Right: 120 kVp image of a  $K_2HPO_4$  syringe-phantom in heterogeneous scattering conditions.

*Figure 18: DECT and SECT measurements in smaller-sized homogenous scattering conditions. Left: The outer body portion of the electron density phantom was removed and water-equivalent inserts or 60 mL syringes filled with distilled water were placed within all but the central bore of the water-equivalent electron density phantom to perform measurements of each two-material syringe-phantom. Right: 120 kVp image of a  $K_2HPO_4$  syringe-phantom in the head portion of the electron density phantom. Due to the display field of view used, the image here looks similar to the image for homogenous scattering conditions in the body phantom.*



The derived solute concentration or HU for each set of measurements was compared to the original concentration or HU measurement in air obtained in Section 3.1.1.2. A linear regression was applied to determine the slope and y-intercept with 95% confidence intervals of the correlation. Regressions with a y-intercept consistent with 0 within 95% confidence limits were re-fit with a y intercept equal to 0. The Pearson's correlation coefficient was also derived for each fit.

### **3.1.2.2. Results**

The magnitude of each form of variation in DECT and SECT for each set of syringe-phantoms in homogenous scattering conditions is summarized for a representative

concentration in Table 12 and Tables 13-14 respectively. In general, all sources of variation were greater in scatter.

*Table 12: Calculated sources of variation of a solute concentration measurement in scattering conditions by DECT for a 25% concentration. The mean value and CV of the total variation are also shown for reference. The total variation is the sum of the individual variabilities added in quadrature.*

<b>DECT Variation (Scatter)</b>	<b>Optiray 25% (mg/mL)</b>	<b>Ethanol 25% (mg/mL)</b>	<b>K<sub>2</sub>HPO<sub>4</sub> 25% (mg/mL)</b>	<b>10 gm% K<sub>2</sub>HPO<sub>4</sub> Solution 25% (mg/mL)</b>
Phantom Preparation ( $\sigma_p$ )	1	-	16	-
Image to Image ( $\sigma_i$ )	3	39	6	12
Scan to Scan ( $\sigma_r$ )	3	-	21	23
ROI Noise ( $\sigma_n$ )	5	314	13	97
Total ( $\sigma_t$ )	8	316	30	100
Mean Value	242	377	378	687
CV	3%	84%	8%	15%

*Table 13: Calculated sources of variation of a CT number measurement in scattering conditions at 120 kVp for a 25% concentration. The mean value and CV of the total variation are also shown for reference. The total variation is the sum of the individual variabilities added in quadrature.*

<b>120 kVp Variation (Scatter)</b>	<b>Optiray 25% (HU)</b>	<b>Ethanol 25% (HU)</b>	<b>K<sub>2</sub>HPO<sub>4</sub> 25% (HU)</b>	<b>10 gm% K<sub>2</sub>HPO<sub>4</sub> Solution 25% (HU)</b>
Phantom Preparation ( $\sigma_p$ )	8	-	12	-
Image to Image ( $\sigma_i$ )	14	2	6	2
Scan to Scan ( $\sigma_r$ )	6	-	10	1
ROI Noise ( $\sigma_n$ )	30	17	18	16
Total ( $\sigma_t$ )	34	17	25	16
Mean Value	1491	-33	577	69
CV	2%	-52%	4%	24%

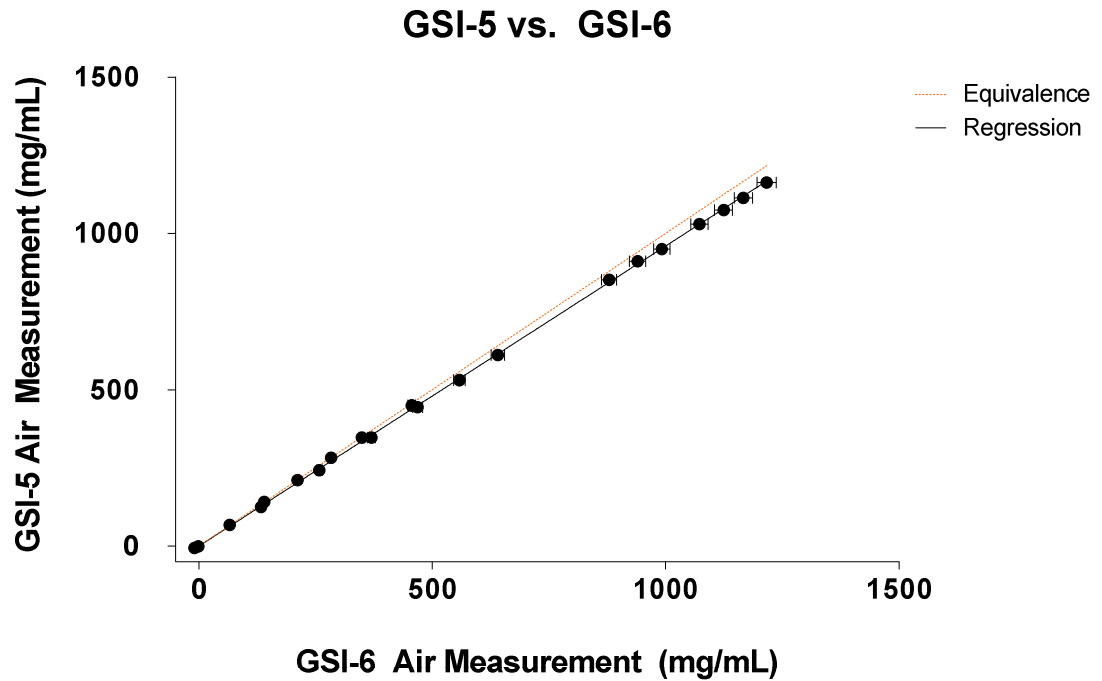


Table 14: Calculated sources of variation of a CT number measurement in scattering conditions at 80 kVp for a 25% concentration. The mean value and CV of the total variation are also shown for reference. The total variation is the sum of the individual variabilities added in quadrature.

80 kVp Variation (Scatter)	Optiray 20% (HU)	Ethanol 20% (HU)	K <sub>2</sub> HPO <sub>4</sub> 20% (HU)	10 gm% K <sub>2</sub> HPO <sub>4</sub> Solution 20% (HU)
Phantom Preparation ( $\sigma_p$ )	8	-	23	-
Image to Image ( $\sigma_i$ )	17	3	6	3
Scan to Scan ( $\sigma_r$ )	9	-	13	1
ROI Noise ( $\sigma_n$ )	38	24	30	24
Total ( $\sigma_t$ )	43	25	40	24
Mean Value	1965	-33	643	111
CV	2%	-74%	6%	21%

Material density image concentration measurements with the two different scan protocols were correlated, ( $R^2 > 0.999$ ) and when fit to a straight line yielded an offset consistent with 0 and a slope near unity ( $0.960 \pm 0.005$ ) (Figure 19, Table 15). Similarly, material density image concentration measurements with the phantom placed on and off isocenter were correlated ( $R^2 > 0.999$ ) and when fit to a straight line also yielded an offset consistent with 0 and a slope near unity ( $0.954 \pm 0.004$ ) (Figure 20). Both scenarios yielded statistically significant differences from identity, but the effect was relatively small (< 5% discrepancy).





*Figure 19: Comparison of material density image concentration measurements performed using the GSI-5 and GSI-6 protocols. Error bars on the x and y axis indicate total variation for measurements made using GSI-6 and GSI-5 protocols respectively and aren't visible for most points.*

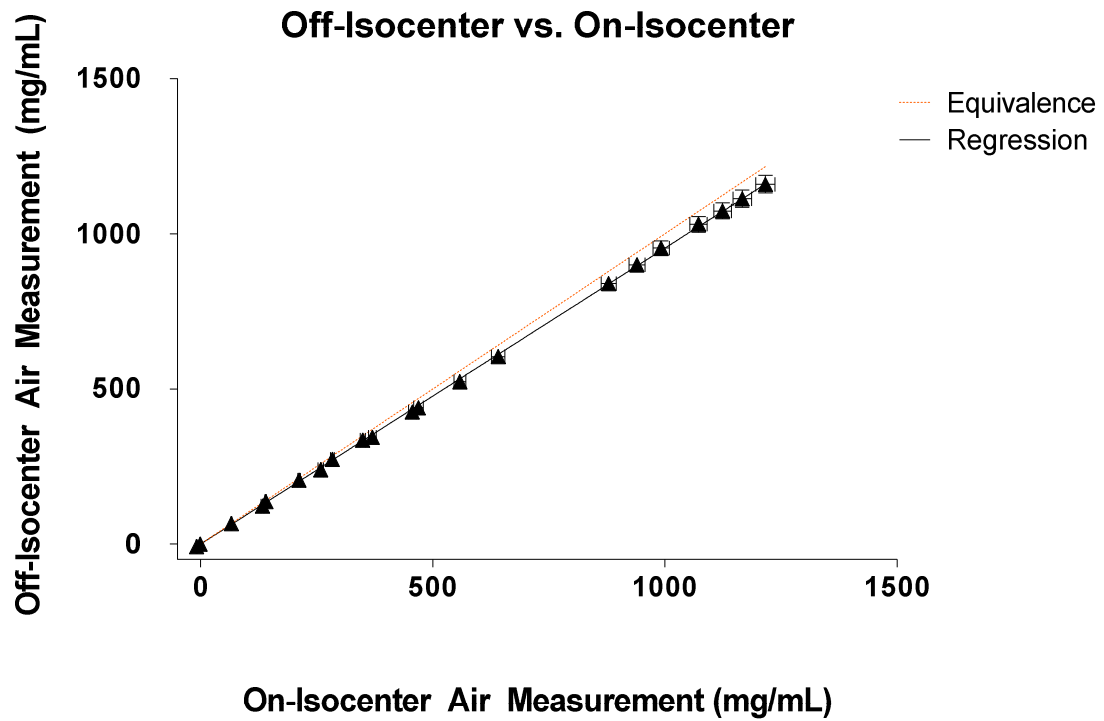


*Figure 20: Comparison of material density image concentration measurements performed at isocenter and 10.5 cm above isocenter. Error bars on the x and y axis indicate total variation for measurements made on and displaced from isocenter respectively and aren't visible for most points. All measurements were made using the GSI-6 protocol.*

*Table 15: Slope and y-intercept with 95% confidence intervals and squared Pearson's correlation coefficient for the linear regression comparing material density image concentration measurements acquired using GSI-5/6 protocols and on/10.5 cm above isocenter. The y-intercept with 95% confidence intervals was equivalent to 0 in the original regression in both cases, so the data were re-fit with a regression set to intercept the y-axis at  $y = 0$  mg/mL. The probability of the slope of this regression being equivalent to unity was evaluated with an f-test. Significance in this experiment was defined as  $p < 0.05$ .*

<b>Regression</b>	<b>Slope</b>	<b>R<sup>2</sup></b>	<b>y-Intercept (mg/mL)</b>	<b>Slope (Intercept = 0)</b>	<b>p (slope = 1)</b>
GSI-5 vs. GSI-6	$0.955 \pm 0.008$	>0.999	$4 \pm 5$	$0.960 \pm 0.005$	<0.0001
Off vs. On-Isocenter	$0.957 \pm 0.006$	>0.999	$-2 \pm 4$	$0.954 \pm 0.004$	<0.0001

Scattering conditions severely (by ~26%) reduced the material density image-derived concentration compared to measurements made in air (Figure 21, Table 16). The effect of heterogeneous scattering conditions was not significantly different from homogenous scattering conditions (< 1% difference). The effect of scatter in the head phantom was far less pronounced, but still significant (~8% reduction from in-air measurements). In comparison, the presence of scattering material also decreased the CT number relative to air at 120 (slope =  $0.70 \pm 0.01$ ) and 80 kVp (slope =  $0.75 \pm 0.04$ ) (Figure 22, Table 17). Again the difference between measurements made in heterogeneous and homogenous scattering conditions was not significant. Measurements made in the head insert did not differ as much as in the body phantom when compared to air (slope =  $0.834 \pm 0.007$  at 120 and  $0.93 \pm 0.04$  at 80 kVp).

Table 16: Slope and y-intercept with 95% confidence intervals and squared Pearson's correlation coefficient for the linear regression comparing material density image concentration measurements made in air and in various scattering conditions. The y-intercept with 95% confidence intervals was equivalent to 0 in the original regression in all cases, so the data were re-fit with a regression set to intercept the y-axis at y = 0. Significance in this experiment was defined as  $p < 0.05$ . Note: Hom. = homogenous, Het. = heterogeneous.

DECT Regression	Slope	R <sup>2</sup>	y-Intercept (mg/mL)	Slope (Intercept = 0)	p (slope = 1)
Hom. Scatter vs. Air	$0.75 \pm 0.03$	0.994	$-14 \pm 17$	$0.74 \pm 0.02$	$< 0.0001$
Het. Scatter vs. Air	$0.76 \pm 0.02$	0.996	$-10 \pm 14$	$0.75 \pm 0.01$	$< 0.0001$
Small Hom. Scatter vs. Air	$0.92 \pm 0.02$	0.998	$-7 \pm 13$	$0.91 \pm 0.01$	$< 0.0001$

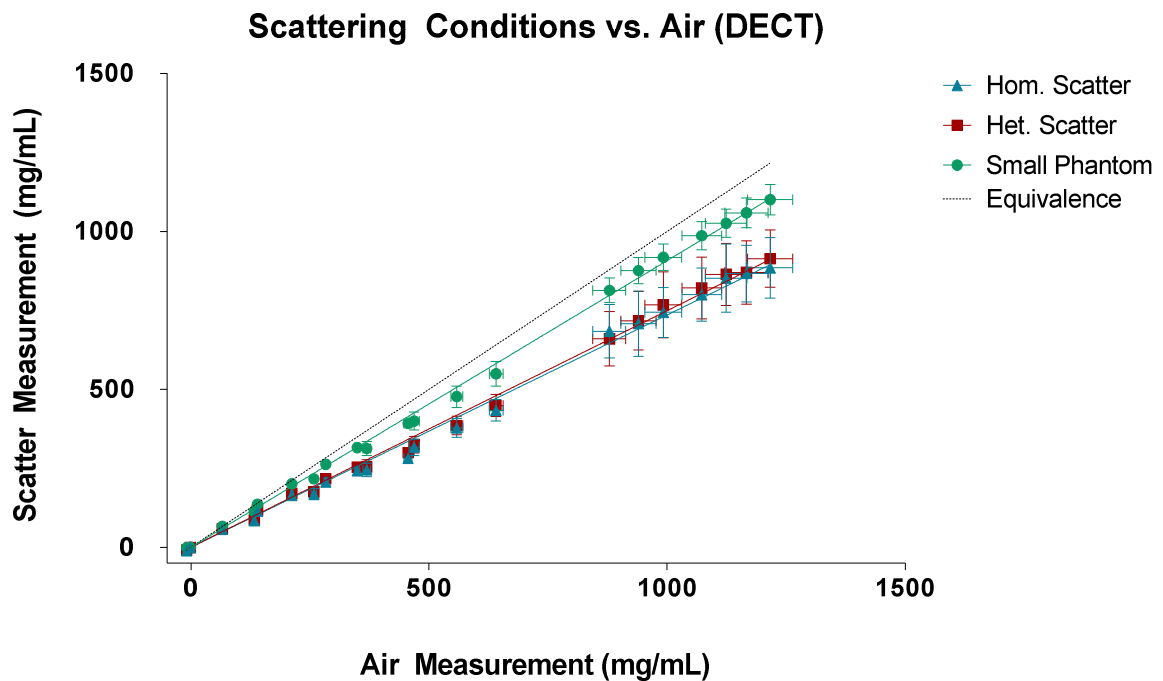


Figure 21: Comparison of material density image concentration measurements acquired in air and in different scattering conditions. Error bars on the x and y axis indicate total variation for measurements made in air and in scattering conditions respectively. The line of equivalence is shown for reference.

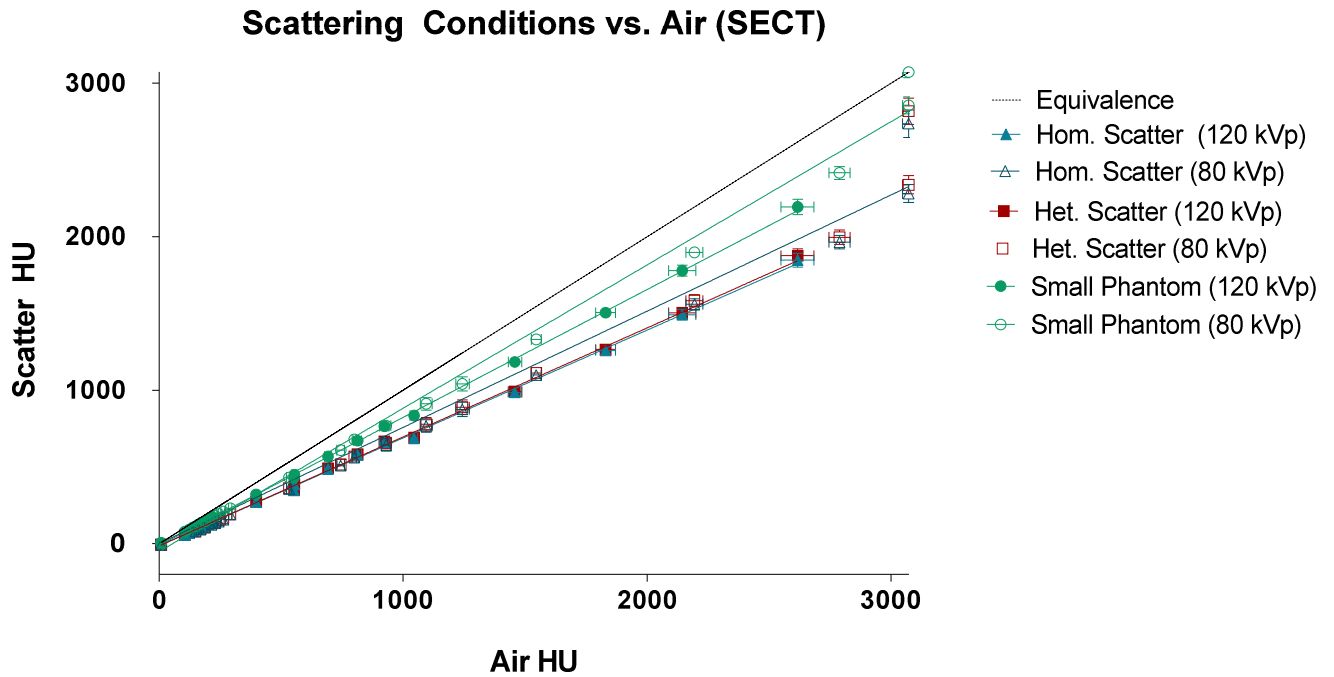


Figure 22: Comparison of SECT HU measurements acquired in air and in different scattering conditions at 120 and 80 kVp. Error bars on the x and y axis indicate total variation for measurements made in air and in scattering conditions respectively. The line of equivalence is shown for reference.

*Table 17: Slope and y-intercept with 95% confidence intervals and the squared Pearson's correlation coefficient for the linear regression comparing SECT concentration measurements made in air and in various scattering conditions at 120 and 80 kVp. The y-intercept with 95% confidence intervals was equivalent to 0 in the original regression in homogenous and heterogeneous scattering conditions in the body phantom at 80 kVp, so the data were re-fit with a regression set to intercept the y-axis at y = 0 HU. Note: Hom. = homogenous, Het. = heterogeneous.*

<b>SECT Regression</b>	<b>Slope</b>	<b>R<sup>2</sup></b>	<b>y-Intercept (HU)</b>	<b>Slope (Intercept = 0)</b>	<b>p (slope = 1)</b>
Hom. Scatter vs. Air (120 kVp)	0.70 ± 0.01	0.999	-14 ± 10		<0.0001
Hom. Scatter vs. Air (80 kVp)	0.79 ± 0.05	0.984	-60 ± 70	0.75 ± 0.04	<0.0001
Het. Scatter vs. Air (120 kVp)	0.71 ± 0.01	0.999	-15 ± 11		<0.0001
Het. Scatter vs. Air (80 kVp)	0.77 ± 0.04	0.982	-60 ± 60	0.77 ± 0.04	<0.0001
Small Hom. Scatter vs. Air (120 kVp)	0.834 ± 0.007	>0.999	-11 ± 7		<0.0001
Small Hom. Scatter vs. Air (80 kVp)	0.93 ± 0.04	0.994	-50 ± 49		0.0012

For the remainder of this paper, when assessing the effects of scatter on DECT and SECT measurements, we explored only homogenous scattering conditions in the body phantom.

Figures 24-28 illustrate the magnitude of each source of variation for each measurement method as an average CV of the mean measurement across all concentrations. Figure 23 illustrates the magnitude of the total variation for each measurement method. The magnitude of every type of variation is highest in DECT and SECT measurements in scattering conditions and for ethanol.

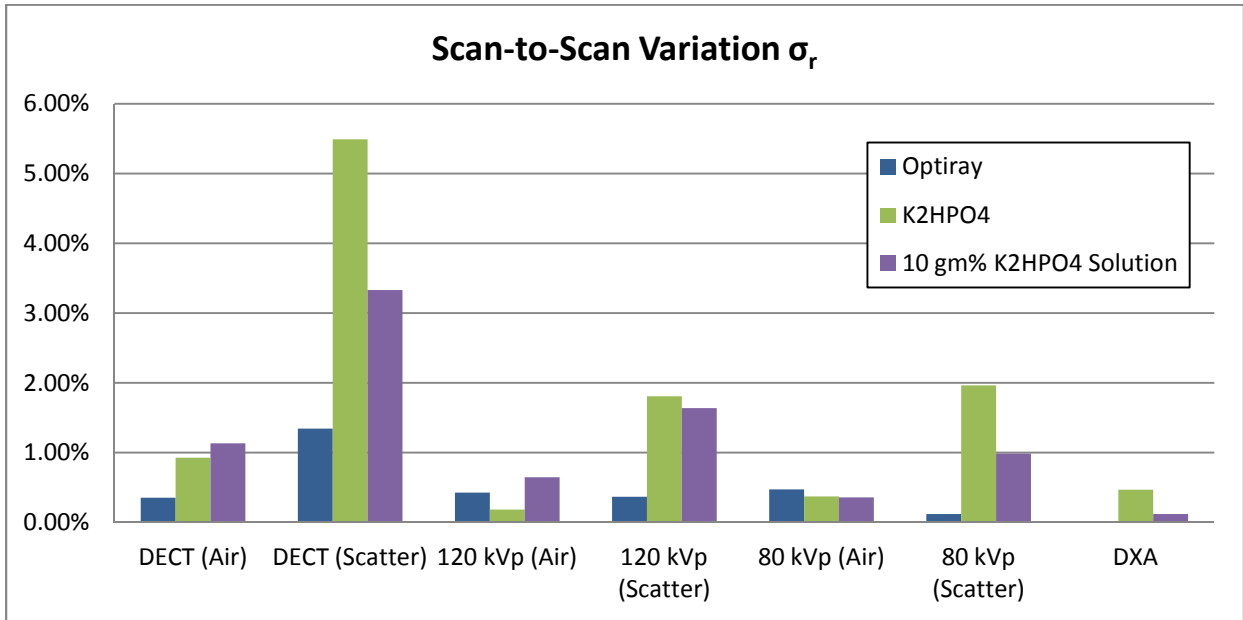


Figure 23: Variation between scans as an average CV of the mean measurement assessed in DECT, SECT, and DXA for Optiray 320, K<sub>2</sub>HPO<sub>4</sub>, and 10 gm% K<sub>2</sub>HPO<sub>4</sub> solution syringe-phantoms.

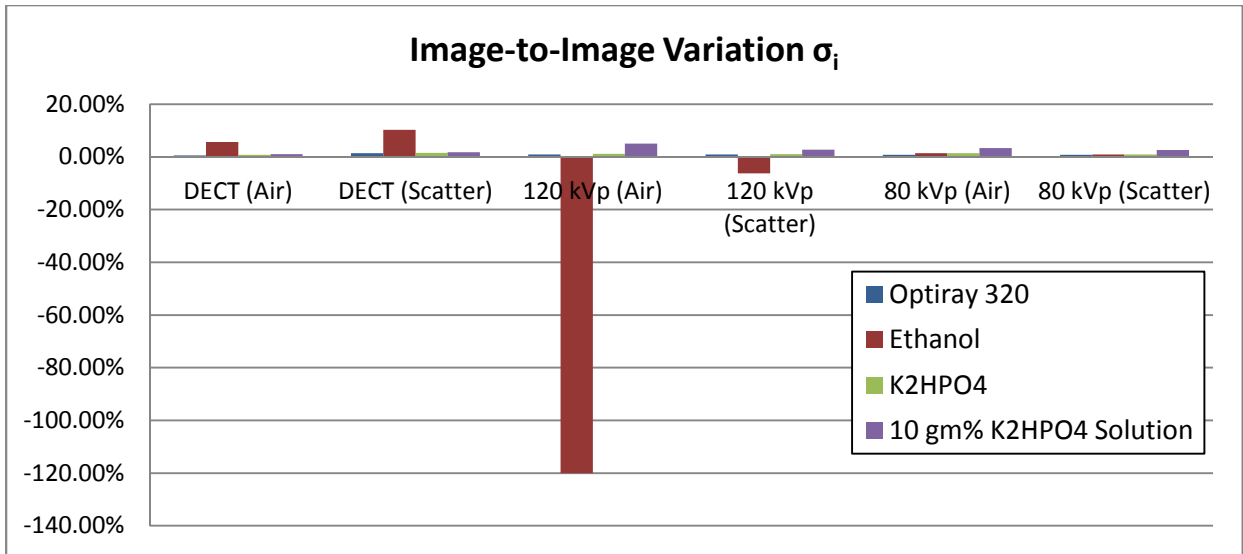


Figure 24: Variation between images as an average CV of the mean measurement assessed in DECT and SECT for Optiray 320, ethanol, K<sub>2</sub>HPO<sub>4</sub>, and 10 gm% K<sub>2</sub>HPO<sub>4</sub> solution syringe-phantoms. The very large CV for ethanol measured in air at 120 kVp is mostly due to the relatively small mean value in the denominator.

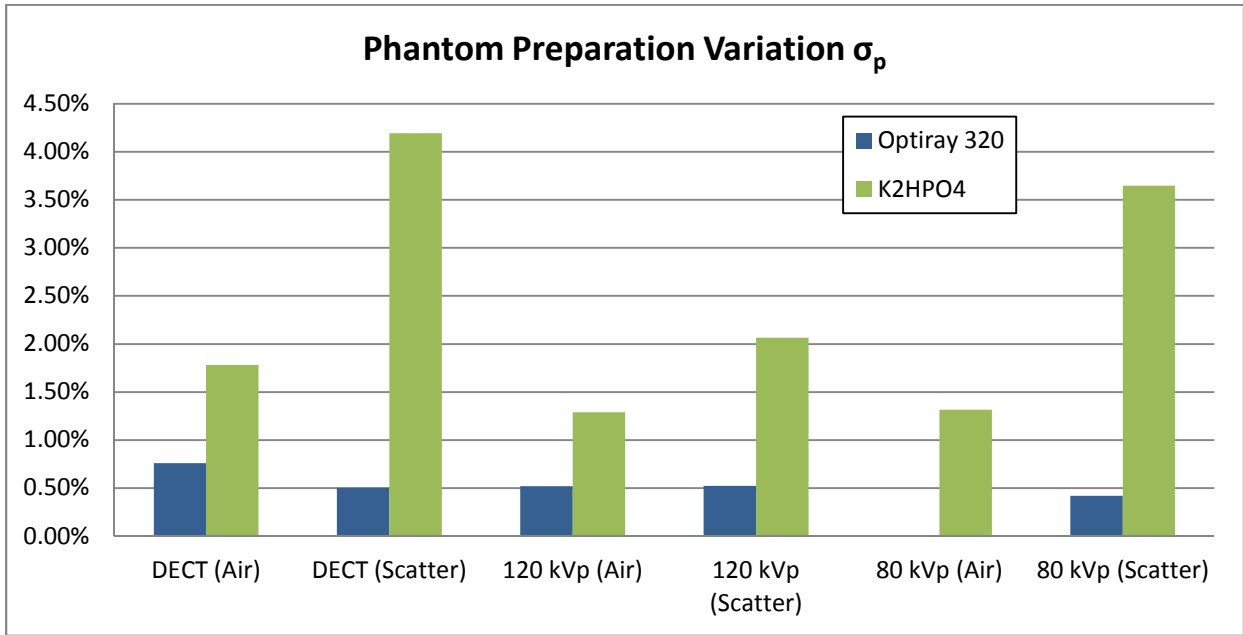


Figure 25: Variation in known concentration from phantom preparation as an average CV of the mean measurement assessed in DECT, SECT, and DXA for Optiray 320 and K<sub>2</sub>HPO<sub>4</sub> syringe-phantoms.

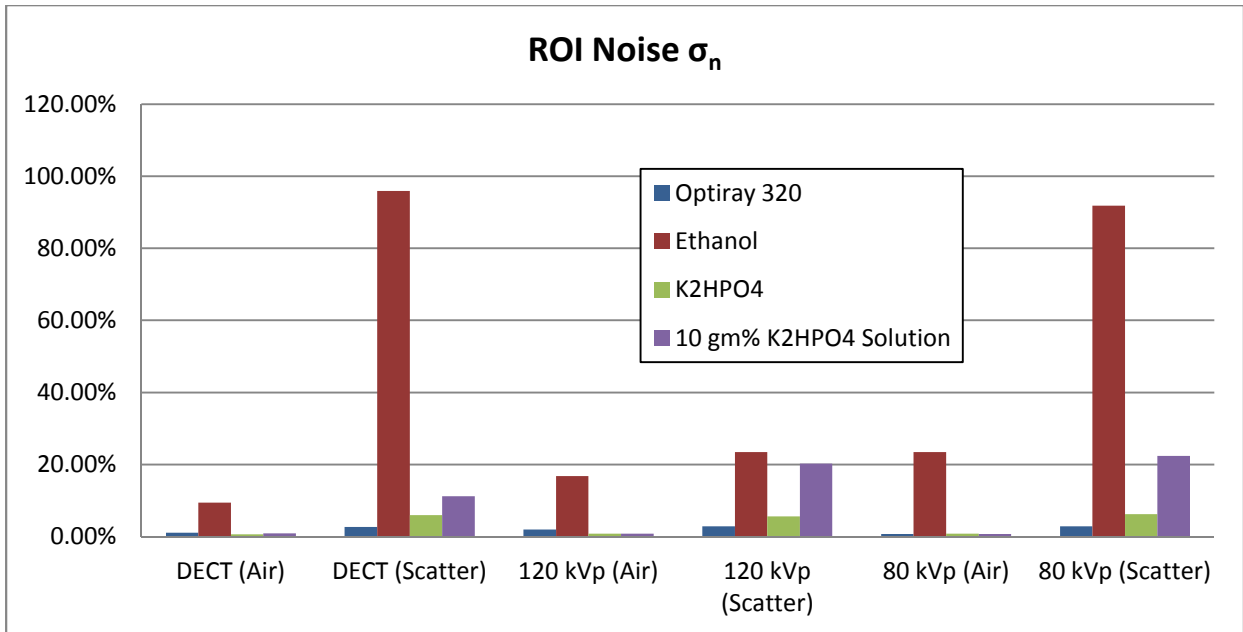


Figure 26: Variation in measured mean as an average CV of the mean measurement assessed in DECT and SECT for Optiray 320, ethanol, K<sub>2</sub>HPO<sub>4</sub>, and 10 gm% K<sub>2</sub>HPO<sub>4</sub> solution syringe-phantoms.



*Figure 27: Total variation as an average CV of the mean measurement assessed in DECT, SECT, and DXA for Optiray 320, ethanol,  $K_2HPO_4$ , and 10 gm%  $K_2HPO_4$  solution syringe-phantoms. The very large CV for ethanol is partially due to the relatively small mean value in the denominator.*

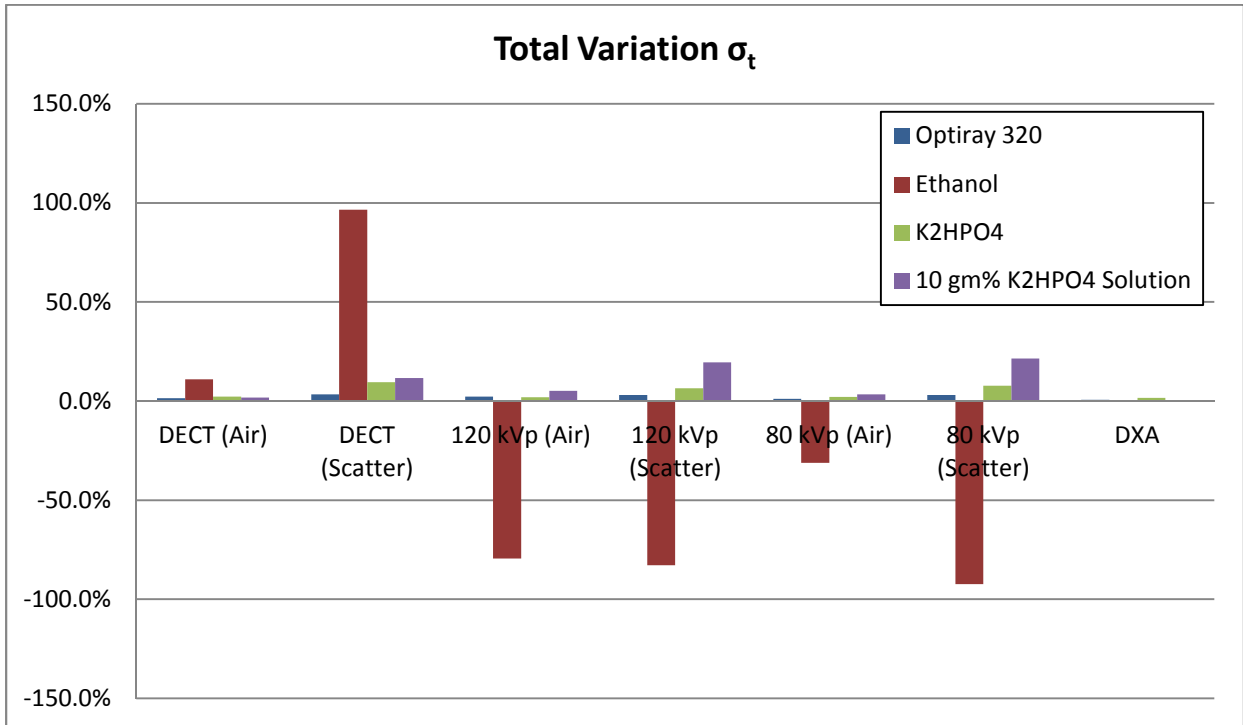


Table 18 summarizes the scan-to-scan variation  $\sigma_r$  of each measurement method for comparison, excluding ethanol due to the large CVs. Variation  $\sigma_r$  is greatest for the DECT scanner measurements in scattering conditions (7%), while it is greatest for DXA (0.2%).

Table 18: Variation between scans as an average CV of the mean measurement across all syringe-phantoms except for ethanol for DECT, SECT and DXA in air and in scattering conditions.

Measurement Method	Scan-to-Scan Variation $\sigma_r$
DXA	0.2%
120 kVp Air	0.4%

80 kVp Air	0.4%
DECT Air	0.8%
80 kVp Scatter	1%
120 kVp Scatter	1%
DECT Scatter	7%

### 3.1.2.3. Discussion

While the effects of the GSI protocol used and position relative to isocenter produced only small (< 5%) reductions (Table 15), the large reductions (~9-26%) (Table 16) in material density image-derived concentrations obtained in scattering conditions indicates sensitivity of these measurements to scan conditions. The reductions seem to correlate with the amount of scattering material surrounding each syringe-phantom. Because the amount of soft tissue attenuation will vary between patients, or a single patient may have different amounts of tissue at different time points due to weight loss or gain, the observed variation in GSI values with phantom size may be problematic for clinical interpretation. While dual-energy x-ray imaging would ideally compensate for effects such as the amount of non-bone tissue, beam hardening, and scatter, its similarity in behavior to SECT suggest certain limitations in the preprocessing algorithm used in the GSI Viewer software. Because the indicated protocol and anatomic positioning will differ for each patient in a clinical situation, the observed differences between measurements made on and off isocenter and between GSI protocols contribute to the poor accuracy, although their effect is relatively small.

Comparing the sources of variation in air and in scattering conditions, the variation between scans was smallest for DXA (Table 9), indicating it has the most stability between scans of the three measurement methods. DXA is known to have a low variation between scans, which is an important reason for its status as the gold standard of bone mineral assessment (74). In scattering conditions, DECT measurements had a relatively high variation between scans and in scatter had the highest of the measurement methods assessed, suggesting a potential problem for the use of DECT measurements in screening for bone mineral loss. Because DECT data is derived from two sets of single-energy data, the sources

of variation in each beam may act in a cumulative fashion to decrease the precision of DECT. There is also likely to be additional variation introduced in the preprocessing basis pair computations.

## **3.2. Subaim 2: Measurements in Bone Geometry Models**

### **3.2.1. Concentric Phantom Accuracy**

#### **3.2.1.1. Materials and Methods**

The objective of this study was to assess the performance of the material density images when imaging phantoms that model the geometry of human bones. Concentric phantoms were constructed and scanned to ascertain if there were differences in material density image-derived concentrations under bone-like conditions relative to uniform syringe-phantoms. Thirteen concentric phantoms were prepared, consisting of a 5 mL cylindrical plastic vial (diameter =  $\frac{1}{2}$  in. or 1.3 cm) containing a solution of  $K_2HPO_4$  in water placed inside a 50 mL plastic centrifuge tube (diameter = 3.0 cm) containing Optiray 320 solution. The less-attenuating inner solution of  $K_2HPO_4$  was constructed to simulate trabecular bone, while the more-attenuating outer solution of Optiray 320 was constructed to simulate cortical bone. Two sets of concentric phantoms were created, each designated as (X%/Y%) where X is the concentration by volume of  $K_2HPO_4$  in the inner chamber and Y is the concentration by volume of Optiray 320 in the outer chamber, as per Table 19 and Figure 28. One set was constructed with the concentration of the inner solution fixed at 10% by volume and the concentration of the outer solution increasing in increments of 5% per volume from 0-30% and the other with the outer solution fixed and the inner solution increasing in concentration. Two concentric phantoms (0%/0%, containing only water in each chamber, and 10%/10%) were shared between the sets. Dual and single-energy scans were acquired with the concentric phantom placed in the electron density body phantom in air and in scattering conditions as described in Section 3.1.1.1 (Figure 29). Measurements of the average concentration and HU were made

using the GSI Viewer software with circular ROIs drawn within the cross-section of the inner cylindrical volume (44-47 mm<sup>2</sup>) and the within the annular cross-section of the outer cylindrical volume (19-23 mm<sup>2</sup>) (Figure 30). In addition, each concentric phantom was scanned in the DXA scanner using the same methodology as described in Section 3.1.1.1, with rectangular ROIs drawn on area corresponding to the inner and outer solution (Figure 31)

*Table 19: Description of concentric phantoms constructed for concentric phantom experiments. Each value is represented as a percent by volume concentration formatted as concentration of K<sub>2</sub>HPO<sub>4</sub> by volume/concentration of Optiray 320 by volume. The 0%/0% concentric phantom contains only water in the inner and outer chambers. The 0%/0% and 10%/10% concentric phantoms were shared between the two sets.*

K <sub>2</sub> HPO <sub>4</sub> / Optiray 320	0%/0%	5%/10%	10%/10%	15%/10%	20%/10%	25%/10%	30%/10%
K <sub>2</sub> HPO <sub>4</sub> / Optiray 320		10%/5%		10%/15%	10%/20%	10%/25%	10%/30%

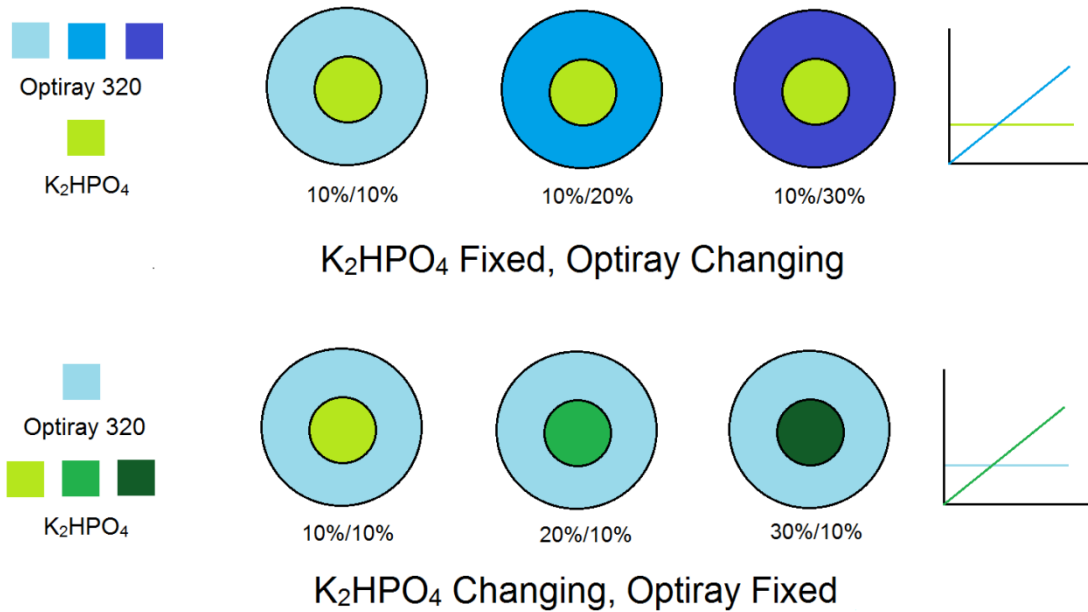


Figure 28: Diagram describing the two sets of concentric phantoms constructed for Section 3.2.1. The color blue represents Optiray 320 solution and the color green represents  $K_2HPO_4$  solution. The increasing concentration of the solute is represented by the darkening hue of each color. The simplified diagrams on the far right illustrate for which solution the concentration was increased and for which solution the concentration remained fixed in each set.

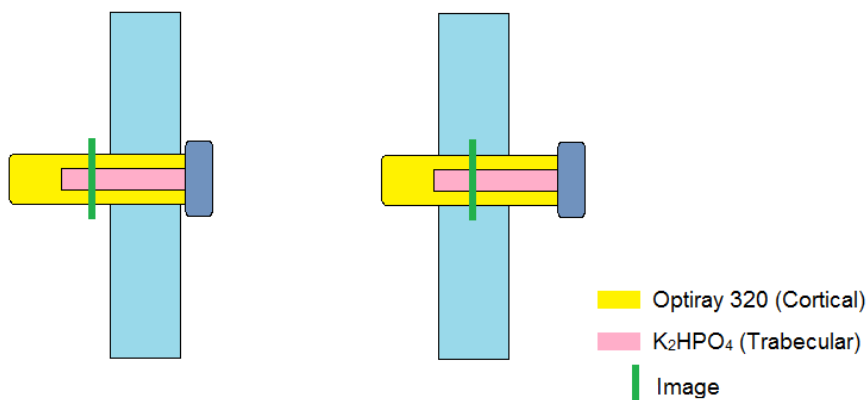


Figure 29: Configuration of materials for concentric phantom DECT and SECT measurements in air (left) and in scattering conditions (right).

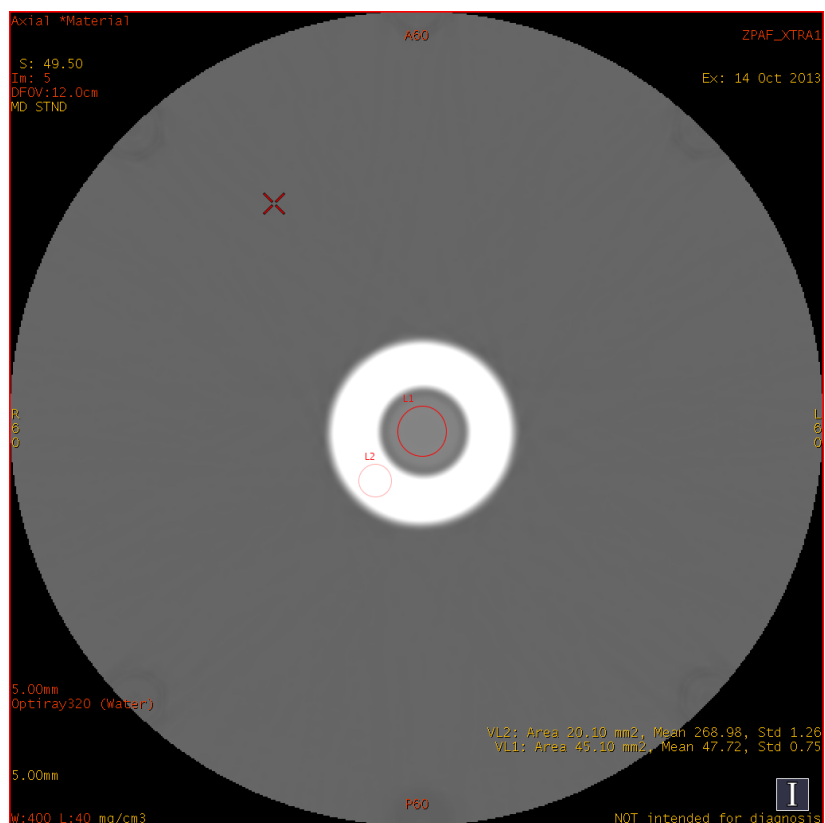


Figure 30: Example GSI Viewer in-air measurements of the  $K_2HPO_4$  concentration in the inner circular area and the Optiray 320 concentration in the annular area surrounding. The Optiray 320-water basis pair is used in this illustration.

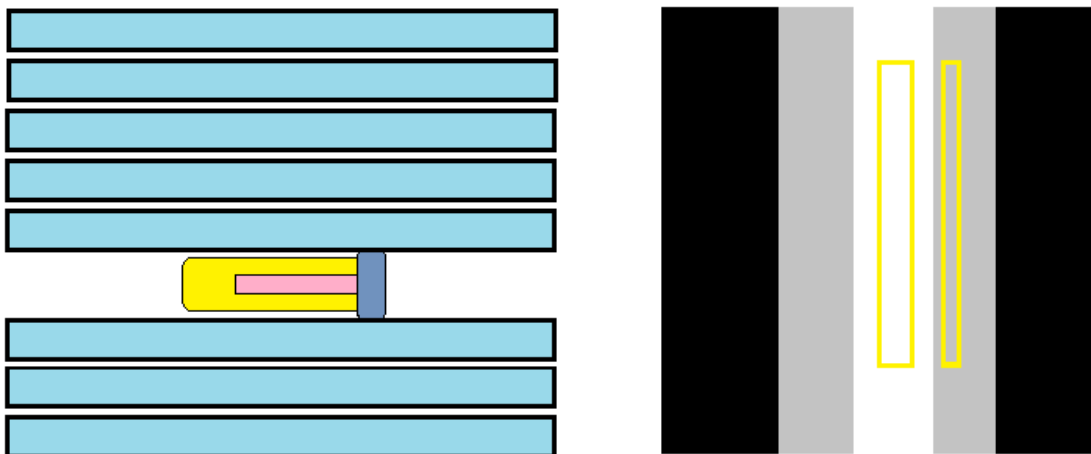


Figure 31: Left: Placement of concentric phantoms for DXA scanning. Right: Rectangular ROIs drawn on DXA image of concentric phantoms for the inner and outer chambers.

For both the outer and inner solution, the measured concentration, HU, or aBMD was plotted against the measurement made in the uniform syringe-phantom with the equivalent concentration (but not the exact same solution). The data were fit with a linear regression and the slope with 95% confidence intervals was compared with an expected value of either 1 or 0 with an f-test. Regressions with a y-intercept consistent with 0 within 95% confidence limits were re-fit with a y intercept equal to 0. To produce error bars on the y-axis, an estimate of the total variation  $\sigma_t$  of the concentric measurements was assessed with the CV between images  $\sigma_i$ , phantom preparation  $\sigma_p$ , and variation between scans  $\sigma_r$  were taken from the uniform syringe-phantom data and the noise  $\sigma_n$  was taken from measurements made in the individual concentric phantoms.

### **3.2.1.2. Results**

#### 3.2.1.2.1 DECT Concentric Phantom Accuracy

Most of the slopes measured did not vary significantly ( $p < 0.5$ ) from their expected value of unity or 0 (Table 20, Figures 33-34). The measured concentration of  $K_2HPO_4$  in the inner chamber, while a fixed concentration of Optiray 320 was present in the outer chamber, was higher by ~13% in air than those measured for the uniform  $K_2HPO_4$  phantom (Figure 32, top). The measured concentration of Optiray 320 in the outer chamber, while a fixed concentration of  $K_2HPO_4$  was present in the inner chamber, was lower by ~12% than measured in the uniform Optiray 320 phantom (Figure 33, top). Most notably, however, the  $K_2HPO_4$  concentration increased in the phantoms in which the  $K_2HPO_4$  concentration was fixed and the Optiray 320 concentration increased (Figure 33, bottom) both in air and in scattering conditions. The in-air measured concentration of  $K_2HPO_4$  ranged from 276 mg/mL—399 mg/mL while the expected concentration based on in-air measurement in the uniform 10%  $K_2HPO_4$  syringe-phantom was just  $258 \pm 6$  mg/mL.



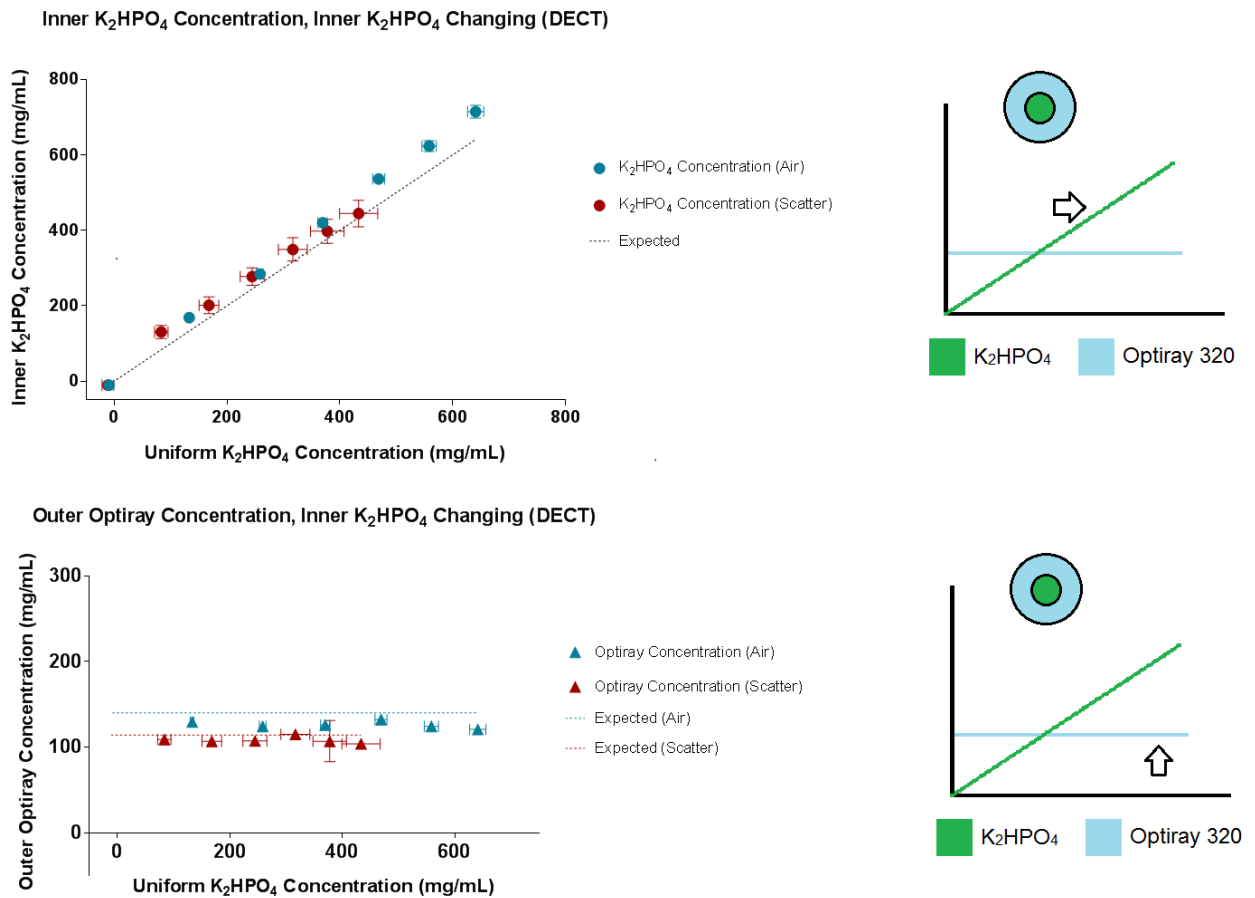


Figure 32: Material density image concentration measurements in air and scattering conditions of concentric phantoms where the inner  $K_2HPO_4$  solution concentration increases and the outer Optiray 320 solution concentration is fixed. Error bars on the x-axis and y-axis indicate the total variation of the uniform solution measurement and the measurement made in the concentric phantom, respectively. Top Left: Measurements of  $K_2HPO_4$  concentration. A slope of 1 is expected for both measurements; in-air measurements yielded a slope of  $1.13 \pm 0.03$  and scatter measurements yielded a slope of  $1.08 \pm 0.08$ . Bottom Left: Measurements of Optiray 320 concentration. A slope of 0 is expected for both measurements; in-air and scatter measurements both yielded a slope of  $-0.01 \pm 0.04$ . Right: Graphic based on Figure 28 illustrating which solution concentration is changing, which solution concentration is fixed, and which is being plotted to the left (arrow).

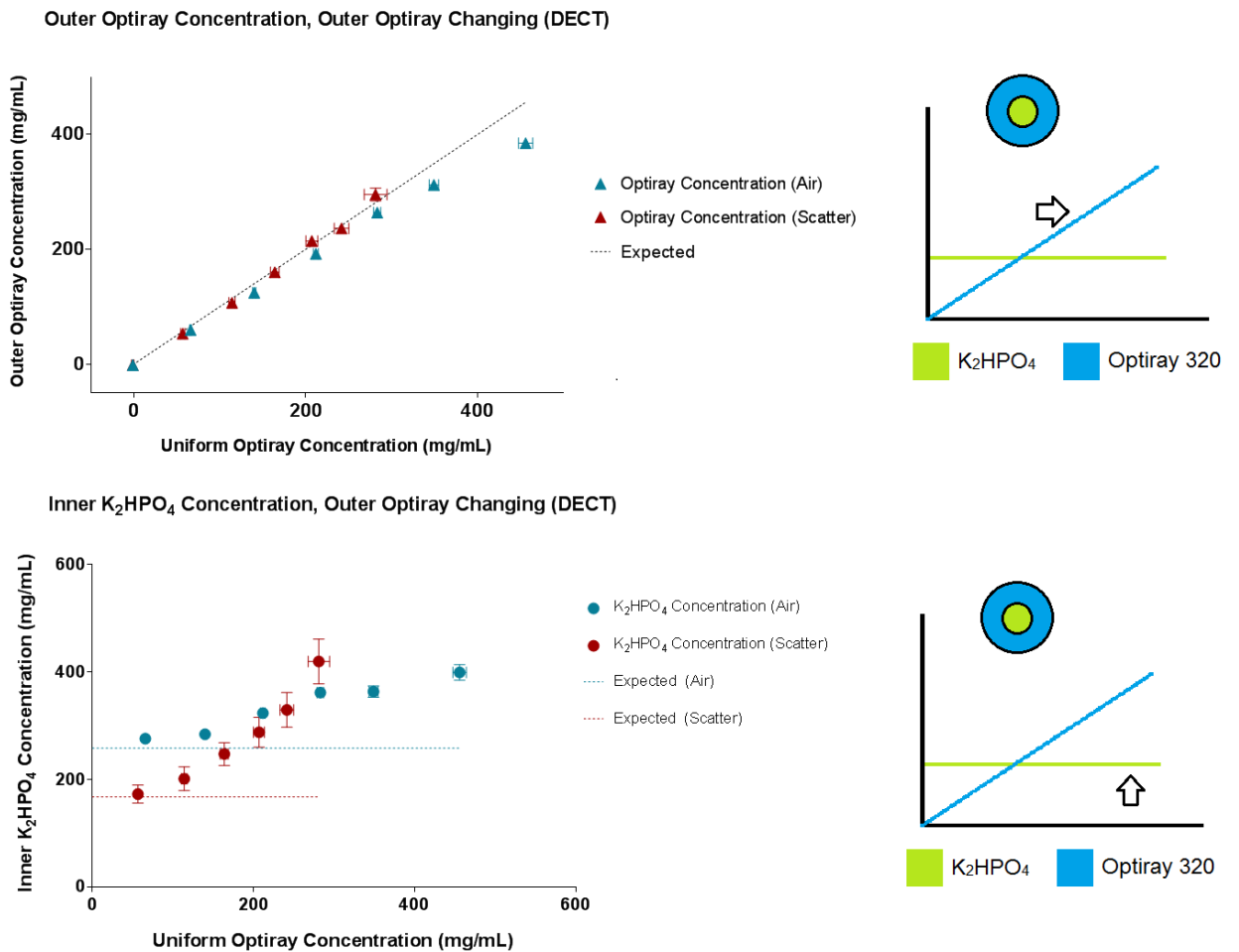


Figure 33: Material density image concentration measurements in air and scattering conditions of concentric phantoms where the inner  $K_2HPO_4$  solution concentration is fixed and the outer Optiray 320 solution concentration increases. Error bars on the x-axis and y-axis indicate the total variation of the uniform solution measurement and the measurement made in the concentric phantom, respectively. Top Left: Measurements of Optiray 320 concentration. A slope of 1 is expected for both measurements; in-air measurements yielded a slope of  $0.88 \pm 0.03$  and scatter measurements yielded a slope of  $1.01 \pm 0.04$ . Bottom Left: Measurements of  $K_2HPO_4$  concentration. A slope of 0 is expected for both measurements; in-air measurements yielded a slope of  $0.3 \pm 0.1$  and scatter measurements yielded a slope of  $1.1 \pm 0.4$ . Right: Graphic based on Figure 28 illustrating which solution concentration is changing, which solution concentration is fixed, and which is being plotted to the left (arrow).

Table 20: Slope with 95% confidence intervals compared for a regression of the concentration measured in the concentric phantom vs the concentration measured in the uniform syringe-phantom. Each concentric phantom was scanned both in air and in scattering conditions and compared with the uniform syringe-phantom with both the equivalent concentration of  $K_2HPO_4$  and Optiray 320 in those conditions. When the concentration of the material analyzed was fixed, it was expected that the slope of the regression would be 0. When the concentration of the material analyzed was changing, it was expected that the slope of the regression would be unity. Slopes considered different from expectation are marked with a \*.

Material Analyzed (mg/mL)	Fixed Material	Changing Material	Corresponding Figure	Slope	Expected
$K_2HPO_4$ (Air)	$K_2HPO_4$ (Inner)	Optiray 320 (Outer)	Figure 33 (Bottom)	$0.3 \pm 0.1^*$	0
$K_2HPO_4$ (Scatter)	$K_2HPO_4$ (Inner)	Optiray 320 (Outer)	Figure 33 (Bottom)	$1.1 \pm 0.4^*$	0
Optiray (Air)	$K_2HPO_4$ (Inner)	Optiray 320 (Outer)	Figure 33 (Top)	$0.88 \pm 0.03^*$	1
Optiray (Scatter)	$K_2HPO_4$ (Inner)	Optiray 320 (Outer)	Figure 33 (Top)	$1.01 \pm 0.04$	1
$K_2HPO_4$ (Air)	Optiray 320 (Outer)	$K_2HPO_4$ (Inner)	Figure 32 (Top)	$1.13 \pm 0.03^*$	1
$K_2HPO_4$ (Scatter)	Optiray 320 (Outer)	$K_2HPO_4$ (Inner)	Figure 32 (Top)	$1.08 \pm 0.08$	1
Optiray (Air)	Optiray 320 (Outer)	$K_2HPO_4$ (Inner)	Figure 32 (Bottom)	$-0.01 \pm 0.04$	0
Optiray (Scatter)	Optiray 320 (Outer)	$K_2HPO_4$ (Inner)	Figure 32 (Bottom)	$-0.01 \pm 0.04$	0

### 3.2.1.2.2 SECT Concentric Phantom Correlation

The trends observed in material density image concentration measurements were mostly also observed in single-energy HU measurements (Figures 35-36, Table 21). The measured in-air CT number of  $K_2HPO_4$  for a fixed concentration ranged from 390 HU to 547 HU at 120 kVp and from 535 HU to 772 HU where a value of  $398 \pm 8$  HU and  $533 \pm 11$  HU was expected respectively (Figure 35, bottom), based on measurements in uniform syringe-

phantoms. The lower than expected Optiray measurements in concentric phantoms in which Optiray was changing was observed at 120 kVp but not at 80 kVp (Figure 35, top). The slightly higher  $K_2HPO_4$  concentration measurements in concentric phantoms where the Optiray concentration was held fixed in air was not observed (Figure 34, top). Note that for the concentric phantoms measured in air at 80 kVp in which the outer Optiray 320 concentration was 25 or 30% (Figure 35, bottom), the HU reached the maximum value the software was capable of reporting (3071 HU).

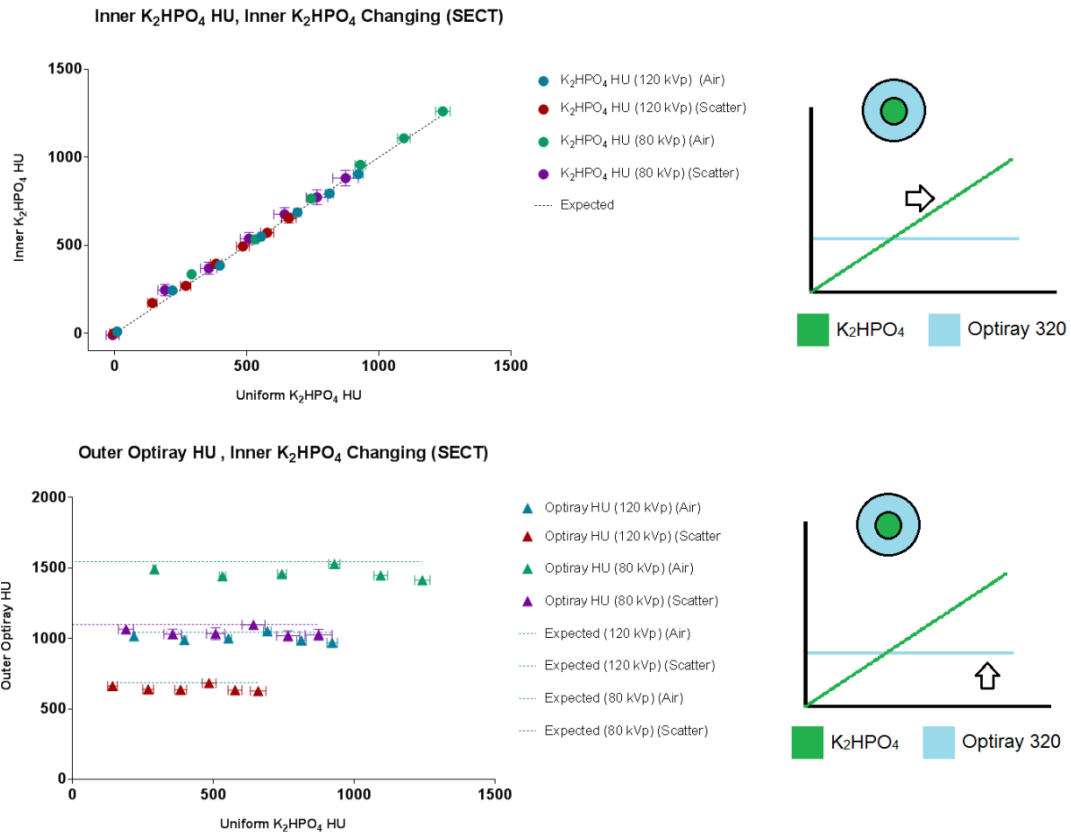


Figure 34: SECT HU measurements of concentric phantoms in air and scattering conditions at 120 and 80 kVp where the inner  $K_2HPO_4$  solution increases and the outer Optiray 320 solution concentration is fixed. Error bars on the x-axis and y-axis indicate the total variation of the uniform solution measurement and the measurement made in the concentric phantom, respectively. Top Left: Measurements of  $K_2HPO_4$  HU. A slope of 1 is expected for all measurements; in-air measurements at 120 kVp yielded a slope of  $0.99 \pm 0.02$  and scatter measurements yielded a slope of  $1.01 \pm 0.03$ . In-air measurements at 80 kVp yielded a slope of  $1.02 \pm 0.02$  and scatter measurements yielded a slope of  $1.03 \pm 0.04$ . Bottom Left: Measurements of Optiray HU. A slope of 0 is expected for all measurements; in-air and scatter measurements at 120 kVp both yielded a slope of  $0.0 \pm 0.1$ . In-air measurements at 80 kVp yielded a slope of  $0.0 \pm 0.1$  and scatter measurements yielded a slope of  $0.0 \pm 0.2$ . Right: Graphic based on Figure 28 illustrating which solution concentration is changing, which solution concentration is fixed, and which is being plotted to the left (arrow).

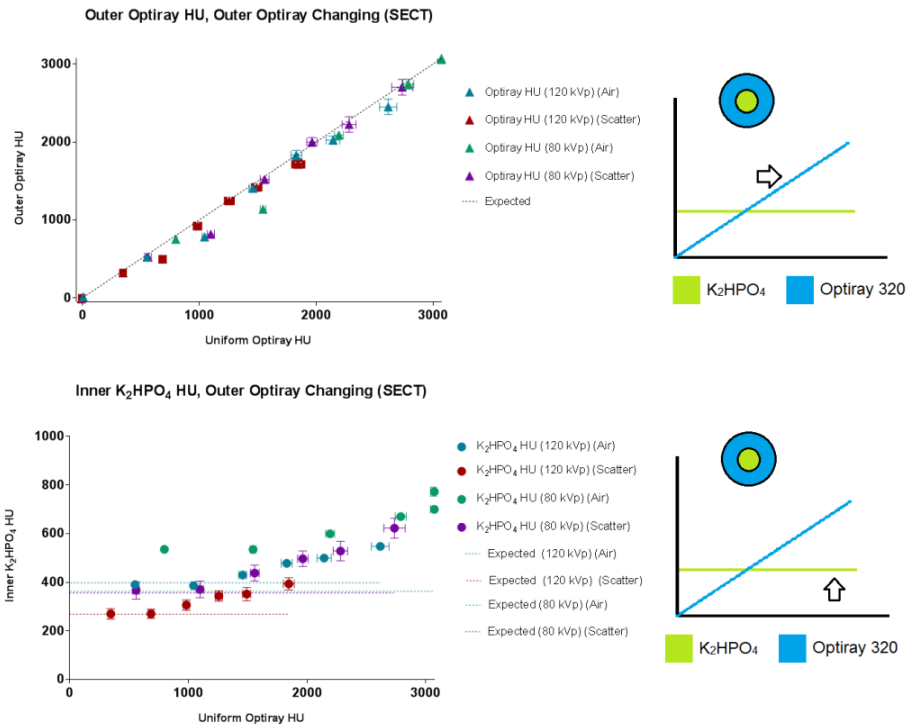


Figure 35: SECT HU measurements of concentric phantoms in air and scattering conditions at 120 and 80 kVp where the inner  $K_2HPO_4$  solution is fixed and the outer Optiray 320 solution concentration increases. Error bars on the x-axis and y-axis indicate the total variation of the uniform solution measurement and the measurement made in the concentric phantom, respectively. Top Left: Measurements of Optiray HU. A slope of 1 is expected for all measurements; in-air measurements at 120 kVp yielded a slope of  $0.94 \pm 0.5$  and scatter measurements yielded a slope of  $0.93 \pm 0.5$ . In-air measurements at 80 kVp yielded a slope of  $0.97 \pm 0.07$  and scatter measurements yielded a slope of  $0.97 \pm 0.06$ . Note that for a 30% Optiray 320 concentration, the CT number reached a maximum value at 80 kVp in air. Bottom Left: Measurements of  $K_2HPO_4$  HU. A slope of 0 is expected for all measurements; in-air measurements at 120 kVp yielded a slope of  $0.8 \pm 0.3$  and scatter measurements yielded a slope of  $0.9 \pm 0.3$ . In-air measurements at 80 kVp yielded a slope of  $0.09 \pm 0.06$  and scatter measurements yielded a slope of  $0.12 \pm 0.04$ . Right: Graphic based on Figure 28 illustrating which solution concentration is changing, which solution concentration is fixed, and which is being plotted to the left (arrow).

Table 21: Slope with 95% confidence intervals compared for a regression of the HU measured in the concentric phantom vs the HU measured in the uniform syringe-phantom in air and in scattering conditions at 120 and 80 kVp. Each concentric phantom was scanned both in air and in scattering conditions and compared with the uniform syringe-phantom with both the equivalent concentration of  $K_2HPO_4$  and Optiray 320 in those conditions. When the concentration of the material analyzed was fixed, it was expected that the slope of the regression would be 0. When the concentration of the material analyzed was changing, it was expected that the slope of the regression would be unity. Slopes considered different from expectation are marked with a \*.

Material Analyzed (HU)	Fixed Material	Changing Material	Figure	Slope	Expected
$K_2HPO_4$ (120 kVp) (Air)	$K_2HPO_4$ (Inner)	Optiray 320 (Outer)	Figure 35 (Bottom)	$0.08 \pm 0.03^*$	0
$K_2HPO_4$ (120 kVp) (Scatter)	$K_2HPO_4$ (Inner)	Optiray 320 (Outer)	Figure 35 (Bottom)	$0.09 \pm 0.03^*$	0
$K_2HPO_4$ (80 kVp) (Air)	$K_2HPO_4$ (Inner)	Optiray 320 (Outer)	Figure 35 (Bottom)	$0.09 \pm 0.06^*$	0
$K_2HPO_4$ (80 kVp) (Scatter)	$K_2HPO_4$ (Inner)	Optiray 320 (Outer)	Figure 35 (Bottom)	$0.12 \pm 0.04^*$	0
$K_2HPO_4$ (120 kVp) (Air)	Optiray 320 (Outer)	$K_2HPO_4$ (Inner)	Figure 34 (Top)	$0.99 \pm 0.02$	1
$K_2HPO_4$ (120 kVp) (Scatter)	Optiray 320 (Outer)	$K_2HPO_4$ (Inner)	Figure 34 (Top)	$1.01 \pm 0.03$	1
$K_2HPO_4$ (80 kVp) (Air)	Optiray 320 (Outer)	$K_2HPO_4$ (Inner)	Figure 34 (Top)	$1.02 \pm 0.02$	1
$K_2HPO_4$ (80 kVp) (Scatter)	Optiray 320 (Outer)	$K_2HPO_4$ (Inner)	Figure 34 (Top)	$1.03 \pm 0.04$	1
Optiray 320 (120 kVp) (Air)	Optiray 320 (Outer)	$K_2HPO_4$ (Inner)	Figure 34 (Bottom)	$0.0 \pm 0.1$	0
Optiray 320 (120 kVp) (Scatter)	Optiray 320 (Outer)	$K_2HPO_4$ (Inner)	Figure 34 (Bottom)	$0.0 \pm 0.1$	0
Optiray 320 (80 kVp) (Air)	Optiray 320 (Outer)	$K_2HPO_4$ (Inner)	Figure 34 (Bottom)	$0.0 \pm 0.1$	0
Optiray 320 (80 kVp) (Scatter)	Optiray 320 (Outer)	$K_2HPO_4$ (Inner)	Figure 34 (Bottom)	$0.0 \pm 0.2$	0
Optiray 320 (120 kVp) (Air)	$K_2HPO_4$ (Inner)	Optiray 320 (Outer)	Figure 35 (Top)	$0.94 \pm 0.5^*$	1

Optiray 320 (120 kVp) (Scatter)	K <sub>2</sub> HPO <sub>4</sub> (Inner)	Optiray 320 (Outer)	Figure 35 (Top)	0.93 ± 0.05*	1
Optiray 320 (80 kVp) (Air)	K <sub>2</sub> HPO <sub>4</sub> (Inner)	Optiray 320 (Outer)	Figure 35 (Top)	0.97 ± 0.07	1
Optiray 320 (80 kVp) (Scatter)	K <sub>2</sub> HPO <sub>4</sub> (Inner)	Optiray 320 (Outer)	Figure 35 (Top)	0.97 ± 0.06	1

### 3.2.1.2.3 DXA Concentric Phantom Correlations

DXA measurements of concentric phantoms are summarized in Figures 37-38. Similar to the trend observed in DECT and SECT, aBMD measurements of K<sub>2</sub>HPO<sub>4</sub> in the inner chamber had a positive, nonzero slope ( $0.58 \pm 0.03$ ) despite a fixed concentration (Figure 37, bottom, Table 22). This measurement also had a higher offset than expected by about 0.26 g/cm<sup>2</sup>. Measurements of Optiray 320 in the outer chamber, conversely, had a lower slope than expected when the concentration was increased (Figure 37, top). This was also true of measurements of K<sub>2</sub>HPO<sub>4</sub> in the inner chamber while the concentration increased and the concentration of the Optiray 320 in the outer chamber remained fixed (Figure 36, top). There was also a large offset in this measurement, about 1.3 g/cm<sup>2</sup> greater than the expected value (0 g/cm<sup>2</sup>). The offset for outer chamber Optiray 320 measurements in this set of concentric phantoms was less than the expected value by about 0.6 g/cm<sup>2</sup> (Figure 36, bottom).



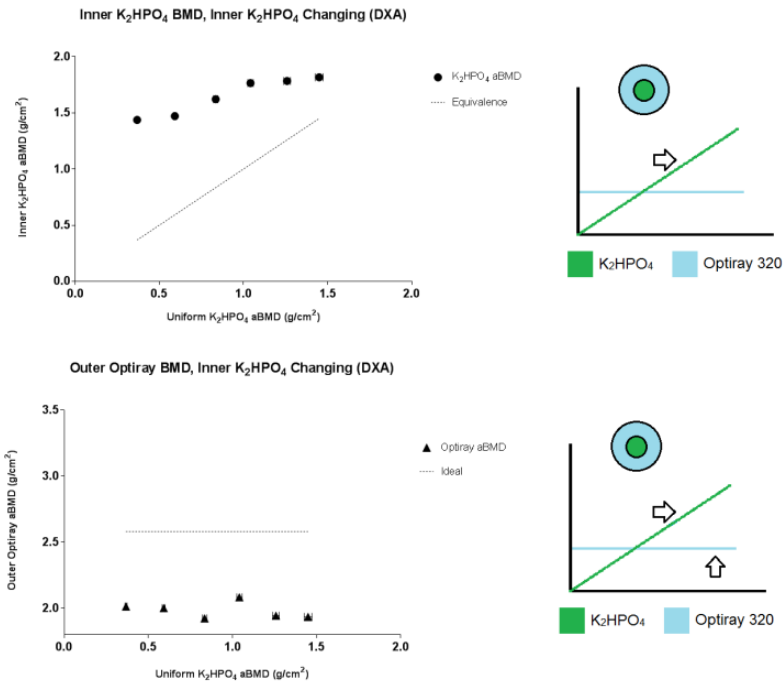


Figure 36: DXA aBMD measurements of concentric phantoms where the inner  $K_2HPO_4$  solution increases and the outer Optiray 320 solution concentration is fixed. Error bars on the x-axis and y-axis indicate the total variation of the uniform solution measurement and the measurement made in the concentric phantom, respectively. Top Left: Measurements of  $K_2HPO_4$  aBMD. A slope of 1 and offset of 0 is expected; measurements yielded a slope of  $0.4 \pm 0.1$  and an offset of  $1.3 \pm 0.1$ . Bottom Left: Measurements of Optiray aBMD. A slope of 0 and offset of  $2.58 \pm 0.02$  is expected; measurements yielded a slope of  $-0.1 \pm 0.2$  and an offset of  $2.0 \pm 0.2$ . Right: Graphic based on Figure 28 illustrating which solution concentration is changing, which solution concentration is fixed and which is being plotted to the left (arrow).

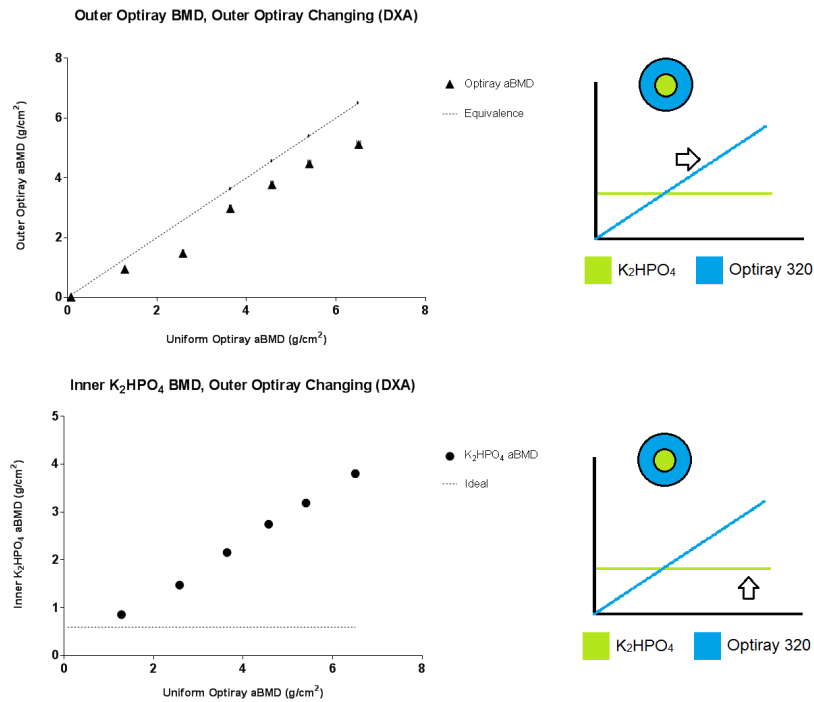


Figure 37: DXA aBMD measurements of concentric phantoms for which the inner K<sub>2</sub>HPO<sub>4</sub> concentration is fixed and the outer Optiray 320 solution concentration increases. Error bars on the x-axis and y-axis indicate the total variation of the uniform solution measurement and the measurement made in the concentric phantom, respectively. Top left: Measurements of Optiray aBMD. An offset of 0 and slope of 1 is expected; measurements yielded a slope of  $0.8 \pm 0.1$  and an offset of  $-0.2 \pm 0.5$ . Bottom left: Measurements of K<sub>2</sub>HPO<sub>4</sub> aBMD. A slope of 0 and an offset of  $0.592 \pm 0.009$  is expected; measurements yielded a slope of  $0.58 \pm 0.03$  and an offset of  $0.85 \pm 0.01$ . Right: Graphic based on Figure 28 illustrating which solution concentration is changing, which solution concentration is fixed and which is being plotted to the left (arrow).

Table 22: Slope and offsets with 95% confidence intervals compared for a regression of the aBMD measured in the concentric phantom vs the aBMD measured in the uniform syringe-phantom. Each concentric phantom was scanned between eight 3/8 in. (9.5 mm) PMMA blocks and compared with the uniform syringe-phantom with both the equivalent concentration of  $K_2HPO_4$  and Optiray 320 in those conditions. When the concentration of the material analyzed was fixed, it was expected that the slope of the regression would be 0. When the concentration of the material analyzed was changing, it was expected that the slope of the regression would be unity. The expected offset is the measurement of the uniform syringe-phantom of equivalent concentration to the material being analyzed  $\pm$  the total variation in the uniform syringe-phantom measurement or 0 if the material being analyzed is changing in concentration. Slopes and offsets considered different from expectation are marked with a \*.

Measurement, Phantom	Corresponding Figure	Slope	Expected Slope	Offset (g/cm <sup>2</sup> )	Expected Offset (g/cm <sup>2</sup> )
$K_2HPO_4$ aBMD, Optiray Changing	Figure 37 (Bottom)	$0.58 \pm 0.03^*$	0	$0.85 \pm 0.01^*$	$0.592 \pm 0.009$
Optiray aBMD, $K_2HPO_4$ Changing	Figure 36 (Bottom)	$-0.1 \pm 0.2$	0	$2.0 \pm 0.2^*$	$2.58 \pm 0.02$
Optiray aBMD, Optiray Changing	Figure 37 (Top)	$0.8 \pm 0.1$	1	$-0.2 \pm 0.5$	0
$K_2HPO_4$ aBMD, $K_2HPO_4$ Changing	Figure 36 (Top)	$0.4 \pm 0.1$	1	$1.3 \pm 0.1^*$	0

### 3.2.1.3. Discussion

In theory, in three-dimensional images of two concentric cylinders each containing two materials, the concentration of one material should not affect measurements made in another. However, we measured and increasing value in the inner  $K_2HPO_4$  solution with increasing Optiray 320 concentration, despite a fixed composition. The effect appears in both DECT (Figure 33, bottom) and SECT (Figure 35, bottom) indicating that, as in the scattering conditions experiments in Section 3.1.2, the effect is likely caused by inaccuracies in the DECT

material decomposition reconstruction from the single-energy data. Since every line integral through this region contains the high attenuation (relative to  $K_2HPO_4$ ) from the surrounding Optiray 320, the effect may be attributed to limitations in the filtered back-projection used to reconstruct the dual and single-energy CT images; that is, some attenuation from Optiray 320 may have “smeared” across the regions containing  $K_2HPO_4$ . The effect in this case is the opposite from what might be expected in a beam hardening artifact, in which the measured concentration or HU of the  $K_2HPO_4$  solution might be expected to be lower than for a uniform solution of the same concentration. Back-projection errors may also be responsible for the deviation of the slope for the changing Optiray 320 concentration from 1 (Figure 33, Figure 35). Higher variation in each measurement compared to in air may mask this effect in scattering conditions in DECT.

It is not clear why in-air DECT concentration measurements of  $K_2HPO_4$  are greater (~13%) when surrounded by a fixed Optiray concentration than those measured in uniform phantoms (Figure 32) as the corresponding effect is not present in single-energy data. As for the Optiray measurements in increasing Optiray concentrations (Figure 33), the effect may be masked in scattering conditions by the greater variation in each DECT measurement compared to in air. It is unknown how the GSI Viewer software combines the data from each single-energy beam. It is possible that while the greater than expected  $K_2HPO_4$  measurements in a changing  $K_2HPO_4$  concentration are not discernable in single-energy data, there is an cumulative effect when constructing dual-energy images. This cumulative effect may also explain why the Optiray concentration measurements for a changing Optiray concentration in air are lower than expected in DECT and at 120 kVp but not at 80 kVp.

The DXA measurements of the concentric phantoms demonstrate quantitative inaccuracy stemming from signal integration. The concentration of the outer solute was expected to contribute to the aBMD of the inner solute measured by DXA and lead to inaccurate measurements. Consistent with expectations, although the inner  $K_2HPO_4$  solution

(meant to represent trabecular bone) concentration was held constant, the DXA aBMD increased with higher Optiray 320 (meant to represent cortical bone) concentration present in the outer chamber (Figure 37, bottom). The integration methodology also causes differences in aBMD measurements due to different phantom geometries. DXA measurements of Optiray 320 aBMD with a changing concentration (Figure 37), even when made without integration through a  $K_2HPO_4$  solution, were less (~20%) than those made with in the uniform syringe-phantoms with 95% confidence. This is due to differences in the thickness of the cylinders across the area presented to the DXA beam and the different diameter of the concentric vs the uniform syringe-phantom cylinders (3.0 vs. 2.5 cm). When a DXA measurement is made off the axis of a cylinder, the x-ray beam travels through a smaller thickness of the solution compared to a measurement made along the axis of the same area, resulting in a smaller average aBMD. The same is true for measurements of the same area made in the same location on two cylinders of different diameter (Figure 38).

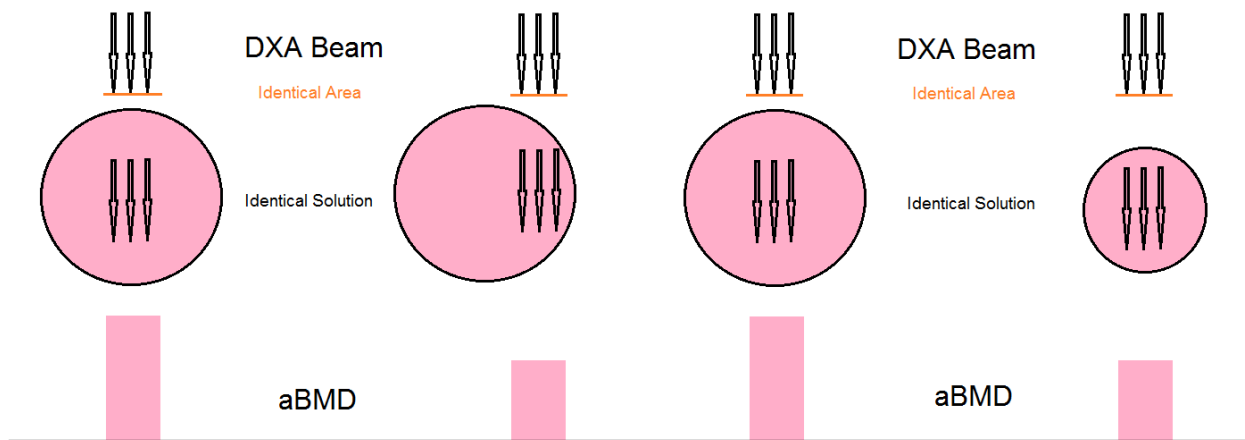


Figure 38: The aBMD varies for the same size and shaped ROI area on a cylinder depending on position transverse to the axis and cylinder diameter.

### 3.2.2. Reversed Concentric Phantoms

#### 3.2.2.1. Materials and Methods

To further investigate the increasing  $K_2HPO_4$  measurements for a fixed concentration observed in DECT and SECT measurements in Section 3.2.1.2, three additional concentric phantoms were constructed with the placement of the  $K_2HPO_4$  and Optiray 320 solutions reversed (Figure 39). The inner 5 mL vial was filled with an Optiray 320 dilution in water with a concentration of 10, 20, or 30% by volume and the outer 50 mL centrifuge tube was filled with a 10% by volume solution of  $K_2HPO_4$  in water for all three concentric phantoms. Dual and single-energy CT scans were acquired and analyzed in the same manner as Section 3.2.1.1.

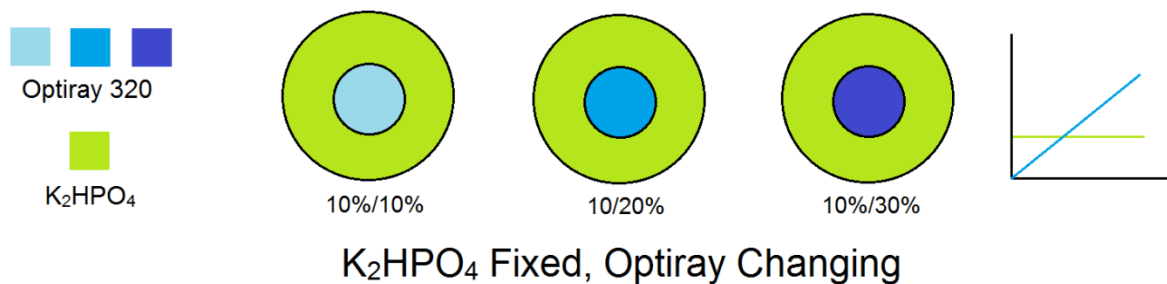


Figure 39: Diagram based on Figure 28 describing the set of three “reverse” concentric phantoms constructed for the reversed concentric phantom experiment. The color blue represents Optiray 320 solution, while the color green represents  $K_2HPO_4$  solution. The increasing concentration of the Optiray 320 represented by the darkening hue. The simplified diagram on the far right illustrates for which solution the concentration was increased and for which solution the concentration remained fixed, as in Figure 28.

### 3.2.2.2. Results

The results for DECT are summarized in Figure 40 and SECT in Figure 41. To produce error bars on the y-axis, an estimate of the total variation  $\sigma_t$  of the concentric measurements was assessed with the CV between images  $\sigma_i$ , phantom preparation  $\sigma_p$ , and variation between scans  $\sigma_r$ , were taken from the uniform syringe-phantom data and the noise  $\sigma_n$  was taken from the measurement made in the individual reversed concentric phantoms. The Optiray solution with a nominal concentration of 20% by volume appears to have been prepared incorrectly; nonetheless, a general trend is apparent. In every plot the measured concentration and HU of the Optiray 320 solution is increasing with concentration while the measured value of the  $K_2HPO_4$  solution remains relatively fixed.

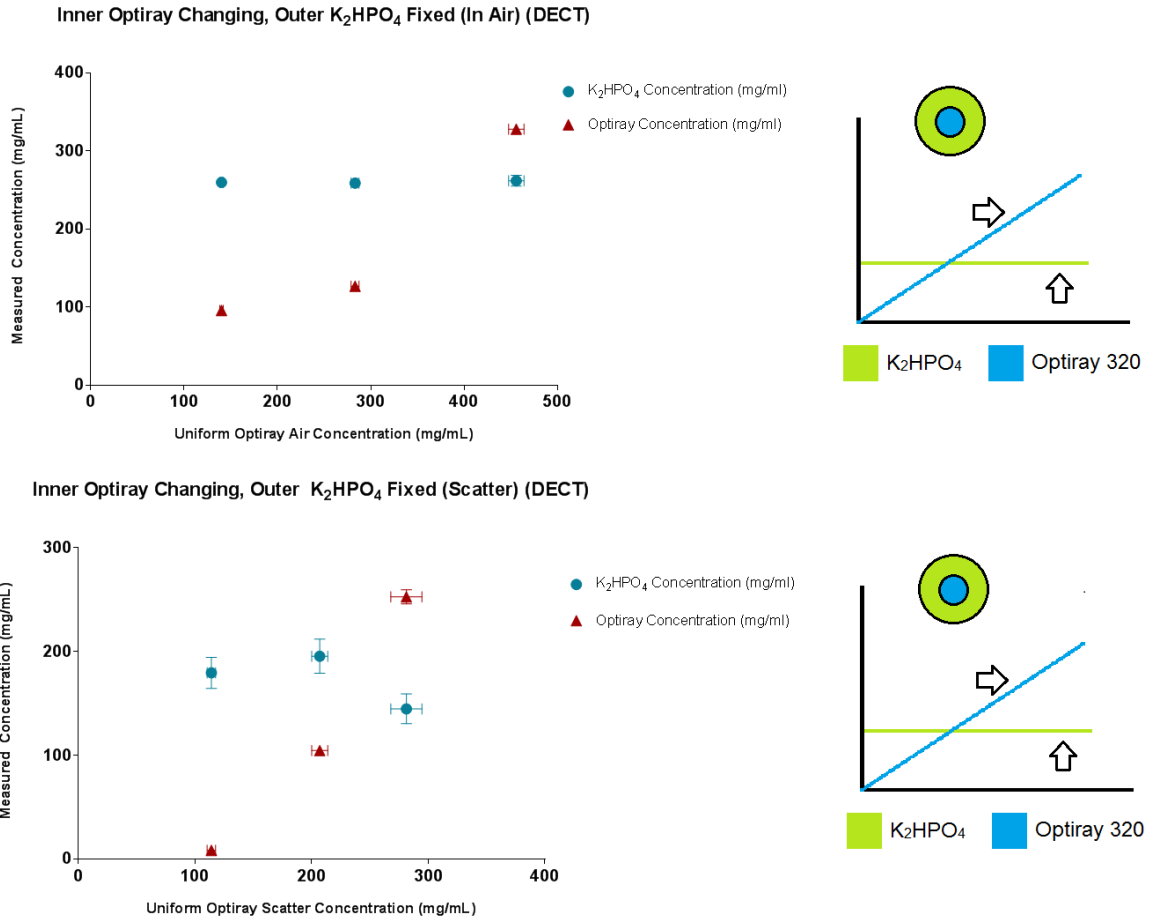


Figure 40: Left: Material density image concentration measurements in air (Top) and in scattering conditions (Bottom) of the inner Optiray 320 solution of increasing concentration, where the outer  $K_2HPO_4$  solution concentration was fixed. Error bars on the x-axis and y-axis indicate the total variation of the uniform solution measurement and the measurement made in the concentric phantom, respectively. The point corresponding to 20% Optiray concentration appears to reflect an improper Optiray solution preparation. Right: Graphic based on Figure 39 illustrating which solution concentration is changing, which solution concentration is fixed and which is being plotted to the left (arrow).



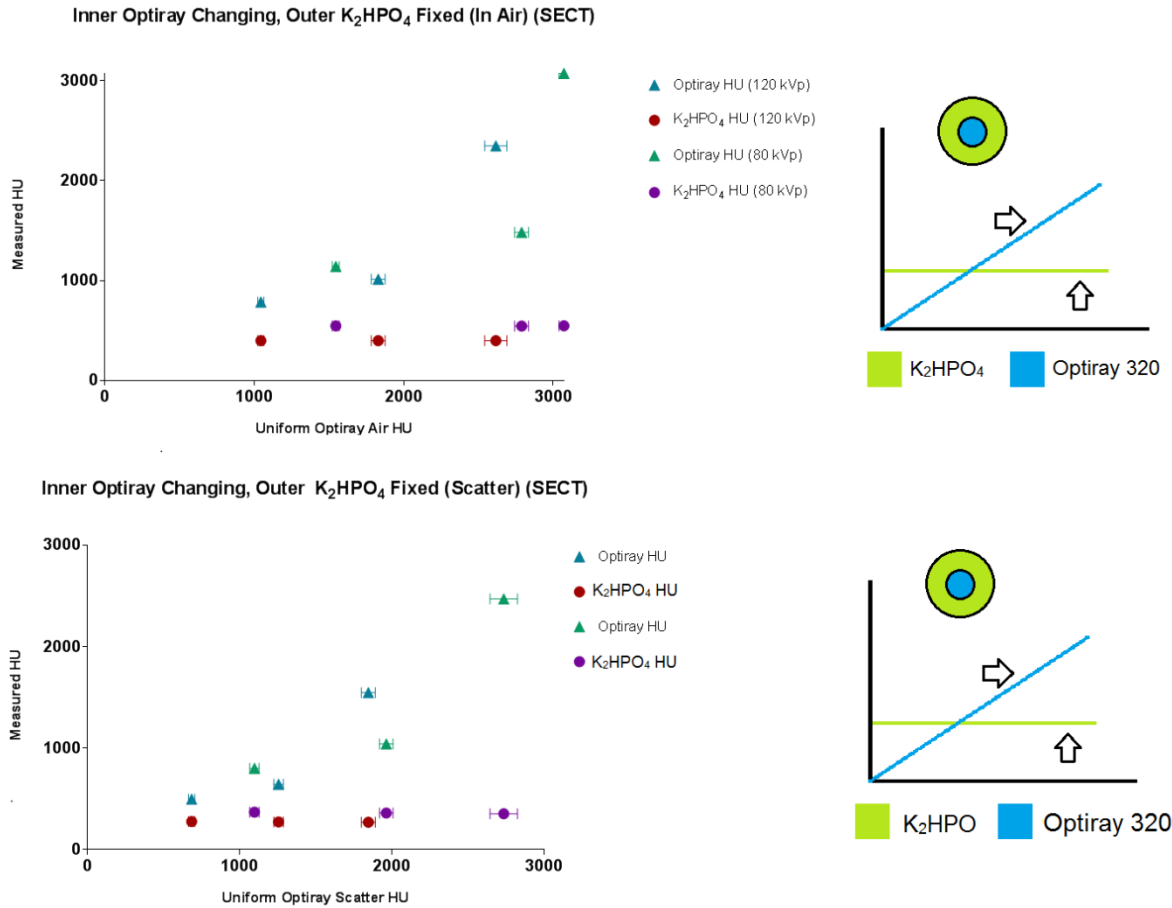


Figure 41: Left: SECT HU measurements in air (Top) and in scatter (Bottom) at 120 and 80 kVp of the inner Optiray 320 solution of increasing concentration, where the outer  $K_2HPO_4$  solution concentration was fixed. Error bars on the x-axis and y-axis indicate the total variation of the uniform solution measurement and the measurement made in the concentric phantom, respectively. The points corresponding to 20% Optiray concentration appears to reflect an improper Optiray solution preparation. Right: Graphic based on Figure 39 illustrating which solution concentration is changing, which solution concentration is fixed and which is being plotted to the left (arrow).

### **3.2.2.3. Discussion**

The increasing concentration and HU measurements of a fixed  $K_2HPO_4$  solution with increasing Optiray 320 concentration disappears when the relative position of the two solutions in the concentric phantoms is reversed and the measurements are instead stable. This indicates that the effect is geometrically dependent rather than an inherent property of the two materials or the scanner. When the position of the Optiray 320 solution and the  $K_2HPO_4$  solution were reversed in the concentric geometry, the effect probably disappeared because many fewer line integrals containing  $K_2HPO_4$  also contained Optiray 320. The Optiray 320 concentration increases as expected.

## **3.3. Subaim 3: Sensitivity of Measurement Methods**

### **3.3.1. Materials and Methods**

It is important for any measurement method used for BMD screening to be sensitive to very small changes in bone density so that the screening is able to detect changes early enough for preventative treatment. To compare the sensitivity of each measurement method, a series of thirteen syringe-phantoms were prepared in 60 mL syringes containing 30 mL  $K_2HPO_4$  solutions with concentrations by volume varying by  $5/2^x\%$ , where  $x = 0 - 12$ . That is, percent concentration successively varied as a half of the previous concentration, 5%, 2.5%, 1.25%, etc. Because the excess volume from the  $K_2HPO_4$  was too small to be evaluated from the syringes, a quadratic regression was fitted to the table provided in Rao et al. (107) of water concentration with increasing  $K_2HPO_4$  concentration. An additional 30 mL syringe-phantom containing pure distilled water (0% concentration) was prepared. Measurements of the  $K_2HPO_4$  solutions were acquired on three separate dates with SECT and DECT in air and in scattering conditions and with DXA as described in Sections 3.1.1.1 and 3.1.2.1 and the three measurements were averaged.

For this experiment, it was necessary to create a new estimate of total variation  $\sigma_t$  for each averaged measurement. Variation in phantom preparation,  $\sigma_p$ , was assumed to be the same value as calculated previously for  $K_2HPO_4$ . Variation between images,  $\sigma_i$ , was estimated from a stack of images obtained of a 2.5%  $K_2HPO_4$  syringe-phantom in air and scattering conditions using the method in section 3.1.1.1 and 3.1.2.1. Variation between scans,  $\sigma_r$ , was the standard deviation of the three-measurement mean. The noise,  $\sigma_n$ , of each measurement was taken as the average standard deviation of the mean for each concentration. The total standard deviation  $\sigma_t$  was obtained by summing the four variabilities in quadrature.

Two different tests assessing the sensitivity of each measurement method were established. In the first test, the difference  $z = a - b$  was considered, where  $a$  is the measurement of a given  $K_2HPO_4$  concentration and  $b$  is the measurement for pure water. The standard deviation of the difference  $z$  is defined by the propagation of error as  $\sigma_z = \sqrt{\sigma_a^2 + \sigma_b^2}$  where  $\sigma_a$  and  $\sigma_b$  are the total standard deviation  $\sigma_t$  for the  $K_2HPO_4$  syringe-phantom and the water syringe-phantom respectively. The concentration of  $K_2HPO_4$  for which  $z > 2\sigma_z$  or  $z > 2\sqrt{\sigma_a^2 + \sigma_b^2}$  is defined as the discrete sensitivity of a given measurement method.

An additional non-discrete sensitivity test was sought to compare the measurement methods within the range of  $K_2HPO_4$  concentration equivalents expected to be measured using SEQCT or DEQCT. In the second test, the  $K_2HPO_4$  concentration, HU, and aBMD measurements in air and scattering conditions from Sections 3.1.1.2 and 3.1.2.2 were combined with the average concentration, HU, and aBMD measurements in this experiment, plotted against the known  $K_2HPO_4$  concentration, and fit with a new regression. Regressions with a y-intercept consistent with 0 within the 95% confidence intervals were re-plotted with the y-intercept set to 0. The smallest detectable change outside the 95% confidence interval in  $K_2HPO_4$  concentration equivalent from those associated with the normal value of a post-

menopausal woman (57,112) was determined for DECT and SECT in air and in scattering conditions and for DXA and this smallest detectable change was defined as the sensitivity. Concentrations of  $K_2HPO_4$  determined to be indistinguishable from water with 95% confidence with a measurement method in the first sensitivity analysis were excluded from this analysis for that measurement method.

### **3.3.2. Results**

#### 3.3.2.1. DECT Sensitivity

The measured concentration of  $K_2HPO_4$  solution with DECT as a function of the concentration (from phantom preparation) used to estimate the sensitivity in the first test is plotted in Figure 42. The smallest detectable  $K_2HPO_4$  concentration from this experiment was 0.16% by volume in air and 2.5% in scattering conditions. The extended  $K_2HPO_4$  concentration plot from the second sensitivity test is shown in Figure 43. The equation for the in-air regression with 95% confidence is  $y = (1.08 \pm 0.02)x$  mg/mL. The normal vBMD of postmenopausal women as assessed with QCT is approximately 126 mg/mL  $K_2HPO_4$  (112), which would according to the fit correspond to a measured concentration of  $(1.08)(126) = 136$  mg/mL. The lower 95% confidence limit on a measurement of 136 mg/mL is  $1.06 \times 126$  mg/mL = 134 mg/mL or  $(134)/1.08 = 124$  mg/mL true  $K_2HPO_4$  concentration. The minimum difference in true  $K_2HPO_4$  concentration from normal that can be detected with 95% confidence is therefore  $126$  mg/mL –  $124$  mg/mL =  $2$  mg/mL or  $2$  mg/mL ÷  $126$  mg/mL = 2%. Likewise, the equation for the regression in scatter is  $y = (0.73 \pm 0.01)x$  mg/mL, so a decrease in normal bone mineral in excess of 2 mg/mL true  $K_2HPO_4$  concentration (2%) is necessary before detection.

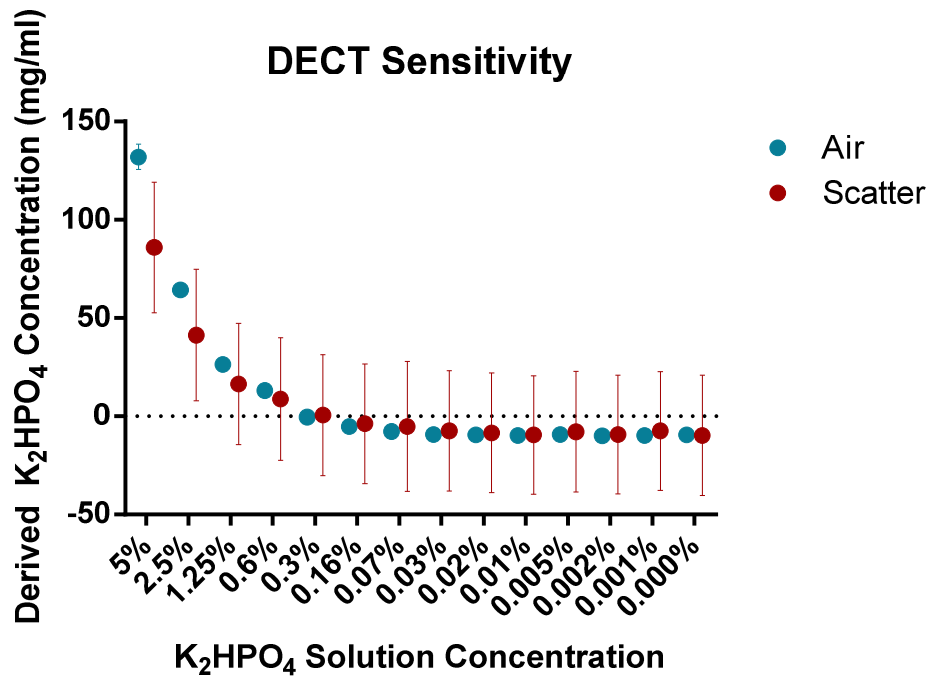


Figure 42: Material density image concentration measured in air and in scattering conditions for a series of K<sub>2</sub>HPO<sub>4</sub> syringe-phantoms for which the concentration of the solute decreases logarithmically. The error bars represent 2σ<sub>z</sub> for that measurement, where z is the difference between the measurement for that K<sub>2</sub>HPO<sub>4</sub> concentration and water. The error bars are too small to be visible for most points in air. The smallest K<sub>2</sub>HPO<sub>4</sub> concentration distinguishable from water in air was 0.16% and 2.5% in scatter.

### Extended $K_2HPO_4$ Measurements (DECT)

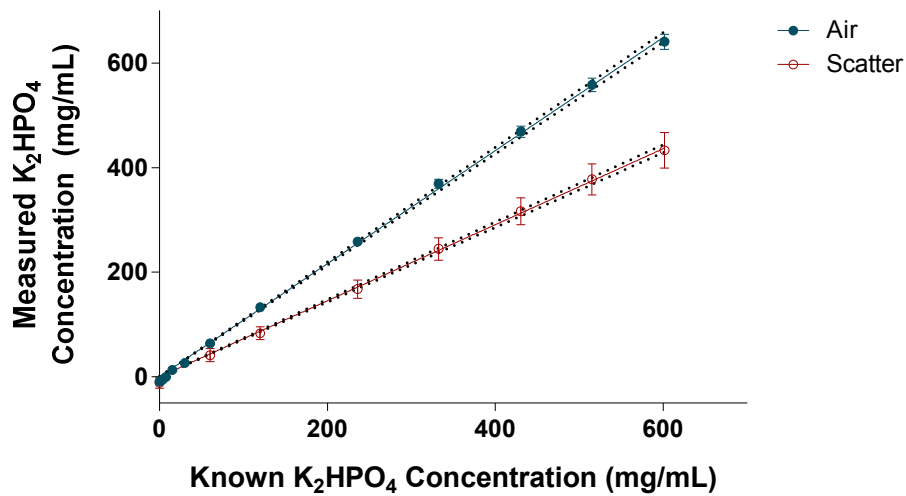


Figure 43: Extended plot of  $K_2HPO_4$  concentration for the purpose of evaluating DECT sensitivity. Error bars on the y-axis indicate total variation for each measurement. The dotted lines indicate the 95% confidence intervals. The equation of the regression in air with 95% confidence is  $y = (1.08 \pm 0.02)x$  (in mg/mL). The equation of the regression in scattering conditions with 95% confidence is  $y = (0.73 \pm 0.01)x$  (in mg/mL).

#### 3.3.2.2. SECT Sensitivity

The measured concentration of  $K_2HPO_4$  solution with SECT as a function of the concentration (from phantom preparation) used to estimate the sensitivity in the first test is plotted in Figure 44. The smallest detectable  $K_2HPO_4$  concentration from this experiment was 0.16% by volume in air and 2.5% in scattering conditions. The 120 and 80 kVp scatter regression from the extended  $K_2HPO_4$  concentration plot in the second sensitivity test (Figure 45) was found to have an offset consistent with zero, so the offset was set to 0 and the slope recalculated with this constraint (shown). The equation for the 120 kVp regression with 95% confidence is  $y = (1.54 \pm 0.04 \text{ HU (mg/mL)}^{-1})x + (19 \pm 11) \text{ HU}$  in air and  $y = (1.12 \pm 0.02 \text{ HU (mg/mL)}^{-1})x$  in scattering conditions. The equation for the 80 kVp regression with 95% confidence is  $y = (2.09 \pm 0.05 \text{ HU (mg/mL)}^{-1})x + (21 \pm 14) \text{ HU}$  in air and  $y =$

$(1.48 \pm 0.03 \text{ HU (mg/mL)}^{-1})x$  in scattering conditions. According to the regression for a 120 kVp HU measurement in air, the normal vBMD of 126 mg/mL  $\text{K}_2\text{HPO}_4$  corresponds to a HU of  $(1.54 \text{ HU (mg/mL)}^{-1})(126 \text{ mg/mL}) + 19 \text{ HU} = 213 \text{ HU}$ . The lower 95% confidence limit on a measurement of 213 HU is  $1.50 \text{ HU (mg/mL)}^{-1} \times 126 \text{ mg/mL} + 8 \text{ HU} = 197 \text{ HU}$  or  $(197 \text{ HU} - 19 \text{ HU}) / (1.54 \text{ HU (mg/mL)}^{-1}) = 116 \text{ mg/mL } \text{K}_2\text{HPO}_4$ . The minimum difference in  $\text{K}_2\text{HPO}_4$  concentration from normal that can be detected with 95% confidence is therefore  $126 \text{ mg/mL} - 116 \text{ mg/mL} = 10 \text{ mg/mL}$  or  $10 \text{ mg/mL} \div 126 \text{ mg/mL} = 8\%$ . Using similar calculations, it was determined that a change of 2 mg/mL (2%) could be detected at 120 kVp in scattering conditions, a change of 10 mg/mL (8%) at 80 kVp in air and in scattering conditions a change of 3 mg/mL (2%).

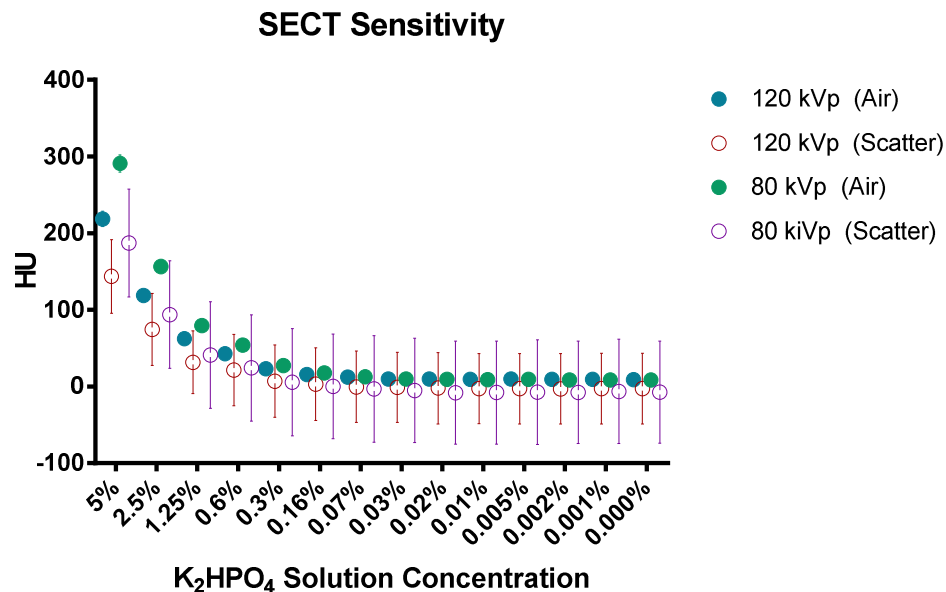


Figure 44: SECT HU measured in air and in scattering conditions at 120 and 80 kVp for a series of  $\text{K}_2\text{HPO}_4$  syringe-phantoms for which the concentration of the solute decreases logarithmically. The error bars represent  $2\sigma_z$  for that measurement, where  $z$  is the difference between the measurement for that  $\text{K}_2\text{HPO}_4$  concentration and water. The error bars are too small to be visible for most points in air. The smallest  $\text{K}_2\text{HPO}_4$  concentration distinguishable from water in air was 0.16% and 2.5% in scatter for both 120 and 80 kVp.

### Extended $K_2HPO_4$ Measurements (SECT)

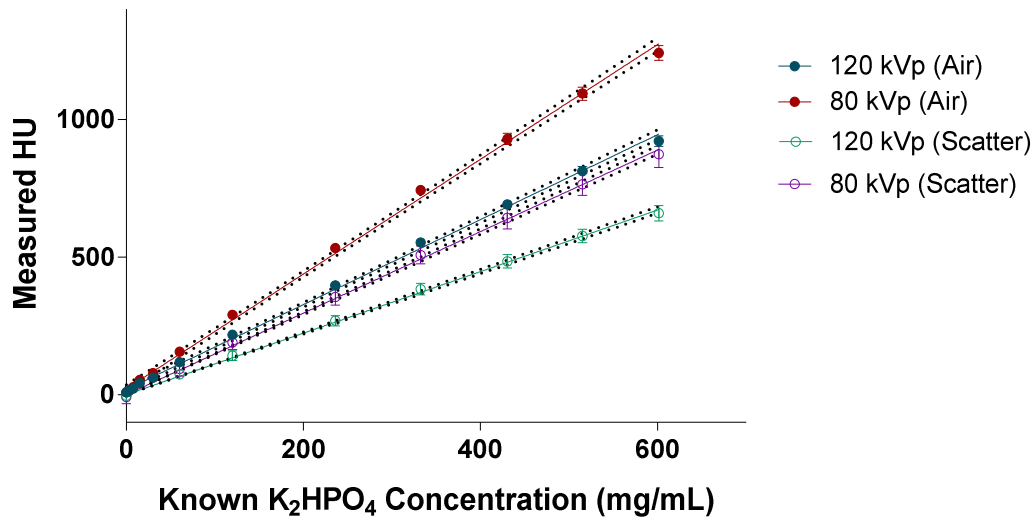


Figure 45: Extended plot of  $K_2HPO_4$  concentration for the purpose of evaluating SECT sensitivity. Error bars on the y-axis indicate total variation for each measurement; some are too small to be visible. The dotted lines indicate the 95% confidence intervals. The equation for the 120 kVp regression with 95% confidence is  $y = (1.54 \pm 0.04 \text{ HU (mg/mL)}^{-1})x + (19 \pm 11) \text{ HU}$  in air and  $y = (1.12 \pm 0.02 \text{ HU (mg/mL)}^{-1})x$  in scattering conditions. The equation for the 80 kVp regression with 95% confidence is  $y = (2.09 \pm 0.05 \text{ HU (mg/mL)}^{-1})x + (21 \pm 14) \text{ HU}$  in air and  $y = (1.48 \pm 0.03 \text{ HU (mg/mL)}^{-1})x$  in scattering conditions.

#### 3.3.2.3. DXA Sensitivity

The measured concentration of  $K_2HPO_4$  solution with DXA as a function of the concentration (from phantom preparation) used to estimate the sensitivity in the first test is plotted in Figure 46. The smallest detectable  $K_2HPO_4$  concentration from this experiment was 0.63 % by volume. The extended  $K_2HPO_4$  aBMD plot from the second sensitivity test is shown in Figure 47. The equation for the regression with 95% confidence is  $y = (2.23 \pm 0.03 \times 10^{-3} \text{ g/cm}^2 \text{ (mg/ml)}^{-1})x - (8 \pm 1 \times 10^{-2}) \text{ g/cm}^2$ . The normal aBMD of postmenopausal women as assessed with DXA is approximately  $0.99 \text{ g/cm}^2$  (57). According to the regression, this corresponds to a  $K_2HPO_4$  concentration of  $x = (0.99 \text{ g/cm}^2 + 0.08 \text{ g/cm}^2) / (2.23 \times 10^{-3}) =$



480 mg/mL. The lower 95% confidence interval of 480 mg/mL is  $(2.20 \times 10^{-3} \times 480 \text{ g/cm}^2 - 9 \times 10^{-2} \text{ g/cm}^2) = 0.97 \text{ g/cm}^2$  or  $(0.97 + 0.08 \text{ g/cm}^2) / (2.23 \times 10^{-3} \text{ g/cm}^2 (\text{mg/ml})^{-1}) = 470 \text{ mg/mL}$   $\text{K}_2\text{HPO}_4$  concentration. The minimum difference in true  $\text{K}_2\text{HPO}_4$  concentration from normal that can be detected with 95% confidence is therefore  $480 \text{ mg/mL} - 470 \text{ mg/mL} = 10 \text{ mg/mL}$  or  $10 \text{ mg/mL} \div 480 \text{ mg/mL} = 2\%$ .

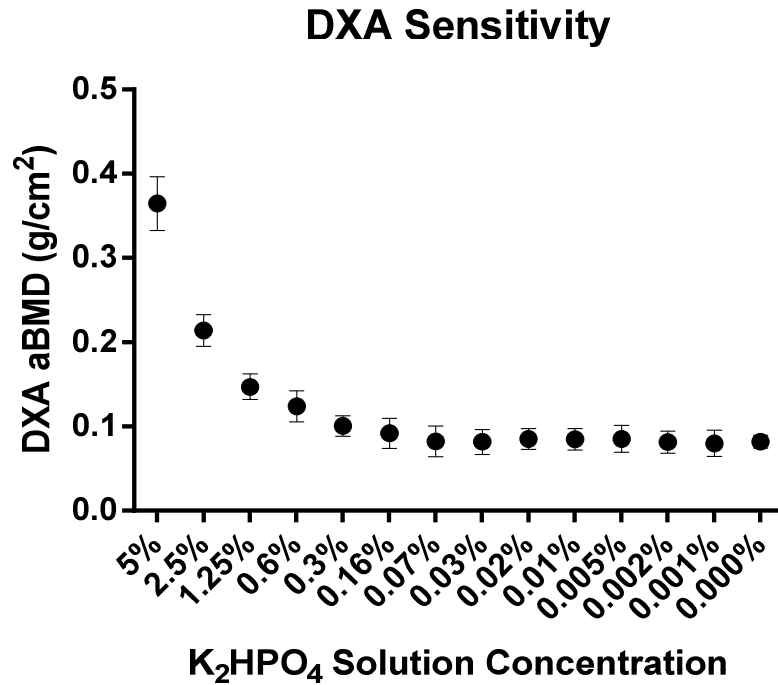
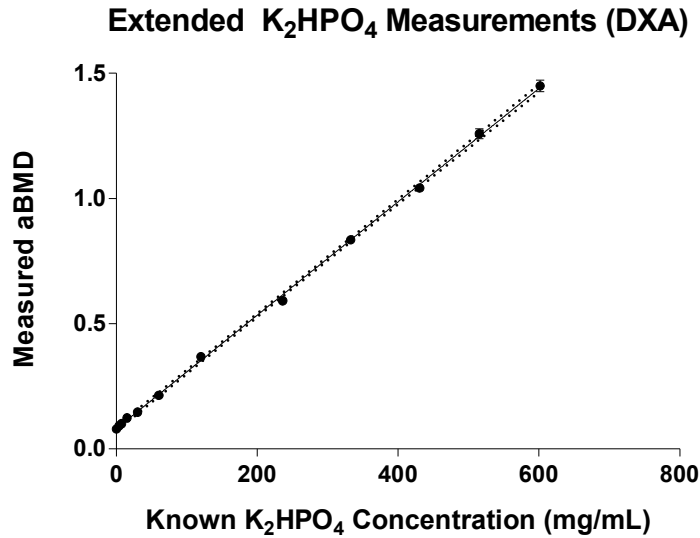


Figure 46: DXA aBMD measured for a series of  $\text{K}_2\text{HPO}_4$  syringe-phantoms for which the concentration of the solute decreases logarithmically. The error bars represent  $2\sigma_z$  for that measurement, where  $z$  is the difference between the measurement for that  $\text{K}_2\text{HPO}_4$  concentration and water. The smallest  $\text{K}_2\text{HPO}_4$  concentration distinguishable from water was 0.31%.

Figure 47: Extended plot of  $K_2HPO_4$  concentration for the purpose of evaluating DXA sensitivity. Error bars on the y-axis indicate total variation for each measurement; most are too small to be visible. The dotted lines indicate the 95% confidence intervals. The equation for the regression with 95% confidence is  $y = (2.23 \pm 0.03 \times 10^{-3} g/cm^2 (mg/ml)^{-1})x - (8 \pm 1 \times 10^{-2} g/cm^2)$ .



The smallest concentration of  $K_2HPO_4$  distinguishable from water in this experiment by each measurement method is summarized in Table 23 along with the magnitude of the different sources of variation for the measurement method at that concentration. Both the 120 kVp and 80 kVp SECT scans were found to detect the smallest concentration of  $K_2HPO_4$ , with DECT in air slightly less sensitive, but both DECT and SECT in scattering conditions were found to be roughly half as sensitive as DXA in distinguishing  $K_2HPO_4$  from water in this experiment.

The smallest detectable change in concentration of  $K_2HPO_4$  from normal in this experiment by each measurement method is summarized in Table 24. DECT in air and scatter was found to be more sensitive than DXA, although only slightly more sensitive than SECT in scattering conditions at 80 and 120 kVp with the techniques used. DXA and SECT at 120 and 80 kVp are equally sensitive in this experiment in terms of the magnitude of  $K_2HPO_4$

concentration detectable, although for DXA measurements this represent a smaller percentage change from normal.

*Table 23: The minimum discrete amount of  $K_2HPO_4$  by volume percentage and concentration that can be distinguished from water by each measurement method in air and in scattering conditions when applicable. The magnitude of each source of variation for that measurement method in the measurement of the listed concentration is also shown for comparison.*

Measurement Method	% $K_2HPO_4$ Solution	$K_2HPO_4$ Concentration (mg/mL)	$\sigma_p$	$\sigma_i$	$\sigma_r$	$\sigma_n$	$\sigma_t$
SECT (120 kVp Air)	0.16%	3.8	0.2 HU	0.2 HU	0.1 HU	2 HU	2 HU
SECT (80 kVp Air)	0.16%	3.8	0.2 HU	0.1 HU	0.4 HU	2 HU	2 HU
DECT (Air)	0.16%	7.6	-0.09 mg/mL	-0.05 mg/mL	0.4 mg/mL	1.3 mg/mL	1.4 mg/mL
DXA	0.31%	7.6	0.004 g/cm <sup>2</sup>	-	0.004 g/cm <sup>2</sup>	-	0.005 g/cm <sup>2</sup>
SECT (120 kVp Scatter)	2.5%	61	2 HU	2 HU	1 HU	17 HU	17 HU
SECT (80 kVp Scatter)	2.5%	61	3 HU	2 HU	1 HU	26 HU	26 HU
DECT (Scatter)	2.5%	61	2 HU	2 HU	2 HU	12 HU	13 HU

Table 24: The smallest detectable reduction in  $K_2HPO_4$  concentration from normal at the 95% confidence interval of the regression as a concentration and percentage of the normal value. The normal  $K_2HPO_4$  concentration equivalent vBMD for post-menopausal women is estimated at 126 mg/mL.

Measurement Method	$K_2HPO_4$ Concentration (mg/mL)	Percentage
DECT (Air)	2	2%
DECT (Scatter)	2	2%
SECT (120 kVp Scatter)	3	2%
SECT (80 kVp Scatter)	3	2%
DXA	10	3%
SECT (120 kVp Air)	10	8%
SECT (80 kVp Air)	10	8%

### 3.3.3. Discussion

The two different experiments for each measurement method gave two different perspectives on its sensitivity. The experiment in which differentiation of  $K_2HPO_4$  from water was the goal highlighted the significant effect of scatter on the variation of SECT and DECT, and it is clear from Table 23 that the increase in total variation  $\sigma_t$  in these measurement methods in scattering conditions, driven by increases in noise, is responsible.

A better understanding of the sensitivity expected in clinical measurements is given by the second experiment, in which the slope of the regression and the uncertainty of the regression parameters determines the modality's sensitivity. DECT was able to detect a smaller change in normal bone  $K_2HPO_4$  concentration in air and in scattering conditions relative to DXA, indicating greater sensitivity (Table 24). Previous research (112) has shown that normal and osteoporotic bone densities for post-menopausal women correspond to  $K_2HPO_4$  concentrations of approximately  $126 \pm 24$  and  $79 \pm 24$  mg/mL, respectively. The smallest detectable change of ~2-3 mg/mL with DECT in air and both DECT and SECT in scattering conditions is well within the standard deviation of the mean value for each population (24 mg/mL). The smallest detectable change of ~10 mg/mL DXA and SECT in scatter found is

likewise sufficient for distinguishing osteoporotic patients from non-osteoporotic patients. Based on our results, in theory a DECT or SECT measurement could detect a change in BMD before DXA.

The rankings of the measurement methods by sensitivity are different for the two experiments. The results from the second experiment indicating DECT measurements in air and both DECT and SECT measurements in scattering conditions are more sensitive than DXA (Table 24) are likely due to the fact that two different equivalent concentrations  $K_2HPO_4$  are being used as the reference. The  $K_2HPO_4$  concentration equivalent of trabecular BMD assessed by SEQCT is much less than the  $K_2HPO_4$  concentration equivalent of the integrated trabecular and cortical BMD that is assessed by DXA. This result then highlights a theoretical advantage of DECT and SECT. The ability to measure BMD specifically for trabecular bone as possible with DECT may further increase its relevance and sensitivity over DXA for detecting a change in normal BMD for postmenopausal women. However, DECT sensitivity may be impacted by the changes in slope from uniform geometry seen in some concentric phantom concentration measurements (Section 3.2.1.2.1).

It is important to remember that both sensitivity and variation determine the usefulness of a measurement method in screening for small changes in BMD. Scatter is present in clinical measurement; therefore, despite the results indicated in Tables 23 and 24, the much reduced total variation of DXA compared to SECT measurements in scattering conditions (0.2% vs 1%) (Table 18) as well as the reduced dose and cost may more than compensate for the very slight reduction in sensitivity and make DXA the preferred modality. It is also important to note that there was no attempt to match the dose of the DECT and SECT techniques, so it is possible that the theoretical sensitivity of SECT could be even greater than that found in these results.

### 3.4. Subaim 4: Correlation of Base Pairs

#### 3.4.1. Materials and Methods

In order to directly compare the performance of DECT concentration with DXA aBMD, a single basis pair for which to evaluate all phantoms is desirable. To assess the correlation between different DECT material decomposition basis pairs, the measurement of the concentration of the solute in the Optiray 320,  $K_2HPO_4$ , and 10 gm%  $K_2HPO_4$  solution uniform syringe-phantoms was made using each of the following basis pairs: Optiray 320-water,  $K_2HPO_4$ -water and 10 gm%  $K_2HPO_4$  solution-ethanol. Identical ROIs were drawn on the constituent basis pair images for each additional basis pair. The concentration of each solute in each basis pair image was plotted against the concentration of the solute measured with the constituent basis pair. The data were fit with a linear regression and their correlations evaluated.

#### 3.4.2. Results

The correlation between the GSI-derived concentration of the constituent solute and the concentration of each other solute was perfectly correlated ( $R^2=1$ ) for each set of syringe-phantoms except for the measured Optiray 320 concentration of the 10 gm%  $K_2HPO_4$  solution syringe-phantoms, which was very highly correlated ( $R^2 > 0.995$ ). The results are summarized in Figures 49-51 and Table 25. It is interesting to note the very high concentrations of 10 gm%  $K_2HPO_4$  solution measured using the of 10 gm%  $K_2HPO_4$  solution-ethanol basis pair for each set of syringe-phantoms relative to the measured concentration of  $K_2HPO_4$ . This is because the concentration of two different solutes is being assessed (pure  $K_2HPO_4$  vs. a solution of  $K_2HPO_4$  in water).

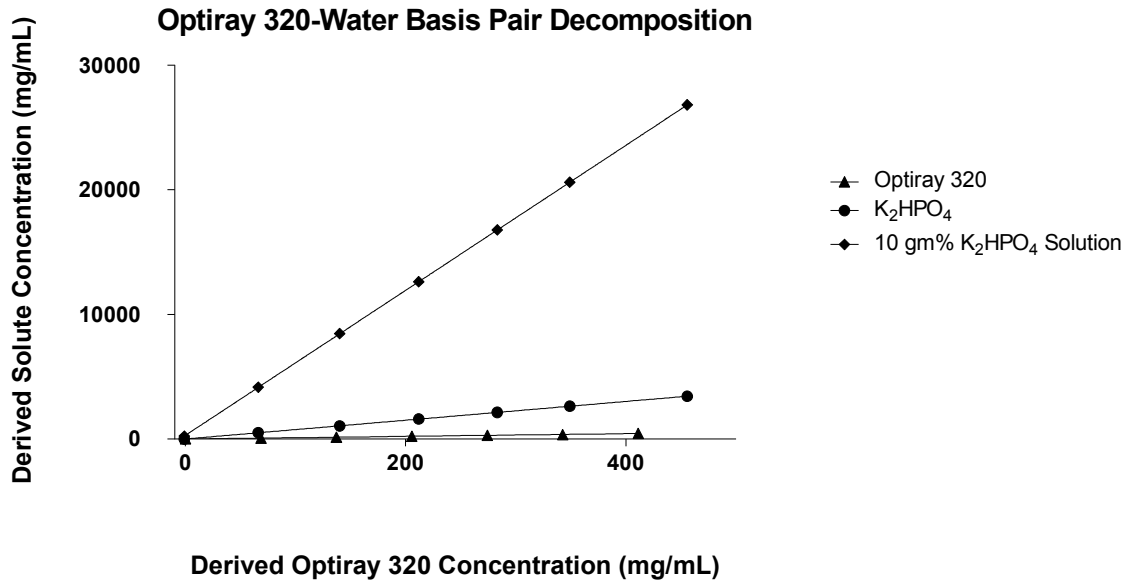


Figure 48: The solute concentrations with different material decomposition basis pairs are measured in the syringe-phantom set containing Optiray 320 and water and plotted against the derived Optiray 320 concentration using the Optiray 320-water basis pair.

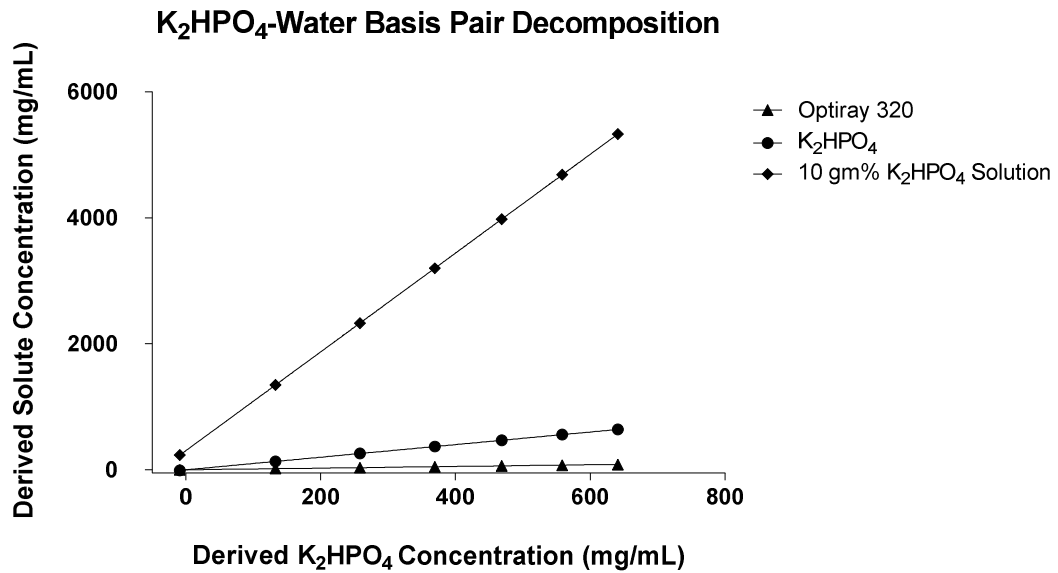


Figure 49: The solute concentrations with different material decomposition basis pairs are measured in the syringe-phantom set containing K<sub>2</sub>HPO<sub>4</sub> and water and plotted against the derived K<sub>2</sub>HPO<sub>4</sub> concentration using the K<sub>2</sub>HPO<sub>4</sub>-water basis pair.

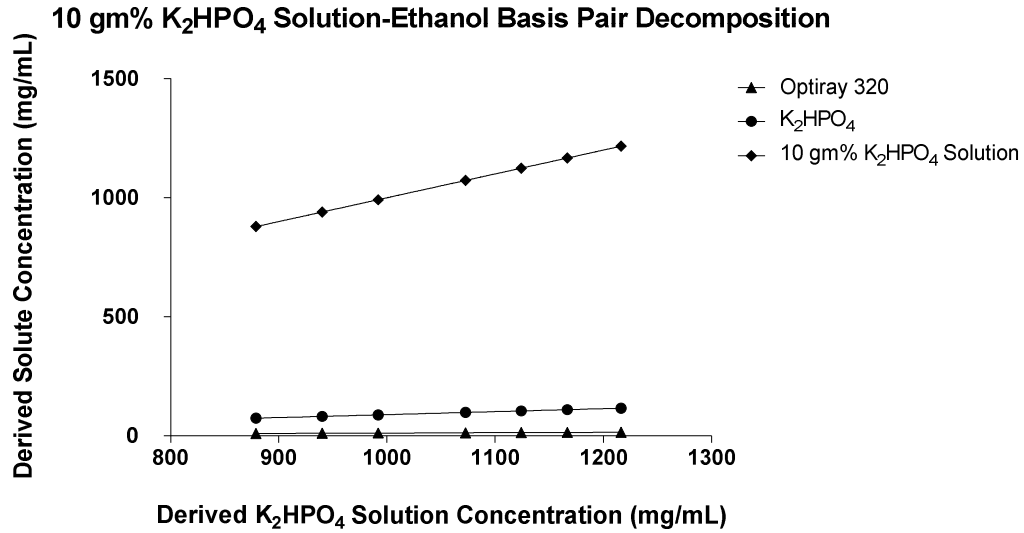


Figure 50: The solute concentrations with different material decomposition basis pairs are measured in the syringe-phantom set containing 10 gm% K<sub>2</sub>HPO<sub>4</sub> solution and ethanol and plotted against the derived concentration of 10 gm% K<sub>2</sub>HPO<sub>4</sub> solution using the 10 gm% K<sub>2</sub>HPO<sub>4</sub> solution-ethanol basis pair.

Table 25: The squared Pearson's correlation coefficient for each linear regression of the derived concentration using a given basis pair against the constituent basis pair for that series of syringe-phantoms.

Base Pair Correlation (R <sup>2</sup> )	Optiray 320 (Derived)	K <sub>2</sub> HPO <sub>4</sub> (Derived)	10 gm% K <sub>2</sub> HPO <sub>4</sub> Solution (Derived)
Optiray 320	1.000	1.000	1.000
K <sub>2</sub> HPO <sub>4</sub>	1.000	1.000	1.000
10 gm% K <sub>2</sub> HPO <sub>4</sub> Solution	0.996	1.000	1.000

### 3.4.3. Discussion

The nearly perfect agreement between all basis pairs is an expected result based on the known principles of material decomposition (113). The lack of perfect agreement for the Optiray 320 basis pair decomposition of the 10 gm% K<sub>2</sub>HPO<sub>4</sub> solution syringe-phantoms was



very likely due to the low concentrations of Optiray 320 measured and the subsequent lack of significant figures. With more significant figures the regression would be expected to be perfect as well. However, the perfect agreement found in this experiment may depend on the mass attenuation coefficient of the two materials in each basis pair being sufficiently different at the effective energies used in DECT. The ethanol-water basis pair is not expected to produce similar results due to difficulties in the material decomposition process, possibly related to the similar mass attenuation coefficients of the two basis materials in the range of rsDECT x-ray energies (Section 3.1.1.3). The advantage of perfect correlation between different basis pairs is the ability to translate density estimates between different materials, as investigated in the next section.

#### **4. Specific Aim II: Relating DECT to DXA**

##### **4.1. Subaim 1: Correlation of DECT and DXA**

###### **4.1.1. Materials and Methods**

To directly compare the performance of DECT and DXA, it is useful to establish if there is a relationship between measurements made by the two methods. To investigate a possible predictable relationship between material density image concentration measurements acquired from DECT and aBMD acquired from DXA,  $K_2HPO_4$  concentrations with the  $K_2HPO_4$ -water basis pair were measured in air for each of the Optiray 320,  $K_2HPO_4$ , and 10 gm%  $K_2HPO_4$  solution uniform syringe-phantoms and plotted with the corresponding DXA aBMD measurements on the ordinate. Here the perfectly linear relationship between each basis pair established in Section 3.4.2 was exploited to combine the measurements of each syringe-phantom on to a single plot using the same basis pair ( $K_2HPO_4$ -water). The data were fit with a linear regression and the degree of correlation was assessed with the Pearson's correlation coefficient.

#### 4.1.2. Results

The correlation between DXA aBMD and  $K_2HPO_4$  concentration for the uniform two-material syringe-phantoms is summarized in Figure 51. The two measurements were highly correlated ( $R^2 > 0.992$ ).

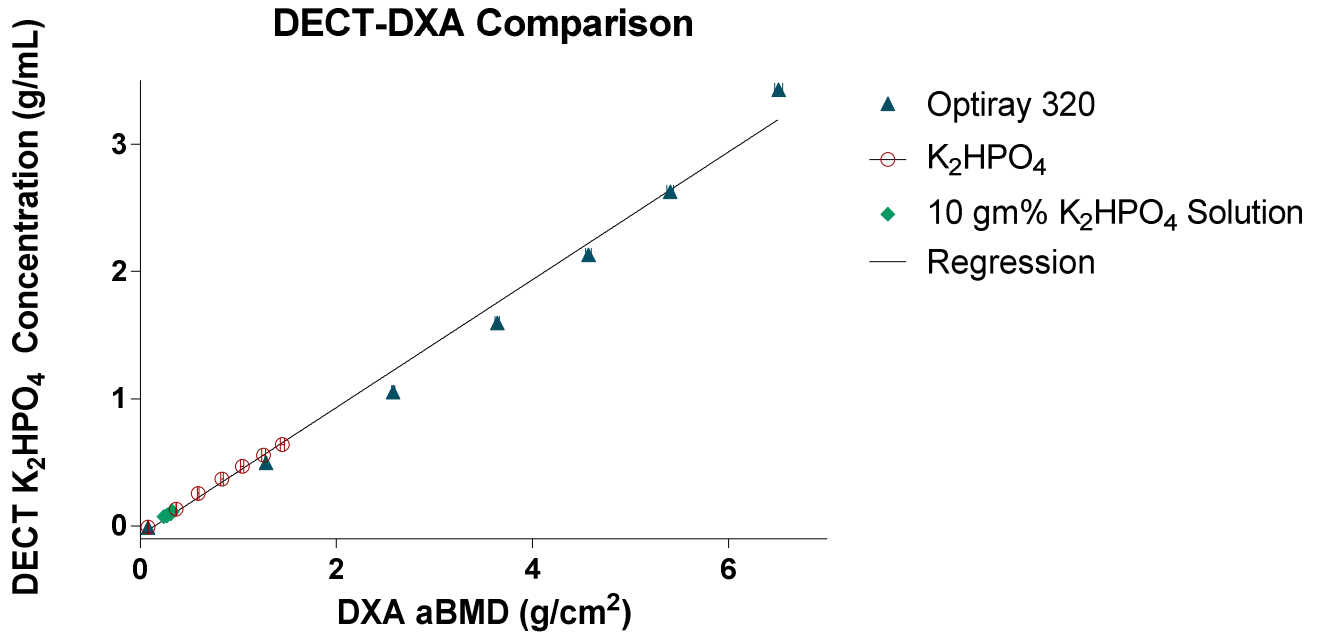


Figure 51: Correlation of  $K_2HPO_4$  concentration measured from material density images using the  $K_2HPO_4$ -water basis pair for three different solutes with aBMD measured with DXA.

#### 4.1.3. Discussion

Figure 51 is very interesting because it suggests that concentration measurements acquired with DECT in air are linearly correlated with DXA aBMD measurements, despite the two measurement methods assessing composition using two very different methodologies. Due to the perfectly linear relationship between different material density image basis pairs, a similar linear regression with the exact same Pearson's correlation coefficient could be found for DXA aBMD and nearly any other material, provided there was sufficient difference between the mass attenuation coefficients of the two material bases in the appropriate energy range. While the relationship is geometrically dependent due to the DXA's areal density

measurements, a linear relationship between the two modalities suggests that it may indeed be possible to relate a DECT measurement to an aBMD measurement of a given sample.

## **4.2. Subaim 2: DECT Integration and DXA Comparison**

### **4.2.1. Materials and Methods**

To evaluate the ability of material density image concentration measurement to predict DXA aBMD, 34 DECT, SECT, and DXA image sets were obtained, consisting of three uniform syringe-phantoms of each solute composition (Optiray 320,  $K_2HPO_4$ , 10 gm%  $K_2HPO_4$  solution) plus one 2.5%  $K_2HPO_4$  syringe-phantom, three phantoms from each set of concentric phantoms, including the shared (10% inner  $K_2HPO_4$ /10% outer Optiray 320) phantom, the QC phantom included with the Hologic Discovery DXA scanner (Figure 52), the European Spine Phantom (Figure 53), and nine animal bones as unknown, arbitrary anthropomorphic samples. The European Spine Phantom (114) (Quality Assurance and Radiology in Medicine, Möhrendorf, Germany) is a tool designed to relate CT and DXA measurements consisting of three lumbar spine inserts designed to provide a clinical range of three different bone mineral (HA) densities. The animal bones were of bovine or porcine origin obtained in a raw condition from a grocery store (neck bones) or in cured form from a pet clinic (all others). They included a shank, a collection of five neck bones, a femoral head, and a set of two vertebral bodies (Figure 54).

The image sets were obtained from the DECT scanner using the GSI-6 DECT protocol (Table 11) with 5 mm images and at 80 kVp/200 mA with a 1s tube rotation time and medium body filter selected. 80 kVp was selected instead of 120 due to the increased sensitivity to material composition. 2.5 mm images for the femoral head and one positioning of the vertebral bodies were obtained at 80 kVp.

The animal bones were also scanned in the DXA scanner between PMMA blocks as used for the liquid solution phantoms (Figure 55). The vertebral bodies were oriented in two

different positions in the DECT and DXA scanners, in order to present different areas for aBMD measurements. Instead of manual ROIs, the DXA software automatically identified bone material and corresponding ROIs for which the aBMD was determined for the QC phantom, animal bones, and ESP. Because the DXA aBMD measurements of the QC phantom and ESP relied on user delineation of the individual vertebral bodies, three scans were acquired and the measurements were averaged.

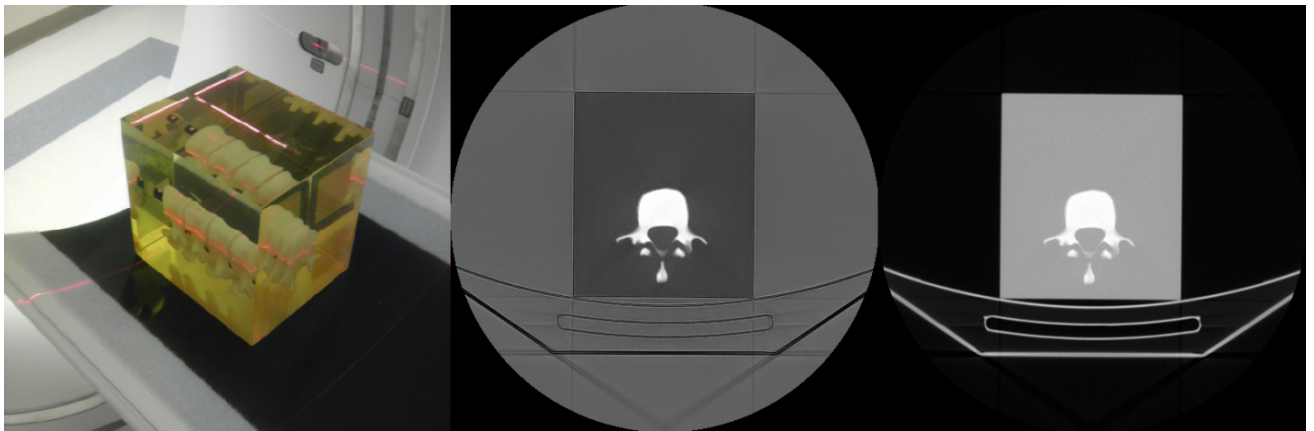


Figure 52: Left: Anthropomorphic QC phantom included with the Hologic Discovery DXA scanner. The cuboid phantom is designed to produce a measured aBMD of about  $1 \text{ g/cm}^2$  on the scanner. Center: DECT  $K_2HPO_4$  material density map. Right: SECT 80 kVp HU image.



Figure 53: Left: The European Spine Phantom. Center: DECT  $K_2HPO_4$  material density map. Right: SECT 80 kVp HU image.

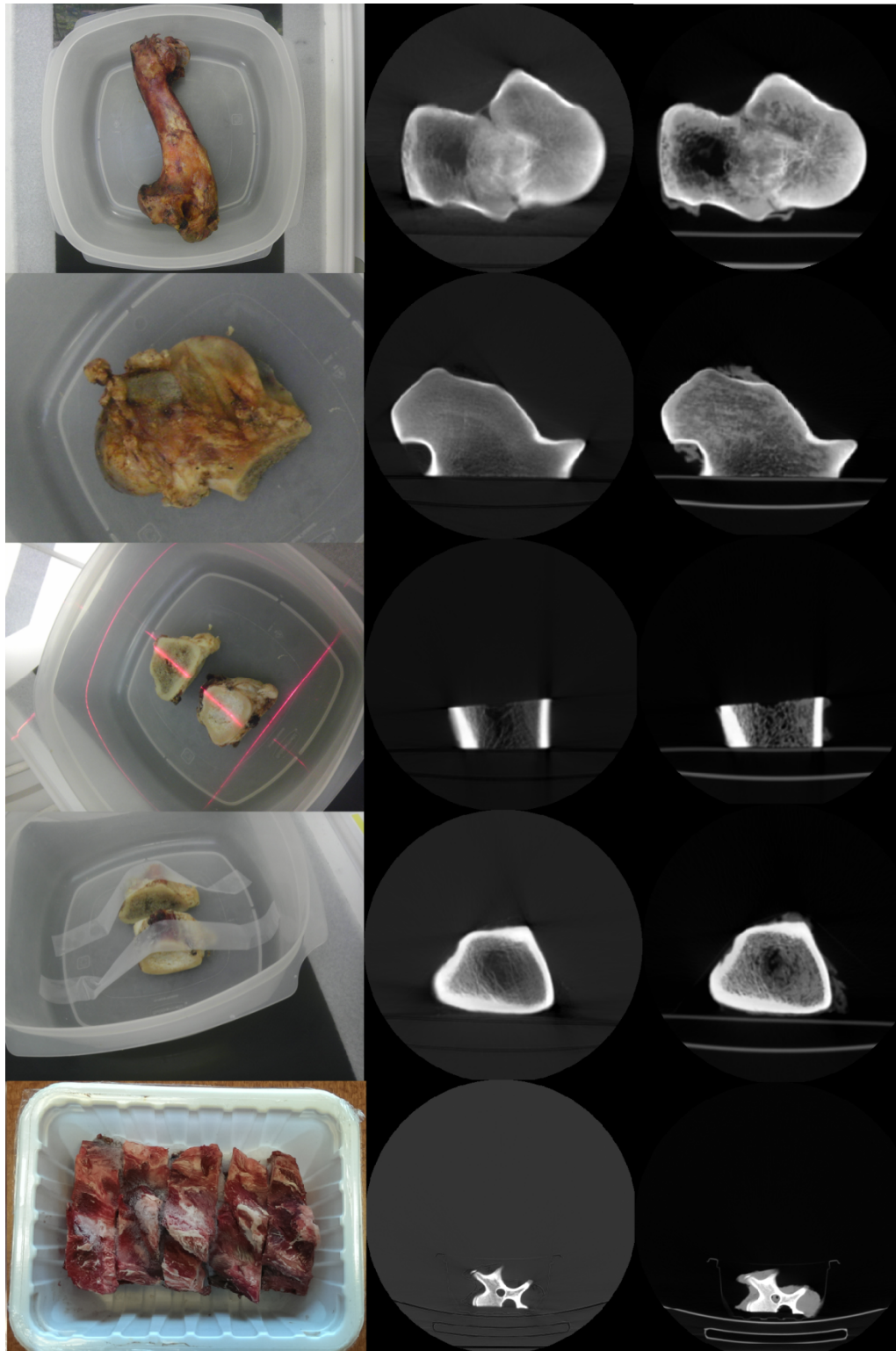
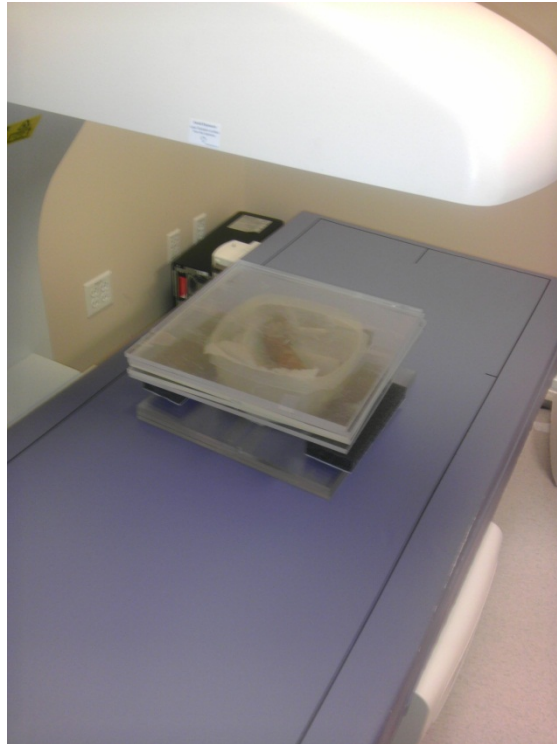


Figure 54: Top to bottom: Shank, femoral head, vertebral bodies placed parallel to scan axis, vertebral bodies placed perpendicular to scan axis, neck bones. Left to right: photograph, DECT  $K_2HPO_4$  material density map, SECT 80 kVp HU image.

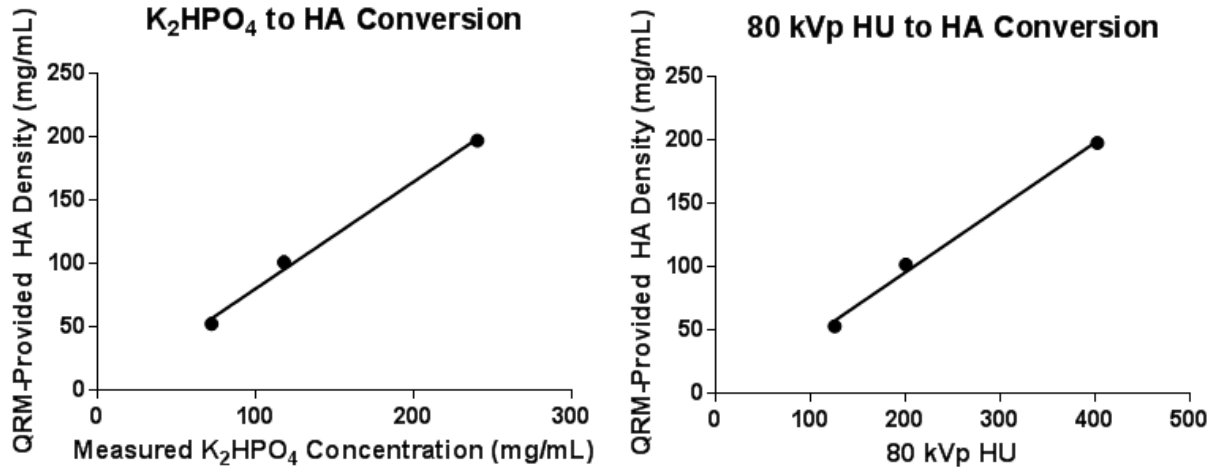


Figure 55: Arrangement of materials for measurement of animal bones with the DXA scanner.



A methodology for processing and analyzing DECT and SECT data to produce an areal BMD in  $\text{g}/\text{cm}^2$  was devised to fully evaluate the relationship between DXA aBMD and material density image concentration measurements, as well as SECT HU measurements for comparison. To assist the comparison, the European Spine Phantom was scanned using the GSI-6 protocol (Table 11). The DECT and SECT scans of the European Spine Phantom were used to convert the raw  $\text{K}_2\text{HPO}_4$  density and 80 kVp HU of each of the phantom's three vertebral bodies to the true HA density provided by the manufacturer using a linear transformation function estimated by fitting the data (Figure 56).

Figure 56: Linear regression used to convert material density image-derived  $K_2HPO_4$  concentration (left) and 80 kVp HU (right) to HA concentration using HA density provided by QRM. The equation of the line for DECT  $K_2HPO_4$  measurements is  $y = 0.8445x - 3.536$  (in (mg/mL)/(mg/mL)). The equation of the line for SECT 80 kVp HU measurements is  $y = 0.5125x$  (in (mg/mL)/HU) - 6.800 (in mg/mL).



A diagram of the CT image integration process is illustrated in Figure 57. Axial image stacks of the DECT material density map with the  $K_2HPO_4$ -water basis pair and the SECT HU map transformed into HA density were re-binned, avoiding interpolation, into coronal-plane images using ImageJ image analysis software (115). A threshold for “bone material” in the stack was visually determined and voxels below the threshold in each image were set to 0 mg/mL. The images in each stack were arithmetically summed into a single image, on which a new threshold was applied to segment the “bone” or a manual ROI corresponding to the DXA ROI was placed. A measurement of the integrated density  $N$ , or the sum of the value of each selected pixel in mg/mL HA, and the total area  $A$  of the selected pixels in  $mm^2$  was calculated for each summed image after segmentation. The estimate of aBMD in HA density, expressed in  $g/cm^2$  based on DECT and SECT data was then calculated as follows:

$$aBMD \left[ \frac{g}{cm^2} \right] = \left( NV \times \frac{1000^{-1} g}{mg} \right) / \left( A \times \frac{10^{-2} cm^2}{mm^2} \right), \quad \text{Equation 4.2.1-1}$$

where  $N$  is the integrated density in units of  $\text{mg}/\text{cm}^3$  HA,  $V$  is the voxel volume in  $\text{mL}^3$ , and  $A$  is the total area of the selected pixels on the integrated DECT or SECT image.

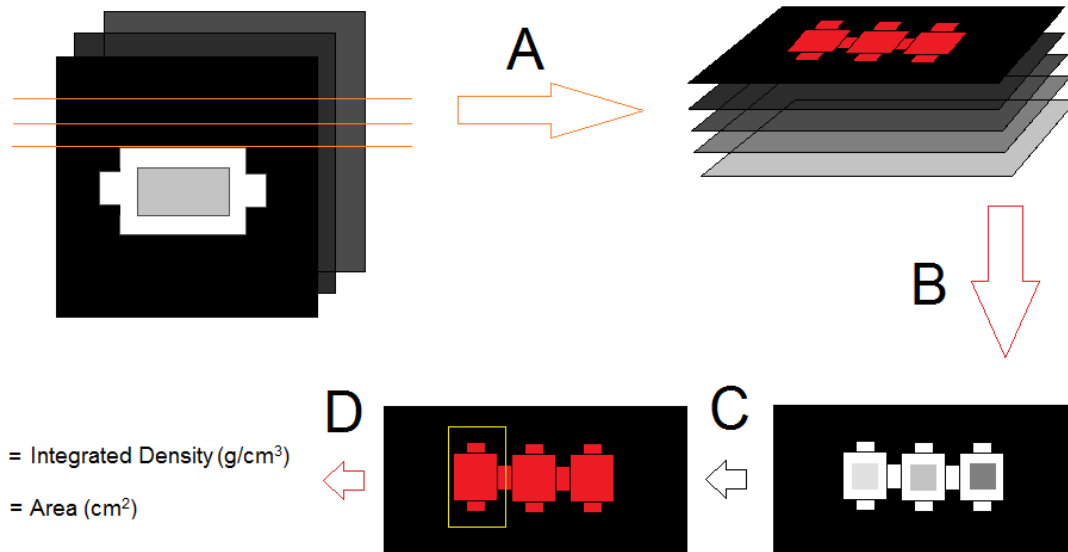


Figure 57: Simplified schematic diagram of the DECT or SECT image integration process for the ESP. A) An axial image set is re-binned into coronal images. A threshold is applied and the remaining voxels are set to zero B) The thresholded images are then integrated into a single image. C) A new threshold is applied and D) the resulting area (within an ROI in this case) is recorded along with the integrated density from which to calculate the aBMD (right).



The integration processing described was applied to the 34 DECT image sets. The 80 kVp SECT images were processed in the same manner for comparison with a similar HA conversion (Figure 56) applied, excluding three phantoms in which a large number of pixels attained the maximum CT number (25% Optiray 320 uniform syringe-phantom, 10%/30% concentric phantom, and shank). The HA aBMD ( $\text{g}/\text{cm}^2$ ) for DECT and SECT were plotted with DXA aBMD measurements on the ordinate and the data were fit with a linear regression. Correlation was assessed using Pearson's correlation coefficient and a slope and offset calculated with 95% confidence. The DECT and SECT HA aBMD were compared with DXA aBMD with Bland-Altman analysis.

#### **4.2.2. Results**

##### 4.2.2.1. DECT Integration

The measurements of aBMD between the two modalities were found to be correlated ( $R^2 = 0.983$ ,  $p < 0.0001$ ), and the regression (Figure 58) is  $y = (0.95 \pm 0.04)x$  (in  $\text{g}/\text{cm}^2$ ) / ( $\text{g}/\text{cm}^2$ ) +  $(0.28 \pm 0.09)$  (in  $\text{g}/\text{cm}^2$ ). The range of DXA aBMD values expected to be seen in clinical measurements of the lumbar spine, about  $0.65\text{-}1.5 \text{ g}/\text{cm}^2$  (53) is shown in more detail in Figure 59. The Bland-Altman analysis, (Figure 60, Table 26) yielded a mean difference of  $0.205 \text{ g}/\text{cm}^2$  with a standard error of  $0.005 \text{ g}/\text{cm}^2$ , indicating a consistent underestimation of DXA aBMD by DECT aBMD. The 95% confidence interval for the limits of agreement between DXA and material density image-derived aBMD were calculated to be  $-0.16\text{--}0.57 \text{ g}/\text{cm}^2$ . In the clinical range, Bland-Altman analysis yielded a mean difference of  $0.27 \text{ g}/\text{cm}^2$  with a standard error of  $0.01 \text{ g}/\text{cm}^2$ , and a 95% confidence interval for the limits of agreement of  $-0.05\text{--}0.60 \text{ g}/\text{cm}^2$ .

## DXA aBMD Prediction from DECT aBMD

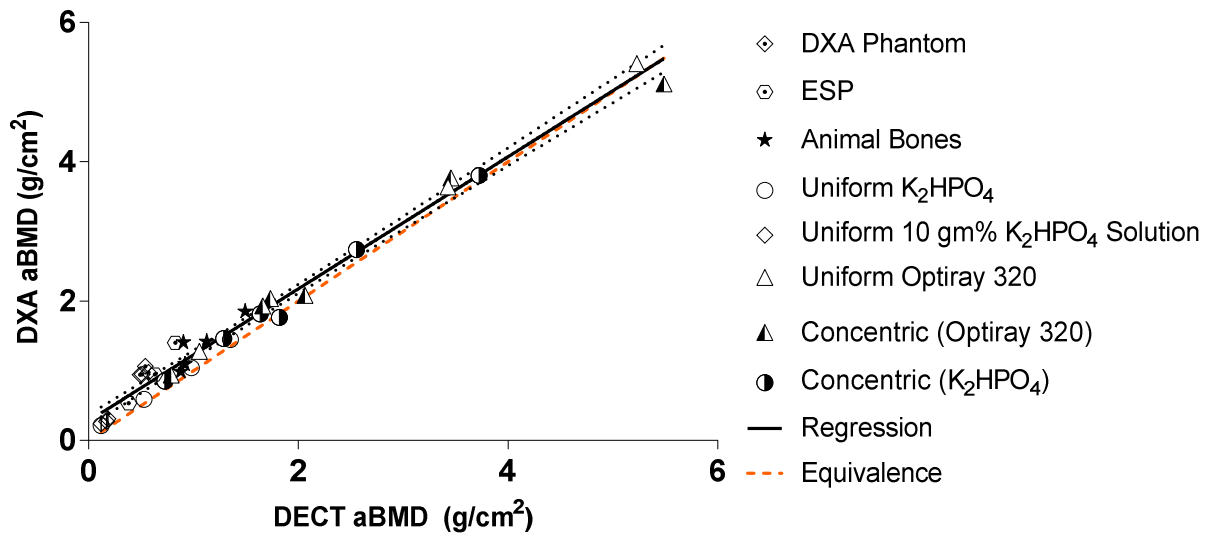


Figure 58: Correlation of integrated HA aBMD acquired from DECT images and DXA aBMD.

The linear regression is plotted with 95% confidence intervals (dotted lines) and the line of equivalence. The equation of the regression is  $y = (0.95 \pm 0.04)x$  (in  $(g/cm^2)/(g/cm^2)$ ) +  $(0.28 \pm 0.09)$  (in  $g/cm^2$ ).

## DXA aBMD Prediction from DECT aBMD (Clinical Range)

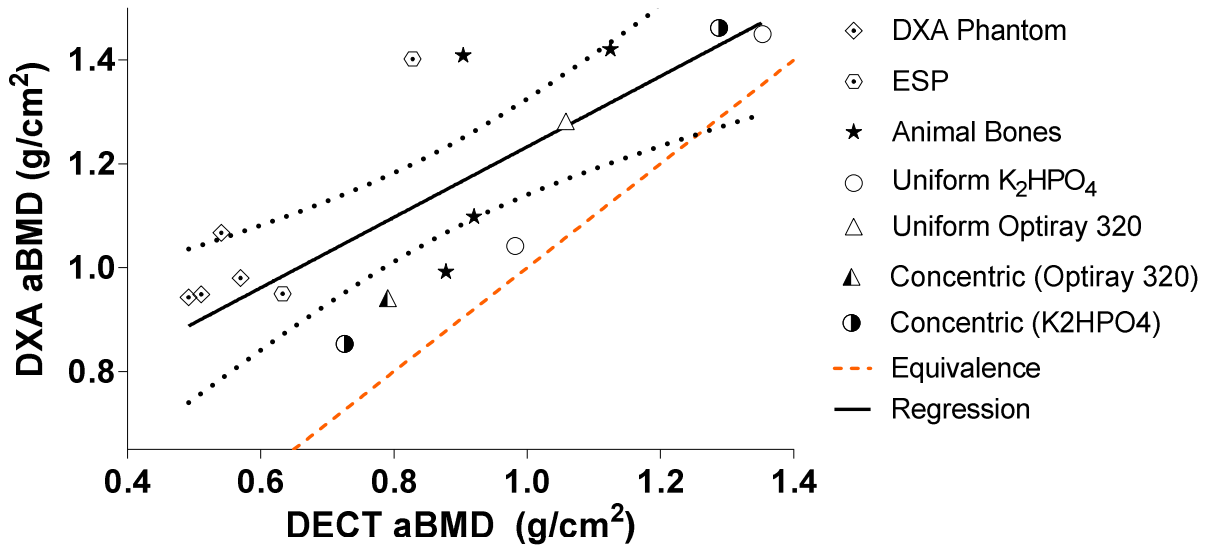


Figure 59: Enlargement of Figure 58 showing the range of DXA aBMD values expected to be seen in clinical measurements of the lumbar spine, about 0.65-1.5 g/cm<sup>2</sup>. Dotted lines represent the 95% confidence intervals and the line of equivalence is shown for reference.

Figure 60: Bland-Altman analysis comparing DECT aBMD and DXA aBMD of a variety of phantoms illustrated in Figure 58. The mean difference was 0.205 g/cm<sup>2</sup> with a standard error of 0.005 g/cm<sup>2</sup>.

### Difference vs. average: Bland-Altman of DECT aBMD

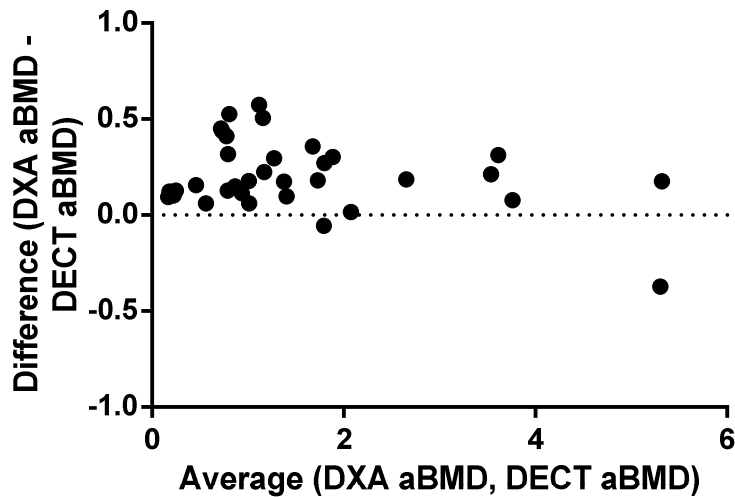


Table 26: Bland-Altman statistics of comparison between DECT HA aBMD and DXA aBMD.

Bias (g/cm <sup>2</sup> )	Standard Deviation of Bias (g/cm <sup>2</sup> )	Upper Limit of Agreement (95%)	Lower Limit of Agreement (95%)
0.21	0.18	0.57	-0.16

#### 4.2.2.2. SECT Integration

The correlation for SECT integration measurements is nearly as high ( $R^2 = 0.968$ ) as for DECT (Figures 62-63). The regression was found to have a y-intercept consistent with 0 within the 95% confidence intervals ( $0.05 \pm 0.1$ ) and so was re-plotted with the y-intercept set to 0. The regression, with 95% confidence intervals, is  $y = (1.25 \pm 0.5)x$  (in (g/cm<sup>2</sup>)/(g/cm<sup>2</sup>)). The Bland-Altman analysis (Figure 63, Table 27) yielded a mean difference of -0.276 g/cm<sup>2</sup> with a standard error of 0.008 g/cm<sup>2</sup>, indicating a consistent underestimation of DXA aBMD by SECT aBMD. The 95% confidence interval for the limits of agreement between DXA and SECT-

derived aBMD were calculated to be  $-0.17$ — $0.72$   $\text{g}/\text{cm}^2$ . In the clinical range, Bland-Altman analysis yielded a mean difference of  $0.24$   $\text{g}/\text{cm}^2$  with a standard error of  $0.01$   $\text{g}/\text{cm}^2$ , and a 95% confidence interval for the limits of agreement of  $-0.10$ — $0.58$   $\text{g}/\text{cm}^2$ .

### DXA aBMD Prediction from SECT aBMD

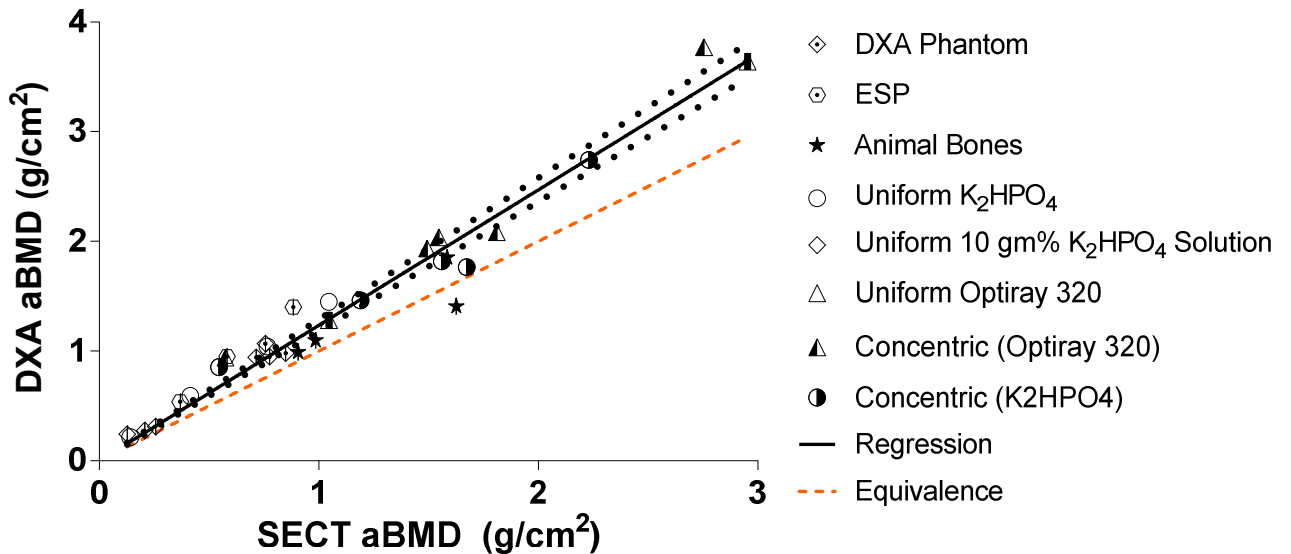


Figure 61: Correlation of integrated 80 kVp HU areal density acquired from SECT images and DXA aBMD. The linear regression is plotted with 95% confidence intervals, represented as dotted lines. The equation of the regression is  $y = (1.25 \pm 0.5)x$  (in  $(\text{g}/\text{cm}^2)/(\text{g}/\text{cm}^2)$ ). The line of equivalence is shown for comparison.

## DXA aBMD Prediction from SECT aBMD (Clinical Range)

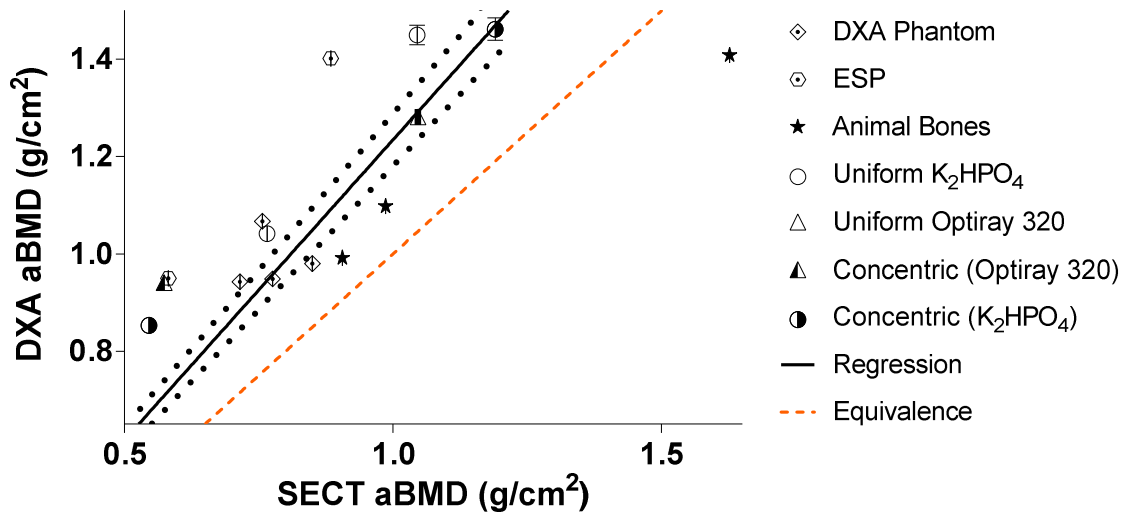


Figure 62: Enlargement of Figure 61 showing the range of DXA aBMD values expected to be seen in clinical measurements of the lumbar spine, about 0.65-1.5 g/cm<sup>2</sup>. Dotted lines represent the 95% confidence intervals of the regression. The line of equivalence is shown for comparison.

### Difference vs. average: Bland-Altman of SECT aBMD

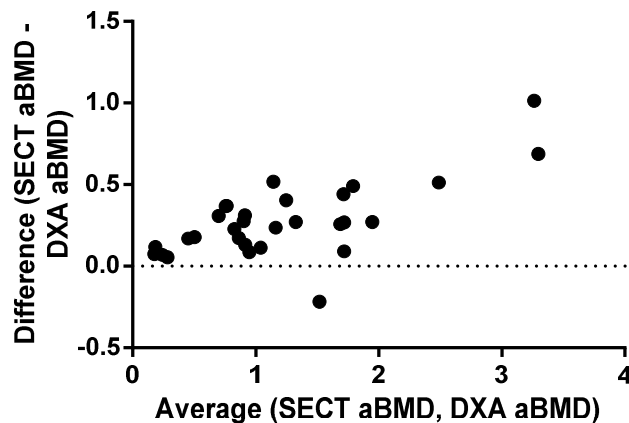


Figure 63: Bland-Altman analysis comparing SECT aBMD and DXA aBMD of a variety of phantoms illustrated in Figure 61. The mean difference was -0.276 g/cm<sup>2</sup> with a standard error of 0.008 g/cm<sup>2</sup>.

Table 27: Bland-Altman statistics of comparison between SECT HA aBMD and DXA aBMD.

Bias (g/cm <sup>2</sup> )	Standard Deviation of Bias (g/cm <sup>2</sup> )	Upper Limit of Agreement (95%)	Lower Limit of Agreement (95%)
0.21	0.21	0.14	-0.70

#### 4.2.3. Discussion

We have taken a three-dimensional imaging modality and created a two-dimensional image for the purpose of comparing its performance to a two-dimensional modality. aBMD measurements in g/cm<sup>2</sup> from DECT integration are well-correlated with aBMD in g/cm<sup>2</sup> measured with DXA. The slope (near unity,  $0.95 \pm 0.04$ ) of the linear regression to the DECT HA areal density plot lends credibility to the DECT integration methodology and suggests the two measurement methods are indeed assessing the same fundamental quantity, the total volumetric density of bone mineral. However, the 95% upper and lower limits of agreement of the DXA aBMD (-0.16-0.57 g/cm<sup>2</sup>) are of the same magnitude as a change in DXA aBMD from normal to osteoporotic (about 0.3 g/cm<sup>2</sup>) (53), limiting the utility of a conversion between the two measurements.

SECT integration measurements are also very well-correlated ( $R^2 = 0.968$ ) with DXA aBMD. However, the trend of SECT integration measurements is an increasing distance from the line of equivalence with increasing SECT aBMD (Figure 62). The limits of agreement for SECT aBMD measurements with DXA aBMD measurements are not an improvement over those for DECT (Table 27).

The aBMDs from DECT and SECT in this experiment were both calculated from images acquired in air. Based on results obtained in Sections 3.1. and 3.2, the effect of surrounding tissue may further complicate the observed linear relationship of each with DXA aBMD in clinical imaging. There is some uncertainty introduced in the manual identification of bone material and the re-binning process used. Additionally, the reconstruction does not exactly

match the fan-beam reconstruction used in DXA imaging. Finally, the difference in the calculation and application of the pixel-by-pixel HA density in the dual-energy processing of DECT and DXA (DECT used a correction based on known HA densities, while DXA used an empirical correction based on the “soft tissue” composition) may have affected our results. All of these factors should be considered in any future applications of this method.

## 5. Conclusion

We have shown that the rsDECT measurements of material concentration obtained with material density images have an RMS accuracy error greater than 5% in air. Accuracy is further reduced under scattering (clinical) conditions (~8-27%), and to a lesser extent with different GSI protocols and patient positioning (< 5%). The accuracy of material density image concentration measurements is also impacted by the attenuation geometry of bone, where a lower-attenuating material of interest is surrounded by a more highly attenuating material. The denser the higher-attenuating material, the higher the measured concentration of the inner material tends to be. These effects, (excepting the effects of DECT protocol), are all observed in SECT data well, suggesting that the dual-energy reconstruction algorithm is not fully compensating for effects inherent in the single-energy data used in the reconstruction. It is important to emphasize that the processing of the dual-energy images in the material density images is only theoretically understood; the details of the implementation, including the reconstructions of the integrated signals (e.g. if it is a linear or higher order function (9,113,116)) and ways in which single-energy inaccuracies could perpetuate to dual-energy data, is unknown.

Based on our assessment of sensitivity, DECT measurements in scattering conditions are marginally more sensitive than DXA to a change in BMD from normal for postmenopausal women (~1 mg/mL  $K_2HPO_4$ ) based on the 95% confidence limits of a regression fitted to  $K_2HPO_4$  syringe-phantom measurements. While this is a promising result, the advantage of the



minor increase in sensitivity is undercut by the inaccuracies in the absolute concentration measurements as well as higher dose (in this study, the  $CTDI_{vol}$  of DECT with GSI-6 protocol was 33.43 mGy, compared with 12.46 mGy and 5.59 mGy at 120 and 80 kVp, respectively, and 0.020 mGy max for the DXA exam). Because Bland-Altman analysis demonstrates that DECT aBMD integration is not sufficiently accurate to reliably produce a DXA aBMD (measurements are expected to differ from DXA aBMD by anywhere from  $-0.16$ - $0.57$  g/cm<sup>2</sup> compared to a change in aBMD of about 0.3 g/cm<sup>2</sup> expected between normal and osteoporotic bone) and is also comparable to SECT aBMD integration ( $-0.72$ - $0.17$  g/cm<sup>2</sup>), the overall advantage of DECT over SECT for assessing BMD based on this study is not clear. DECT material density images would require detailed corrections to produce concentration measurements with clinically acceptable accuracy.

## 6. Future Work

Our study was limited to comparing a single DECT vendor and implementation to a single DXA device. Although we were able to partially evaluate the rsDECT technique in the HD750 scanner, the performance of an alternative commercial DECT implementation such as dual-source DECT in characterizing BMD is unknown. While in our study the Hologic Discovery is assumed to have comparable performance to other currently used DXA scanners, the rsDECT has not yet been compared to any other device.

Only a few material basis pairs were assessed for accuracy, at least one of which, ethanol-water, being inappropriate for general use. There could be many other material basis pairs as problematic as ethanol-water. A wider range of materials evaluated with GSI dual-energy imaging could provide a more comprehensive picture of the technology, particularly clinically relevant materials such as iron (Fe).

While the effect of a few different imaging parameters on material density image concentration measurements were assessed, there are many known sources of variation in

QCT that can be expected affect quantitative measurements (6,72,85). For example, there are many more GSI protocols, with many different associated imaging parameters, which have unknown effects on material density measurements. A detailed investigation of the effects of these parameters would greatly clarify the possible utility of DECT concentration measurements.

A more sophisticated calibration of our  $K_2HPO_4$  concentration measurements to HA density may have allowed for a better comparison to DXA aBMD. This could have been accomplished with a greater number solid phantoms consisting of varying concentrations of HA in water-equivalent plastic. A programmed basis pair of HA-water may also have been evaluated. These calibration methods can be explored in future studies.

Finally, additional insight may be gained by performing material density image measurements in real human vertebral bones, either from cadavers or in patient studies. Vertebral specimens from cadavers with intact marrow fat would be especially good for this investigation, so that the effect of real fat and bone on DECT concentration measurements could be assessed. Alternatively, patient images with both rsDECT and DXA could be obtained either in a prospective or retrospective study. Such a study would include patients of different genders, ethnicities, and age groups to benchmark DECT values against those from DXA, ideally comparing the change in BMD measured between the two modalities over time. In addition, the clinical value of separate cortical and trabecular measurements of BMD with rsDECT could be investigated.

## 7. Bibliography

1. Kanis JA, Melton LJ, Christiansen C, Johnston CC, Khaltsev N. The diagnosis of osteoporosis. *J Bone Miner Res.* 1994;9(8):1137–41.
2. Kanis JA. Assessment of fracture risk and its application to screening for postmenopausal osteoporosis: Synopsis of a WHO report. *Osteoporosis Int.* 1994 Nov 1;4(6):368–81.
3. World Health Organization. Prevention and Management of Osteoporosis - Report of a WHO Scientific Group. WHO; 2003.
4. Li B, Aspden RM. Composition and mechanical properties of cancellous bone from the femoral head of patients with osteoporosis or osteoarthritis. *J Bone Miner Res.* 1997;12(4):641–51.
5. Ebbesen EN, Thomsen JS, Beck-Nielsen H, Nepper-Rasmussen HJ, Mosekilde L. Lumbar vertebral body compressive strength evaluated by dual-energy X-ray absorptiometry, quantitative computed tomography, and ashing. *Bone.* 1999 Dec;25(6):713–24.
6. Cann CE, Genant HK. Precise measurement of vertebral mineral content using computed tomography. *J Comput Assist Tomogr.* 1980;4(4):493–500.
7. Merritt RB, Chenery SG. Quantitative CT measurements: the effect of scatter acceptance and filter characteristics on the EMI 7070. *Phys Med Biol.* 1986 Jan 1;31(1):55.
8. Glüer C-C, Genant HK. Impact of marrow fat on accuracy of quantitative CT. *J Comput Assist Tomogr.* 1989 Nov;13(6):1023–35.
9. Alvarez RE, Macovski A. Energy-selective reconstructions in X-ray computerised tomography. *Phys Med Biol.* 1976 Sep 1;21(5):733–44.
10. Bouillon R, Burckhardt P, Christiansen C, Fleisch HA, Fujita T, Gennari, C, et al. Consensus development conference: prophylaxis and treatment of osteoporosis. *Am J Med.* 1991 Jan;90(1):107–10.
11. Patni R. Normal BMD values for Indian females aged 20-80 years. *J Midlife Health.* 2010;1(2):70.
12. Nordin BEC. Clinical Significance and Pathogenesis of Osteoporosis. *Br Med J.* 1971 Mar 13;1(5749):571–6.
13. Laval-Jeantet AM, Roger B, Cann CE. Age related changes of vertebral marrow fat and influence on CT densitometry. *J Comput Assist Tomogr.* 1983;7(3):562.
14. Meunier P, Courpron P, Edouard C, Bernard J, Bringuier J, Vignon G. Physiological senile involution and pathological rarefaction of bone: Quantitative and comparative histological data. *Clin Endocrinol Metab.* 1973 Jul;2(2):239–56.

15. Riggs BL, Wahner HW, Dunn WL, Mazess RB, Offord KP, Melton L. Differential changes in bone mineral density of the appendicular and axial skeleton with aging: relationship to spinal osteoporosis. *J Clin Invest.* 1980 Sep;67(2):328.
16. Recker RR, Saville PD, Heaney RP. Effect of estrogens and calcium carbonate on bone loss in postmenopausal women. *Ann Intern Med.* 1977 Dec 1;87(6):649–55.
17. Riggs BL, Khosla S, Melton LJ. A unitary model for involitional osteoporosis: estrogen deficiency causes both type I and type II osteoporosis in postmenopausal women and contributes to bone loss in aging men. *J Bone Miner Res.* 1998;13(5):763–73.
18. Bullamore JR, Wilkinson R, Gallagher JC, Nordin BEC, Marshall DH. Effect of age on calcium absorption. *Lancet.* 1970 Sep 12;296(7672):535–7.
19. Griffiths HJ, Zimmerman RE. The clinical application of bone mineral analysis. *Skeletal Radiol.* 1978 Jul 1;3(1):1–9.
20. Taxel P, Kenny A. Differential diagnosis and secondary causes of osteoporosis. *Clin Cornerstone.* 2000;2(6):11–9.
21. Vehmanen L, Saarto T, Elomaa I, Mäkelä P, Välimäki M, Blomqvist C. Long-term impact of chemotherapy-induced ovarian failure on bone mineral density (BMD) in premenopausal breast cancer patients. The effect of adjuvant clodronate treatment. *Eur J Cancer.* 2001 Dec;37(18):2373–8.
22. Hirbe A. Skeletal complications of breast and prostate cancer therapies. In: Favus MJ, editor. *Primer on the Metabolic Bone Diseases and Disorders of Mineral Metabolism.* Washington, D.C.: American Society for Bone and Mineral Research; 2006.
23. Kelly J, Damron T, Grant W, Anker C, Holdridge S, Shaw S, et al. Cross-sectional study of bone mineral density in adult survivors of solid pediatric cancers. *J Pediatr Hematol Oncol.* 2005 May;27(5):248–53.
24. Lambiase R, Sartoris DJ, Fellingham L, Andre M, Resnick D. Vertebral mineral status: assessment with single- versus multi-section CT. *Radiology.* 1987 Jul;164(1):231–6.
25. Engelke K, Adams JE, Armbrecht G, Augat P, Bogado CE, Bouxsein ML, et al. Clinical use of quantitative computed tomography and peripheral quantitative computed tomography in the management of osteoporosis in adults: the 2007 ISCD official positions. *J Clin Densitom.* 2008 Jan;11(1):123–62.
26. Cann CE, Genant HK, Ettinger B, Gordan GS. Spinal mineral loss in oophorectomized women: Determination by quantitative computed tomography. *JAMA.* 1980 Nov 7;244(18):2056–9.
27. Genant HK, Cann CE, Ettinger B, Gordan GS. Quantitative Computed Tomography of Vertebral Spongiosa: A Sensitive Method for Detecting Early Bone Loss After Oophorectomy. *Ann Intern Med.* 1982 Nov 1;97(5):699–705.
28. Frost HM. Tetracycline-based histological analysis of bone remodeling. *Calc Tis Res.* 1969 Dec 1;3(1):211–37.

29. ICRP Publication 23. Report of the task group on reference man. Oxford: Pergamon Press; 1975.
30. Parfitt AM, Mathews CH, Villanueva AR, Kleerekoper M, Frame B, Rao DS. Relationships between surface, volume, and thickness of iliac trabecular bone in aging and in osteoporosis. Implications for the microanatomic and cellular mechanisms of bone loss. *J Clin Invest.* 1983 Oct;72(4):1396–409.
31. Mazess RB, Vetter J. The influence of marrow on measurement of trabecular bone using computed tomography. *Bone.* 1985;6(5):349–51.
32. Cann CE, Ettinger B, Genant HK. Normal subjects versus osteoporotics: No evidence using dual energy computed tomography for disproportionate increase in vertebral marrow fat. *J Comput Assist Tomogr.* 1985;9(3):617.
33. Laval-Jeantet AM, Roger B, Bouysee S, Bergot C, Mazess RB. Influence of vertebral fat content on quantitative CT density. *Radiology.* 1986;159(2):463–6.
34. Reinbold WD, Genant HK, Reiser UJ, Harris ST, Ettinger B. Bone mineral content in early-postmenopausal and postmenopausal osteoporotic women: comparison of measurement methods. *Radiology.* 1986 Aug 1;160(2):469–78.
35. Pacifici R, Susman N, Carr PL, Birge SJ, Avioli LV. Single and dual energy tomographic analysis of spinal trabecular bone: A comparative study in normal and osteoporotic women. *J Clin Endocrinol Metab.* 1987 Feb 1;64(2):209–14.
36. Mosekilde L, Bentzen SM, Ørtoft G, Jørgensen J. The predictive value of quantitative computed tomography for vertebral body compressive strength and ash density. *Bone.* 1989;10(6):465–70.
37. Richardson ML, Genant HK, Cann CE, Ettinger B, Gordan GS, Kolb FO, et al. Assessment of metabolic bone diseases by quantitative computed tomography. *Clin Orthop Relat Res.* 1985 May;(195):224–38.
38. Ensrud K, Thompson D, Cauley J, Nevitt M, Kado D, Hochberg M, et al. Prevalent vertebral deformities predict mortality and hospitalization in older women with low bone mass. Fracture Intervention Trial Research Group. *J Am Geriatr Soc.* 2000 Mar;48(3):241–9.
39. Eastell R, Mosekilde L, Hodgson SF, Riggs BL. Proportion of human vertebral body bone that is cancellous. *J Bone Miner Res.* 1990;5(12):1237–41.
40. Genant HK, Engelke K, Fuerst T, Glüer C-C, Grampp S, Harris ST, et al. Noninvasive assessment of bone mineral and structure: State of the art. *J Bone Miner Res.* 1996;11(6):707–30.
41. Jacobson B. X-ray spectrophotometry in vivo. *Am J Roentgenol, Radium Therapy Nucl Med* [Internet]. 1964 Jan 1 [cited 2014 Jan 4];91. Available from: <http://www.osti.gov/scitech/biblio/4143053>
42. Stein JA, Lazewatsky JL, Hochberg AM. Dual energy X-ray bone densitometer incorporating an internal reference system. *Radiology.* 1987;165(2):313.
43. Elsasser U, Rügsegger P. Proceedings: Bone densitometry with the aid of computerized transaxial tomography. *Am J Roentgenol.* 1976 Jun;126(6):1275–7.

44. Isherwood I, Rutherford RA, Pullan BR, Adams PH. BONE-MINERAL ESTIMATION BY COMPUTER-ASSISTED TRANSVERSE AXIAL TOMOGRAPHY. *The Lancet*. 1976 Oct 2;308(7988):712–5.
45. Genant HK, Boyd D, Korobkin M, Norman D. Quantitative bone mineral analysis using dual energy computerized tomographic scanning. *Invest Radiol*. 1976;11(5):385.
46. Intenzo CM, Parker L, Rao VM, Levin DC. Changes in procedure volume and service provider distribution among radiologists and nonradiologists in dual-energy x-Ray absorptiometry between 1996 and 2002. *J Am Coll Radiol*. 2005 Aug;2(8):662–4.
47. Guglielmi G, Glüer CC, Majumdar S, Blunt BA, Genant HK. Current methods and advances in bone densitometry. *Eur Radiol*. 1995 Mar 1;5(2):129–39.
48. Tofts PS, Sank VJ. Definitions of effective energy in computed tomography. *J Comput Assist Tomogr*. 1981;5(6):950.
49. Sorenson JA, Duke PR, Smith SW. Simulation studies of dual-energy x-ray absorptiometry. *Med Phys*. 1989 Jan 1;16(1):75–80.
50. Peppler WW, Mazess RB. Total body bone mineral and lean body mass by dual-photon absorptiometry. *Calcif Tissue Int*. 1981 Dec 1;33(1):353–9.
51. Hangartner TN, Johnston CC. Influence of fat on bone measurements with dual-energy absorptiometry. *Bone and Mineral*. 1990 Apr;9(1):71–81.
52. Genant HK, Grampp S, Glüer CC, Faulkner KG, Jergas M, Engelke K, et al. Universal standardization for dual X-ray absorptiometry: Patient and phantom cross-calibration results. *J Bone Miner Res*. 1994;9(10):1503–14.
53. Mazess RB, Barden H. Bone Density of the Spine and Femur in Adult White Females. *Calcif Tissue Int*. 1999 Aug 1;65(2):91–9.
54. Maalouf G, Salem S, Sandid M, Attallah P, Eid J, Saliba N, et al. Bone Mineral Density of the Lebanese Reference Population. *Osteoporos Int*. 2000 Sep 1;11(9):756–64.
55. Wu XP, Liao EY, Huang G, Dai RC, Zhang H. A Comparison Study of the Reference Curves of Bone Mineral Density at Different Skeletal Sites in Native Chinese, Japanese, and American Caucasian Women. *Calcif Tissue Int*. 2003 Aug 1;73(2):122–32.
56. Ho-Pham LT, Nguyen UDT, Pham HN, Nguyen ND, Nguyen TV. Reference ranges for bone mineral density and prevalence of osteoporosis in vietnamese men and women. *BMC Musculoskelet Disord*. 2011 Aug 10;12(1):182.
57. Hall ML, Heavens J, Cullum ID, Ell PJ. The range of bone density in normal British women. *Br J Radiol*. 1990 Apr 1;63(748):266–9.
58. Pacifici R, Rupich R, Griffin M, Chines A, Susman N, Avioli LV. Dual energy radiography versus quantitative computer tomography for the diagnosis of osteoporosis. *J Clin Endocrinol Metab*. 1990 Mar 1;70(3):705–10.

59. Brooks RA, Di Chiro G. Theory of Image Reconstruction in Computed Tomography. *Radiology*. 1975 Dec 1;117(3):561–72.
60. Bushberg JT, Seibert JA, Ledholdt Jr. EM, Boone JM. *Computed Tomography. The Essential Physics of Medical Imaging*. 3rd ed. Philadelphia, PA, USA: Lippincott Williams & Wilkins; 2012. p. 352–4.
61. Pickhardt PJ, Pooler BD, Lauder T, del Rio AM, Bruce RJ, Binkley N. Opportunistic Screening for Osteoporosis Using Abdominal Computed Tomography Scans Obtained for Other Indications. *Ann Intern Med*. 2013 Apr 16;158(8):588–95.
62. Lee S, Chung CK, Oh SH, Park SB. Correlation between Bone Mineral Density Measured by Dual-Energy X-Ray Absorptiometry and Hounsfield Units Measured by Diagnostic CT in Lumbar Spine. *J Korean Neurosurg Soc*. 2013 Nov;54(5):384–9.
63. Witt RM, Cameron JR. Improved bone standard containing dipotassium hydrogen phosphate solution for the intercomparison of different transmission bone scanning systems. Wisconsin Univ., Madison. Dept. of Radiology; 1970.
64. Cody DD, Flynn MJ, Vickers DS. A technique for measuring regional bone mineral density in human lumbar vertebral bodies. *Medical Physics*. 1989;16(5):766–72.
65. Faulkner KG, Glüer CC, Grampp S, Genant HK. Cross-calibration of liquid and solid QCT calibration standards: Corrections to the UCSF normative data. *Osteoporosis Int*. 1993 Jan 1;3(1):36–42.
66. Nazarian A, Snyder BD, Zurakowski D, Müller R. Quantitative micro-computed tomography: A non-invasive method to assess equivalent bone mineral density. *Bone*. 2008 Aug;43(2):302–11.
67. Kalender WA, Suess C. A new calibration phantom for quantitative computed tomography. *Med Phys*. 1987 Sep 1;14(5):863–6.
68. Genant HK, Boyd D. Quantitative bone mineral analysis using dual energy computed tomography. *Invest Radiol*. 1977;12(6):545–51.
69. Adams JE, Chen SZ, Adams PH, Isherwood I. Measurement of trabecular bone mineral by dual energy computed tomography. *J Comput Assist Tomogr*. 1982;6(3):601–7.
70. Hounsfield GN. Computerized transverse axial scanning (tomography): Part 1. Description of system. *Br J Radiol*. 1973 Dec 1;46(552):1016–22.
71. Genant HK, Cann CE, Ettigner B, Gordan GS, Felix O, Reiser U, et al. Quantitative computed tomography for spinal mineral assessment: current status. *J Comput Assist Tomogr*. 1985;9(3):602–3.
72. Bligh M, Bidaut L, White RA, Murphy Jr. WA, Stevens DM, Cody DD. Helical multidetector row quantitative computed tomography (QCT) precision. *Acad Radiol*. 2009 Feb;16(2):150–9.
73. Genant HK, Steiger P, Block JE, Glueer CC, Ettinger B, Harris ST. Quantitative computed tomography: Update 1987. *Calcif Tissue Int*. 1987 Oct 1;41(4):179–86.



74. Guglielmi G, Grimston SK, Fischer KC, Pacifici R. Osteoporosis: diagnosis with lateral and posteroanterior dual x-ray absorptiometry compared with quantitative CT. *Radiology*. 1994 Sep 1;192(3):845–50.
75. Damilakis J, Adams JE, Guglielmi G, Link TM. Radiation exposure in X-ray-based imaging techniques used in osteoporosis. *Eur Radiol*. 2010 Nov 1;20(11):2707–14.
76. Kalender WA, Klotz E, Suess C. Vertebral bone mineral analysis: an integrated approach with CT. *Radiology*. 1987;164(2):419–23.
77. Brooks RA, Chiro GD. Beam hardening in X-ray reconstructive tomography. *Phys Med Biol*. 1976 May 1;21(3):390.
78. Weissberger MA, Zamenhof RG, Aronow S, Neer RM. Computed tomography scanning for the measurement of bone mineral in the human spine. *J Comput Assist Tomogr*. 1978;2(3):253–62.
79. Blake GM, McKeeney DB, Chhaya SC, Ryan PJ, Fogelman I. Dual energy x-ray absorptiometry: The effects of beam hardening on bone density measurements. *Med Phys*. 1992 Mar 1;19(2):459–65.
80. Imamura K, Fujii M. Empirical beam hardening correction in the measurement of vertebral bone mineral content by computed tomography. *Radiology*. 1981 Jan 1;138(1):223–6.
81. Nalcioğlu O, Lou RY. Post-reconstruction method for beam hardening in computerised tomography. *Phys Med Biol*. 1979 Mar 1;24(2):330.
82. Glover GH. Compton scatter effects in CT reconstructions. *Med Phys*. 1982 Nov 1;9(6):860–7.
83. Overton TR, Macey DJ, Hangartner TN, Battista JJ. Accuracy and precision in X-ray CT and [gamma]-ray CT measurement of bone density. Identification and evaluation of some sources of error in quantitative studies. *J Comput Assist Tomogr*. 1985;9(3):606.
84. Dougherty G. Quantitative CT in the measurement of bone quantity and bone quality for assessing osteoporosis. *Med Eng Phys*. 1996 Oct;18(7):557–68.
85. Mazess RB. Errors in measuring trabecular bone by computed tomography due to marrow and bone composition. *Calcif Tissue Int*. 1983 Dec 1;35(1):148–52.
86. Glüer C-C, Reiser UJ, Davis CA, Rutt BK, Genant HK. Vertebral mineral determination by quantitative computed tomography (QCT): Accuracy of single and dual energy measurements. *J Comput Assist Tomogr*. 1988 Apr;12(2):242–58.
87. Laval-Jeantet AM, Cann CE, Roger BM, Dallant P. A postprocessing dual energy technique for vertebral CT densitometry. *J Comput Assist Tomogr*. 1984;8(6):1164–7.
88. Maaß C, Baer M, Kachelrieß M. Image-based dual energy CT using optimized precorrection functions: A practical new approach of material decomposition in image domain. *Med Phys*. 2009 Jul 24;36(8):3818–29.
89. Bolus DN. Dual-energy computed tomographic scanners: principles, comparisons, and contrasts. *J Comput Assist Tomogr*. 2013;37(6):944–7.



90. Cann CE, Gamsu G, Birnberg FA, Webb WR. Quantification of calcium in solitary pulmonary nodules using single- and dual-energy CT. *Radiology*. 1982 Nov 1;145(2):493–6.
91. Cann CE, Genant HK. Single versus dual energy CT for vertebral mineral quantification. *J Comput Assist Tomogr*. 1983 Jun;7(3):551.
92. Rutherford RA, Pullan BR, Isherwood I. X-ray energies for effective atomic number determination. *Neuroradiology*. 1976 May 1;11(1):23–8.
93. Millner MR, McDavid WD, Waggener RG, Dennis MJ, Payne WH, Sank VJ. Extraction of information from CT scans at different energies. *Med Phys*. 1979 Jan 1;6(1):70–1.
94. Faul DD, Couch JL, Cann CE, Boyd DP, Genant HK. Composition-selective reconstruction for mineral content in the axial and appendicular skeleton. *J Comput Assist Tomogr*. 1982;6(1):202–3.
95. Rutt B, Fenster A. Split-filter computed tomography: A simple technique for dual energy scanning. *J Comput Assist Tomogr*. 1980;4(4):501–9.
96. Brooks RA, Chiro GD. Split-detector computed tomography: A preliminary report. *Radiology*. 1978 Jan 1;126(1):255–7.
97. Flohr TG, McCollough CH, Bruder H, Petersilka M, Gruber K, Süß C, et al. First performance evaluation of a dual-source CT (DSCT) system. *Eur Radiol*. 2006 Feb 1;16(2):256–68.
98. Graser A, Johnson TRC, Chandarana H, Macari M. Dual energy CT: preliminary observations and potential clinical applications in the abdomen. *Eur Radiol*. 2009 Jan 1;19(1):13–23.
99. Kalender WA, Perman WH, Vetter JR, Klotz E. Evaluation of a prototype dual-energy computed tomographic apparatus. I. Phantom studies. *Med Phys*. 1986 May 1;13(3):334–9.
100. Zou Y, Silver MD. Analysis of fast kV-switching in dual energy CT using a pre-reconstruction decomposition technique. 2008 [cited 2014 Jan 3]. p. 691313. Available from: <http://dx.doi.org/10.1117/12.772826>
101. Goodsitt MM, Rosenthal DI. Quantitative computed tomography scanning for measurement of bone and bone marrow fat content: a comparison of single- and dual-energy techniques using a solid synthetic phantom. *Invest Radiol*. 1987;22(10):799–810.
102. Cann CE. Quantitative CT for determination of bone mineral density: a review. *Radiology*. 1988 Feb 1;166(2):509–22.
103. Yeh BM, Shepherd JA, Wang ZJ, Seong Teh H, Hartman RP, Prevrhal S. Dual-energy and low-kVp CT in the abdomen. *Am J Roentgenol*. 2009 Jul;193(1):47–54.
104. Kraśnicki T, Podgórski P, Guziński M, Czarnecka A, Tupikowski K, Garcarek J, et al. Novel clinical applications of dual energy computed tomography. *Adv Clin Exp Med*. 2011 Dec;21(6):831–41.
105. Morgan DE. Dual-energy CT of the abdomen. *Abdom Imaging*. 2013 Sep 26;1–27.

106. Ito M, Hayashi K, Yamada N. [Evaluation of bone mineral density with dual energy quantitative computed tomography (DEQCT)]. *Nihon Igaku Hoshasen Gakkai Zasshi*. 1989 Aug 25;49(8):999–1008.
107. Rao GU, Yaghami I, Wist AO, Arora G. Systematic errors in bone-mineral measurements by quantitative computed tomography. *Med Phys*. 1986 Oct 17;14(1):62–9.
108. Benson GC, Kiyohara O. Thermodynamics of aqueous mixtures of nonelectrolytes. I. Excess volumes of water-n-alcohol mixtures at several temperatures. *J Solution Chem*. 1980 Oct 1;9(10):791–804.
109. Berger MJ, Hubbell JH, Seltzer SM, Chang J, Coursey JS, Sukumar R, et al. XCOM: Photon Cross Section Database [Online] [Internet]. Gaithersburg, MD: National Institute of Standards and Technology; 2010. Available from: <http://physics.nist.gov/xcom>
110. Bland MJ, Altman DG. Statistical methods for assessing agreement between two methods of clinical measurement. *Lancet*. 1986 Feb 8;327(8476):307–10.
111. Cann CE, Genant HK, Kolb FO, Ettinger B. Quantitative computed tomography for prediction of vertebral fracture risk. *Bone*. 1985;6(1):1–7.
112. Genant HK, Block JE, Steiger P, Glueer C-C, Smith R. Quantitative computed tomography in assessment of osteoporosis. *Semin Nucl Med*. 1987 Oct;17(4):316–33.
113. Lehmann LA, Alvarez RE, Macovski A, Brody WR, Pelc NJ, Riederer SJ, et al. Generalized image combinations in dual KVP digital radiography. *Medical Physics*. 1981 Sep 1;8(5):659–67.
114. Kalender WA. A phantom for standardization and quality control in spinal bone mineral measurements by QCT and DXA: Design considerations and specifications. *Med Phys*. 1992 May 1;19(3):583–6.
115. Rasband WS. ImageJ [Internet]. Bethesda, MD: U.S. National Institutes of Health; 2013. Available from: <http://imagej.nih.gov/ij/>
116. Kappadath SC, Shaw CC. Dual-energy digital mammography: Calibration and inverse-mapping techniques to estimate calcification thickness and glandular-tissue ratio. *Medical Physics*. 2003;30(6):1110–7.

## **Vita**

John Matthew Spiridigliozzi Wait was born in Chapel Hill, North Carolina on August 24, 1988, the son of Gail Anne Spiridigliozzi and John Selby Wait. After completing his work at Riverside High School in Durham, North Carolina in 2006, he attended the University of Florida and then transferred to The University of North Carolina in Chapel Hill, North Carolina. He received a Bachelor of Science degree in Physics in December, 2010. In August of 2011 he entered The University of Texas Health Science Center at Houston Graduate School of Biomedical Sciences.

Permanent address:

4909 Stockton Way  
Durham, NC 27707